Summer 2022

Hydroclimate variability in Central America during the Holocene inferred from lacustrine sediments in Lake Izabal, eastern Guatemala

Edward Fernando Duarte

Department: Geosciences and Geological and Petroleum Engineering

HYDROCLIMATE VARIABILITY IN CENTRAL AMERICA DURING THE HOLOCENE INFERRED FROM LACUSTRINE SEDIMENTS IN LAKE IZABAL, EASTERN GUATEMALA

by

EDWARD FERNANDO DUARTE MARTINEZ

A DISSERTATION

Presented to the Graduate Faculty of the

MISSOURI UNIVERSITY OF SCIENCE AND TECHNOLOGY

In Partial Fulfillment of the Requirements for the Degree

DOCTOR OF PHILOSOPHY

in

GEOLOGY AND GEOPHYSICS

2022

Approved by:

Jonathan Obrist-Farner, Advisor
Francisca Oboh-Ikuenobe
Wan Yang
John Hogan
Andreas Eckert

PUBLICATION DISSERTATION OPTION

This dissertation consists of the following two articles, formatted in the style used by the Missouri University of Science and Technology:

Paper I, found on pages 4–103, has been published in *Earth and Planetary Science Letters*.

Paper II, found on pages 104–141, has been submitted to *Journal of Paleolimnology*.

ABSTRACT

Holocene hydroclimate reconstructions have contributed to our understanding of the mechanisms controlling precipitation in Central America. Recent hydroclimate proxy records from the region, however, have revealed considerable spatiotemporal complexity in precipitation variability. This complexity is hypothesized to result from the interaction between multiple oceanic-atmospheric processes that converge in the region. This project analyzed three sediment cores from Lake Izabal, eastern lowland Guatemala, with the goal of understanding changes in precipitation, lake productivity, and lake water chemistry during the Holocene. Our proxy results indicate that precipitation in the region increased from the early to the middle Holocene, when Lake Izabal became a meromictic lake following a marine incursion. Anoxic bottom waters lasted ~3,500 years, preserving 2,186 mm-scale dark and light laminae couplets that are distinctly different in color, composition, and texture. At ~4,800 calibrated years before present (cal yr BP), Lake Izabal became a polymictic lake, and precipitation in the region stabilized, remaining high until ~1,200 cal yr BP, with an abrupt decrease in precipitation thereafter. Our findings indicate that Lake Izabal is highly sensitive to changes in Caribbean sea level and Caribbean sea-surface temperatures, the former controlling lake water chemistry and the latter controlling precipitation. Our results also add to new hydroclimate proxy data from the region, highlighting the complexity in precipitation variability in the area. Additional paleoclimate proxy records from Central America are needed to improve our understanding of how global warming will affect environmental conditions and regional hydroclimate variability.

ACKNOWLEDGMENTS

First, I would like to express great appreciation to Dr. Jonathan Obrist-Farner for believing in me and giving me the opportunity and honor to work under his guidance on this wonderful research project. His hard work, commitment, and technical excellence inspired me to achieve my goals and materialize this project.

This research was partially supported by NSF/GSA (National Science Foundation/Geological Society of America) Graduate Student Research Grants No. 12101-18 and No. 12638-19, funded by NSF Award No. 1949901. This research was also partially supported by the American Association of Petroleum Geologists (AAPG) Grants-in-Aid, and the Visiting Graduate Student Travel Grant Program from the National Lacustrine Core (LacCore) Facility and the Continental Scientific Drilling Coordination Office. Additionally, I wish to thank the Geosciences and Geological and Petroleum Engineering Department at Missouri S&T for supporting me as a graduate teaching assistant.

I wish to thank my committee members, Dr. Oboh-Ikuenobe, Dr. Yang, Dr. Hogan, and Dr. Eckert, for their valuable comments and suggestions regarding my research. I also thank colleagues for the enlightening discussions and fruitful feedback.

Lastly, I am so grateful to my mother, sister, and aunt for their constant enthusiasm, motivation, and emotional support. Their patience and understanding have continually strengthened me and helped me achieve my personal and professional goals.

TABLE OF CONTENTS

Page

LIST OF ILLUSTRATIONS

PAPER I Page

PAPER II

NOMENCLATURE

Symbol	Description
cal yr BP	Calibrated years before present
XRF	X-ray fluorescence
µXRF	Micro X-ray fluorescence
cps	counts per second
AMS	Accelerator mass spectromery
MS	Magnetic susceptibility
PCA	Principal composent analysis
zPCA	Zonal principal composent analysis
SST	Sea-surface temeperature
ITCZ	Intertropical Convergence Zone
CLLJ	Caribbean Low Level Jet
ENSO	El Niño Southern Oscillation
NASH	North Atlantic Subtropical High
AWP	Atlantic Warm Pool
MWI	Mud-water interface
wt% C	weight percent of Carbon
Mz	Mean grain size
Ca.	Circa

1. INTRODUCTION

Analysis of 40 years of instrumental data in Central America has revealed a significant reduction in precipitation (Anderson et al., 2019). This drying trend is expected to worsen under continued global warming, with the Intergovernmental Panel on Climate Change (IPCC) projecting a reduction of up to 50% in precipitation by the end of the 21st century (Gutiérrez et al., 2021). However, significant inter-model heterogeneity (Christensen et al., 2007; Bhattacharya & Coats, 2020; Gutiérrez et al., 2021) highlights the uncertainty in hydroclimate projections. These uncertainties are made worse by insufficient regional instrumental data, both spatially and temporally, and by the complex interaction of several oceanic-atmospheric processes acting on much shorter time scales that significantly influence Holocene hydroclimate in the region (Wang, 2007; Martinez et al., 2019). Additional highly resolved proxy records for Central America can provide insights into the dominant mechanisms driving precipitation change and contribute to better assess potential deviations in regional precipitation.

For Central America and the Caribbean, sediment and speleothem records have been widely used to investigate Holocene hydroclimate response to external forcing. Holocene hydroclimate records suggest similar changes during the Holocene, supporting teleconnective linkages for the region (Haug et al., 2001; Mueller et al., 2009; Fensterer et al., 2013). For example, lacustrine records from the northern Yucatán Peninsula indicate that wet conditions prevailed for most of the early and middle Holocene, changing to dry conditions during the late Holocene (Mueller et al., 2009; Hillesheim et al., 2005). Similar interpretations from Lake Miragoane in Haiti (Hodell et al., 1991) and

marine sediments from the Cariaco Basin, offshore Venezuela (Haug et al., 2001) have led to the inference that the entire Central American and Caribbean region underwent similar climatic changes and transitions. A prevailing hypothesis to explain the similarities is that precipitation throughout the Holocene was driven by changes in seasonal insolation and the resulting effects on Intertropical Convergence Zone (ITCZ) dynamics (Hodell et al., 1991; Haug et al., 2001). New Holocene terrestrial records from the Guatemala highlands, however, reveal differing precipitation trends, suggesting that oceanic and atmospheric processes acting on much shorter time scales significantly influenced the Holocene hydroclimate in the region (Stansell et al., 2020; Winter et al., 2020). The lack of consistency between paleoclimate records in Central America highlights the need for additional paleoclimate proxy records that may contribute to understand the relationships between oceanic-atmospheric processes and hydroclimate variability.

This project analyzed three sediment cores from Lake Izabal that provides insight into hydroclimate changes during the Holocene. Lake Izabal, located in the eastern lowlands of Guatemala, is a shallow (z = 15 m) polymictic lake with a surface area of 672 km^2 and a hydrological catchment area of 8,740 km^2. Modern limnological observations indicate that the lake is highly sensitive to precipitation seasonality, which significantly affects lake level variations, lake productivity, and sediment and organic matter input into the lake (Brinson, 1973; Brinson and Nordlie, 1975). This project utilized radiocarbon-based age-depth models integrated with lithological, X-ray fluorescence scanning, and multivariate statistical analysis to infer changes in precipitation, lake productivity, and lake water chemistry during the Holocene.

Our proxy results indicate that precipitation in the region increased from the early to the middle Holocene, when Lake Izabal became a meromictic lake following a marine incursion. Although Lake Izabal is currently shallow and well-mixed, this marine incursion established a chemocline in the lake, with persistent bottom-water anoxia that lasted approximately 3,500 years between 8,370 and 4,800 cal yr BP (Obrist-Farner et al., 2022). Anoxia decreased bioturbation in the deeper parts of the basin, facilitating the preservation of a 400-cm-thick thinly laminated silty clay section that contains 2,186 dark/light laminae couplets. The dark and light laminae are sedimentological and geochemical distinct, and similarities between radiocarbon age-depth models and total laminae counts suggest that the couplets are annual deposits. At ~4,800 cal yr BP, Lake Izabal became a polymictic lake, and precipitation in the region remained high until ~1,200 cal yr BP, with an abrupt decrease in precipitation thereafter. Our findings indicate that Lake Izabal is highly sensitive to changes in Caribbean Sea level and Caribbean Sea-surface temperatures (SST). Marine waters allowed the preservation of an annually resolved laminated record that could offer the potential for high-resolution quantitative paleoclimatic reconstructions in the region, while the SST controlled precipitation along the eastern coast of Central America. Comparison of the Izabal record with other paleoclimate records from Central America and the Caribbean highlights the complexity in precipitation variability in the region.

PAPER

I. A PROGRESSIVELY WETTER EARLY THROUGH MIDDLE HOLOCENE CLIMATE IN THE EASTERN LOWLANDS OF GUATEMALA

Edward Duarte[1], Jonathan Obrist-Farner[1], Alex Correa-Metrio[2, 3], Byron A. Steinman[4]

[1]Geosciences and Geological and Petroleum Engineering Department, Missouri University of Science and Technology, Rolla, MO 65409, USA

[2]Instituto de Geología, Universidad Nacional Autónoma de México, Coyoacán, CDMX 04510, México

[3]Centro de Geociencias, Universidad Nacional Autónoma de México, Juriquilla, QRO 76230, México

[4]Large Lakes Observatory and Department of Earth and Environmental Sciences, University of Minnesota Duluth, Duluth, MN 55812, USA

ABSTRACT

Climate records from Central America and the Caribbean region reveal considerable spatiotemporal complexity in precipitation variability, with multiple hypotheses explaining the likely ocean-atmosphere processes influencing precipitation in the region. Here we report on findings from a 760-cm long sediment core from Lake Izabal, eastern Guatemala that affords insight on regional hydroclimate change over the last ~9,500 years. We utilized a radiocarbon-based age-depth model integrated with lithological, XRF elemental abundances, and principal component analyses to infer changes in erosion/precipitation, lake productivity, and lake water chemistry. Abundance of elements commonly associated with terrigenous sources increase from the early to the

latest mid-Holocene, from ca. 9,500 to ca. 4,800 calibrated years before present (cal yr BP), suggesting a progressive increase in precipitation/erosion. This is followed by relatively stable and high erosion/precipitation conditions until ca. 1,200 cal yr BP, with an abrupt decrease in precipitation/erosion ~1,200 years ago. Comparison of the Izabal record with other paleoclimate records from Central America and the Caribbean region indicates substantial heterogeneity in hydroclimate, even across relatively short distances, likely due to a combination of topographic complexity and the combined influences of Atlantic and Pacific basin ocean-atmosphere dynamics. Our results suggest that the progressive increase in boreal autumn insolation throughout the middle and late Holocene may have driven an increase in Caribbean sea-surface temperatures (SST) during the late wet season, leading to increased moisture availability through enhanced evaporation and greater precipitation amounts associated with zonal convergence and orographic uplift along the eastern coast of Central America. However, other nearby records demonstrate hydroclimate changes that are at least partially at odds with the Izabal record, indicating that the modern SST relationships with atmospheric circulation, including Intertropical Convergence Zone dynamics, and precipitation alone cannot be used as a framework for explaining hydroclimate variability across Central America during the Holocene.

1. INTRODUCTION

Sediment and speleothem records have been widely used to reconstruct Holocene paleoenvironmental and paleoclimatic conditions in a diversity of environments around the world. For tropical regions, especially Central America and the Caribbean (Figures 1,

2), such records have been used to investigate Holocene hydroclimate responses to external forcing, such as changes in seasonal insolation and the resulting effects on Intertropical Convergence Zone (ITCZ) dynamics (Hodell et al., 1991; Haug et al., 2001). Analysis of Holocene hydroclimate records suggests similarities between some proxy records of hydroclimate change, as well as inter-hemispheric asynchronicity (Mueller et al., 2009). Based on these inferences, a prevailing hypothesis has emerged that broad-scale variability in tropical precipitation throughout the Holocene was driven by changes in the mean position of the ITCZ (Haug et al., 2001; Mueller et al., 2009). New Holocene proxy records from Central America, however, indicate that past hydroclimatic change across the Isthmus was not spatially and temporally synchronous on century to millennial timescales (Winter et al., 2020) and, at least during the late Holocene, that changes in the strength/width of the ITCZ, rather than its mean position, were the main drivers of hydroclimate change (Asmeron et al., 2020).

Central American hydroclimate and, in particular, precipitation patterns are complex, with the Caribbean coast of Nicaragua, Honduras, and Guatemala, as well as the highland region of Guatemala, receiving three times more precipitation than other regions in Central America (Figure 1). Precipitation on the western Caribbean coast of Central America also differs from the typical May to October rainy season experienced in most parts of the southern coast of the Isthmus (Martinez et al., 2019; Figure 3). On the southern coast, precipitation is mainly driven by the northerly migration of the ITCZ (Martinez et al., 2019), whereas substantial precipitation occurs on the Caribbean coast of Guatemala in October and November after the migration of the ITCZ to the south (Figure 3). The complexity of modern precipitation patterns and the inconsistencies in past

hydroclimate shifts inferred from proxy records impede our understanding of the effect of external forcing on Central American climate. Consequently, predictions of future hydroclimate change in response to both human and natural external controls are beset by substantial uncertainty, a significant problem for a region that heavily depends on summer rains for agricultural purposes and that has experienced devastating droughts in the recent past (Hodell et al., 1995; Hodell et al., 2001; Mueller et al., 2009; Correa-Metrio et al., 2012; Wahl et al., 2014).

Sedimentological studies of Guatemalan lakes have utilized a diverse set of proxies, such as pollen (Leyden, 2002; Wahl et al., 2006; Correa-Metrio et al., 2012), magnetic susceptibility and density (Hodell et al., 2001), elemental concentrations (Mueller et al., 2009), and stable isotopes (Hodell et al., 1995; Stansell et al., 2020), to reconstruct hydroclimatic conditions through the Holocene. Despite the increasing number of paleoclimate records from Guatemala, complete Holocene records are rare, and most come from the northern lowlands, resulting in a spatiotemporal bias that hinders a complete understanding of hydroclimate change in the region. Lake sediments from the northern lowlands also record late Holocene landscape modification due to anthropogenic activities (e.g., Leyden, 2002; Mueller et al., 2009), confounding paleoclimate signals. The development of proxy records from relatively understudied eastern Guatemala, which is both the wettest area in the country (Figure 1) and has less evidence for human occupation throughout the Holocene, can provide additional information to further understand regional hydroclimate drivers.

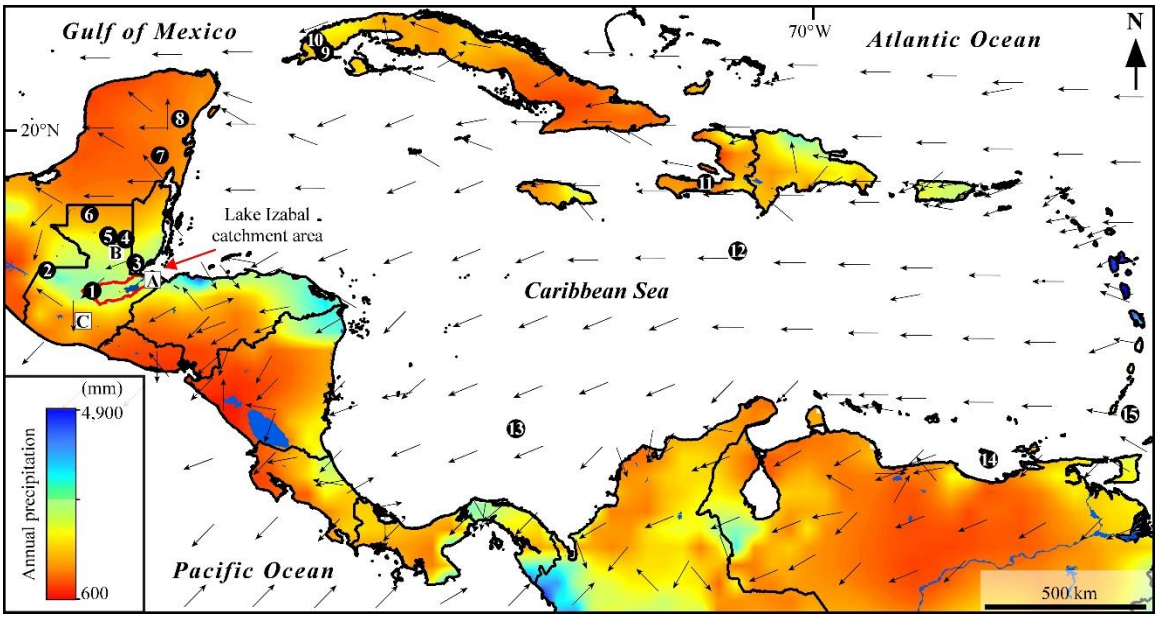

Figure 1. Map of Central America and the Caribbean showing the average distribution of rainfall for the period between 1960 to 2018 (Fick and Hijmans, 2017) and the annual prevailing wind direction for the period between 1979 to 2010 (Chadee and Clarke, 2014). The red contour shows the hydrologic catchment of Lake Izabal (study site). White squares show meteorological stations discussed in this study: A) Puerto Barrios; B) Flores; and C) INSIVUMEH. Black circles show the location of sediment archives mentioned in the text: 1) Rey Marcos cave; 2) Lake Kail; 3) Yok Balum cave; 4) Lake Quexil; 5) Lake Petén-Itzá; 6) Lake Puerto Arturo; 7) Lake Chichancanab; 8) Lake Punta Laguna; 9) Lagoons on the southwest coast of Cuba; 10) Cuba Pequeño speleothem, northwestern Cuba;11) Lake Miragoane; 12) ODP Site SO 164-03-4, central Caribbean Sea; 13) ODP Site VM28-122 from the western Caribbean Colombian Basin; 14) ODP Site 1002 in the Cariaco Basin; 15) ODP Site M35003-4 from the Tobago Basin, southeastern Caribbean Sea.

This study integrates sedimentological and XRF elemental abundance data from a 760-cm-long sediment core collected from Lake Izabal, which has a large catchment that spans most of the highlands and eastern lowlands of Guatemala (Figures 1, 2). We use these analyses to make inferences on hydroclimatic change through the Holocene and then compare the data to other regional proxy-based reconstructions. The Izabal data exhibit several distinct features that suggest that Holocene hydroclimate responses to

ocean-atmosphere circulation changes driven by insolation forcing were heterogeneous across Central America, likely due to the complex interactions between synoptic scale climate phenomena such as the ITCZ, trade-winds, and associated SST variability.

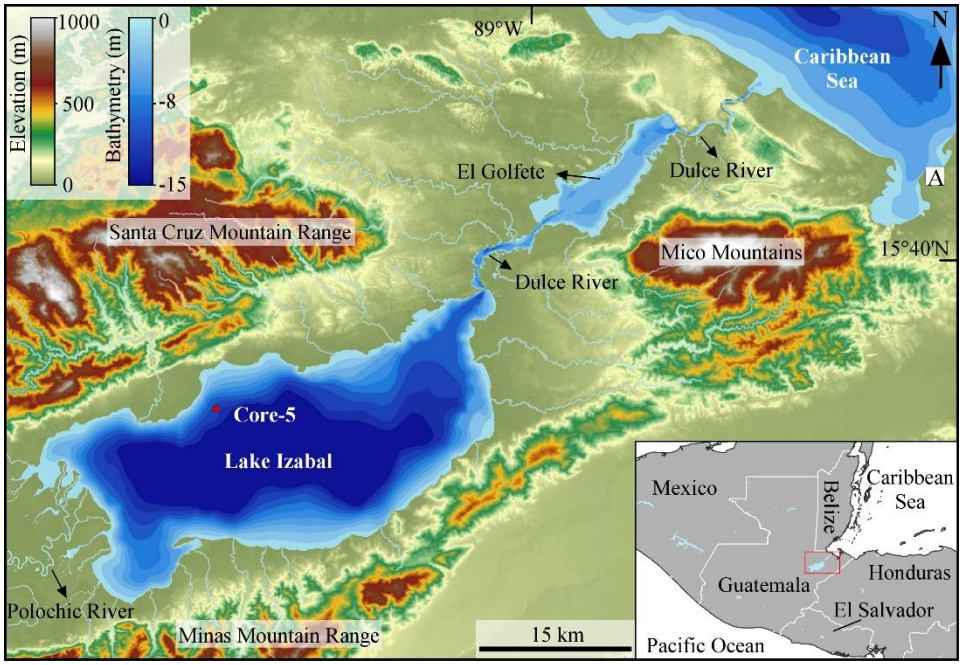

Figure 2. Location of Lake Izabal showing the main topographic features and the bathymetry of the lake. Red dot shows the location of the sediment core (core-5) used for this study. White square labeled with an A shows the location of the meteorological station in Puerto Barrios. Inset map: Location of the study area (red square) covering the central highlands and eastern lowlands of Guatemala.

2. REGIONAL SETTING

Lake Izabal is located between the central highlands and eastern lowlands of Guatemala (Figure 2) and occupies the eastern side of the Lake Izabal pull-apart basin (Obrist-Farner et al., 2020). Lake Izabal is a shallow, hydrologically open, polymictic lake that drains into the Caribbean Sea via the Dulce River (Figure 2). The lake has a

hydrological catchment of 8,740 km^2, a surface area of 672 km^2, a maximum water depth of 15 m (Figure 2), and a mean lake level of ~1.5 m above mean sea level during the wet season (Brinson and Nordlie, 1975; Obrist-Farner et al., 2019). The main tributary is the Polochic River (Figure 2), which contributes ~70% of the water input (Brinson and Nordlie, 1975).

Modern observations indicate that seasonal lake-level fluctuations, lake water chemistry, and lake productivity are all related to changes in regional precipitation (Brinson and Nordlie, 1975). Data from a meteorological station in the Izabal region (Figure 3A) indicate that precipitation is seasonal, with an annual mean of 3,321 mm yr^{-1}, around two times more than that of Flores in the Petén region (1,806 mm yr^{-1}; Figure 3B), and around three times more than that of Guatemala City (1,278 mm yr^{-1}; Figure 3C). The rainy season in Izabal commences in May and lasts until November.

Rainfall in Central America is principally controlled by the position and strength of the ITCZ, which is modified through interaction with the Caribbean Low Level Jet (CLLJ; defined as a maximum of easterly zonal wind at 925 hPa in the central Caribbean region; Wang, 2007; Martinez et al., 2019). Interannually, ITCZ mean position is largely determined by variability in eastern Pacific SST, with positive El Niño Southern Oscillation (ENSO) phases resulting in a more southerly mean position and, consequently, a weakened influence of the ITCZ on western Caribbean precipitation, and vice versa. The CLLJ results from the intensification of easterly winds by the North Atlantic Subtropical High (NASH) pressure system (Wang, 2007) and when strengthened tends to suppress the incursion of the Pacific ITCZ into the western Caribbean and weaken the Atlantic ITCZ, resulting in reduced precipitation.

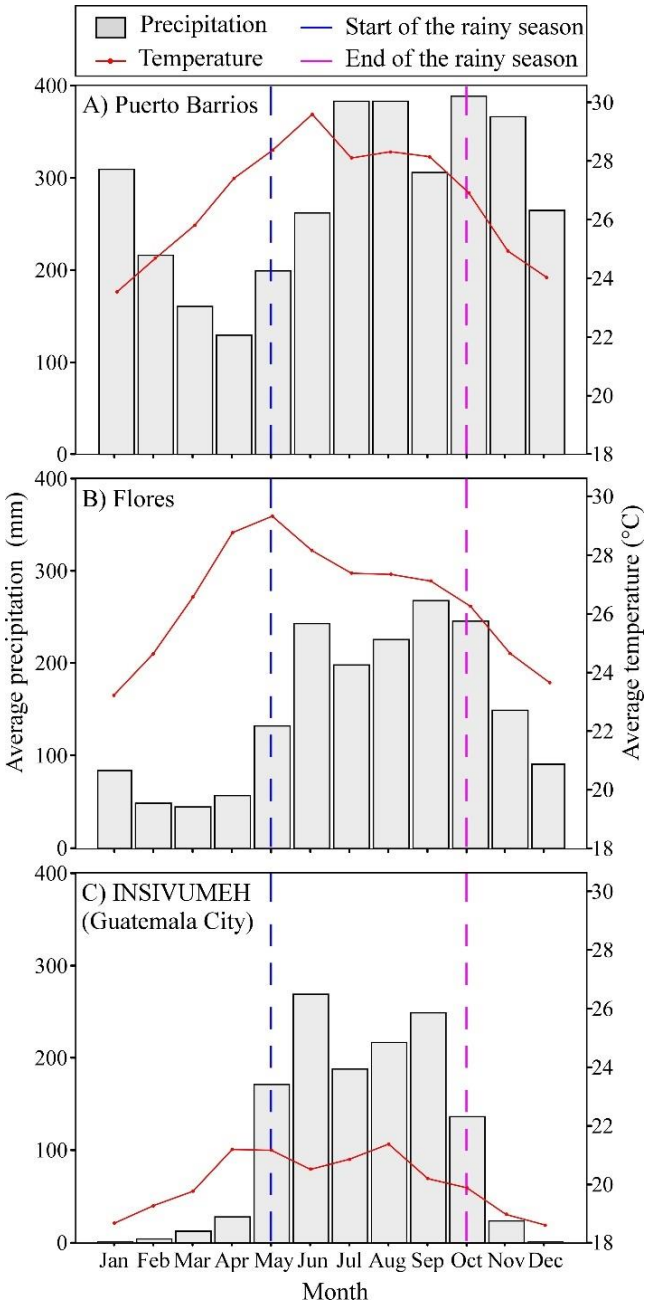

Figure 3. Monthly precipitation and temperature data from meteorological stations A) Puerto Barrios (for the period between 1980 and 2020); B) Flores (for the period between 1980 and 2018); and C) INSIVUMEH in Guatemala City (for the period between 1980 and 2019). See Figure 1 for station locations. Data made available by the National Institute of Seismology, Vulcanology, and Meteorology of Guatemala (INSIVUMEH, 2020). Vertical blue and purple lines show the start and end of the rainy season in Guatemala, which is clearly evident in precipitation data from Guatemala City.

The CLLJ varies intra-annually, peaking in strength during mid-summer and winter, coincident with the mid-summer and winter dry seasons, and waning during the spring and fall, in concert with the late-spring/early-summer and late-summer wet seasons, respectively (Figure 3; Martinez et al., 2019). In the western Caribbean, the CLLJ promotes orographic uplift, zonal convergence and moisture transport via southeasterly winds, which partially offsets its suppression of the ITCZ, leading to a mid-summer drought that is less pronounced than elsewhere or absent altogether, as is the case at Izabal (Figure 4).

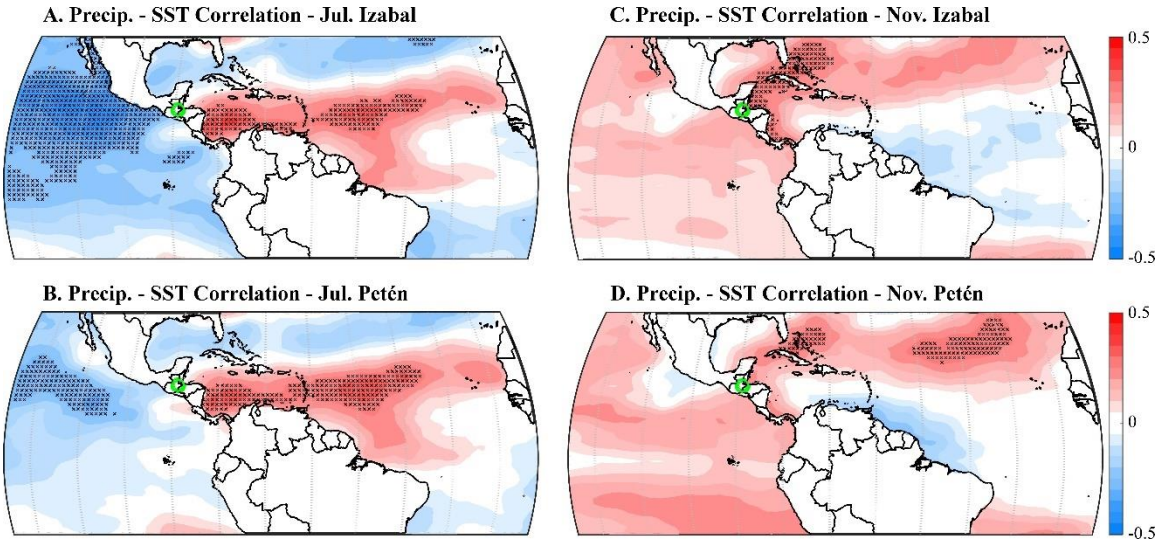

Figure 4. July (A and B) and November (C and D) correlation (Pearson's r) between SST and precipitation for the grid cells within which Lake Izabal and Lake Petén Itzá are located (see methods). Hatching marks locations where the correlation is significant ($p < 0.05$). The green circle shows the location of Lake Izabal. The correlation time period is 1950-2016.

On both intra- and inter-annual timescales, Atlantic Warm Pool (AWP; greater than 28.5 °C) variability is a strong control on CLLJ intensity and moisture availability in

the Caribbean (Muñoz et al., 2008), with warmer SST producing higher sea-level pressure, weaker CLLJ easterlies, and more precipitation at Izabal, and vice versa (Figure 4). Providing a moisture source through enhanced evaporation, the AWP develops in the western Caribbean during the late spring, reaches its greatest extent in September (covering the entire Caribbean), and then shifts westward and dissipates through the fall. During November, anticyclonic circulation from the NASH promotes a shift in low-level winds to easterly, producing orographic uplift and zonal convergence along the eastern coast of Central America, with warmer SST in the western Caribbean leading to greater precipitation amounts (Figure 4).

3. MATERIAL AND METHODS

3.1. OBSERVATIONAL CLIMATE DATA ANALYSIS

The precipitation time series used in the correlation maps (Figure 4) are the mean of three gridded data products (all with 0.5 degree spatial resolution) spanning the time period 1901-2016: University of Delaware v5.01 01 (Willmott and Matsuura, 2001); Global Precipitation Climatology Center V7 (Schneider et al., 2011); and University of East Anglia CRU TS v. 4.03i (Harris et al., 2014). Precipitation at Izabal and Petén Itzá was determined by selecting the individual grid cells within which the lakes are located. SST data are from COBE-SST2 (1-degree resolution; Hirahara et al., 2014). Correlations (Pearson's r) were determined over the time period 1950–2016, with significance estimated by taking into account autocorrelation in the data and adjusting the degrees of freedom accordingly.

3.2. CORE COLLECTION AND ANALYSES

In 2018, a 760-cm-long sediment core (core-5) was retrieved from Lake Izabal from a water depth of 12 m (Figure 2; 15°31'48"N, 89°13'52"W) using two modified piston corers; one specialized for mud-water interface sediments (MWI; Fisher et al., 1992) and one for deeper, more consolidated sediment (Deevey, 1965). The uppermost 75 cm were retrieved with the MWI core, sectioned at 3 cm intervals, and stored in Whirl-Pak® bags. Successive consolidated sediment sections, beginning at 100 cm depth, were retrieved using the second, modified piston corer. Adverse weather (wind and waves) prevented the deployment of casing to the intended depth of 50 cm, leaving a gap of 25 cm (75 to 100 cm) between the MWI core and the deeper core section.

Consolidated whole-core segments were scanned using a Geotek Multisensor Core Logger loop sensor (MSCL-S) to measure sediment density and magnetic susceptibility (MS) at 1 cm resolution at the University of Florida. Afterward, cores were cut and split in half lengthwise to obtain line scan images using the Geotek Geoscan-III. Sediment core description was based on color, bedding, bedding plane contacts, sedimentary texture and structure, and fossil content and recorded and plotted using the package for stratigraphic data analysis in R (SDAR; Ortiz and Jaramillo, 2018). Lithological characteristics were used to subdivide the core into six zones.

Chronological control for core-5 was established using accelerator mass spectrometry (AMS) analysis of 10 terrestrial wood fragments and one mollusk fragment at the Center for Accelerator Mass Spectrometry (CAMS), Lawrence Livermore National Laboratory. All dates were calibrated using IntCal20 (Reimer et al., 2020) and an age-

depth model constructed using the Bayesian software Bacon in R (Blaauw and Christen, 2011).

For X-ray fluorescence (XRF) analyses and X-radiographic imaging, the split-cores and MWI samples were scanned at the Large Lakes Observatory at the University of Minnesota-Duluth using an Itrax XRF core scanner. Elemental scans for consolidated sediment sections were carried out at a 0.5 cm resolution, using a Cr source tube at 30 kV and 55 mA, with 15-second dwell time. The MWI samples were homogenized in the Whirl-Pak® bags before being packed into half of a plastic 2-cm^2 paleomagnetic sample cube, and scanned (20 measurements per sample), using the above specifications. All raw data were reprocessed to optimize peak fitting using QSpec 8.6.0 software. The XRF dataset, given in count per second (cps), was smoothed using a 5-point moving average. XRF ratios were plotted using a log scale to avoid asymmetry related to ratios.

Principal component analysis (PCA) was performed using selected elements to summarize the relationship between elemental variables. Elemental counts were standardized before PCA analysis to avoid confounding effects of dimensional heterogeneity. Original elements are represented by vectors in the dimensional space defined by the principal components, with vector length indicating the amount of variance of each element, and angles among vectors indicating the association among them (Jolliffe, 1986). Thus, the newly defined components can be interpreted in terms of the dominating modes of environmental variability. As samples are assigned scores across the space defined by principal components, their stratigraphic representation provides a synthesis of temporal environmental variability represented by the proxies.

The six stratigraphic zones defined from the core characteristics were further investigated using major geochemical changes (i.e., relationship among elements). We performed moving Procrustes analysis to define statistically significant changes in the relational structure of variables. This analysis compares two PCAs to find differences between the direction and magnitude of vectors that represent elements in each ordination. The test was performed by comparing moving adjacent windows, covering between 200 and 1600 years. Once the main points of change were identified, independent PCA analyses for each of the zones were performed (zonal PCA [zPCA]). Before running zPCA, we constructed correlation matrices for each zone to check for normality and for elemental relationships within zones (Figures S2-S7 in Supplementary Information). MWI data were not included in the PCA analysis because of their lower resolution and inconsistencies in the reading derived from the effects of water content (Tjallingii et al., 2007). PCA and Procrustes analyses were performed using the vegan package (Oksanen et al., 2019) in R.

4. RESULTS

4.1. CHRONOLOGY

The ages of the terrestrial wood samples and the mollusk fragment are all in stratigraphic order, except for two samples in the lower portion of the core (623 and 646 cm) that yielded older ages and one sample at 301 cm that yielded an anomalously young age (Table S1 in Supplementary Information). The deeper samples are within age uncertainties and were included in the model. The shallower sample was obtained 1 cm

below a core break and was likely pushed downward from the younger sediments above during the coring drive. The age for the mollusk fragment was not corrected for a possible hard water effect error. However, the radiocarbon age is within the uncertainty of the model, suggesting minimal hard water error in the sample. Sedimentological and geochemical results are discussed using the weighted mean ages from the model and the 95% confidence intervals reported for each zone (Table S1).

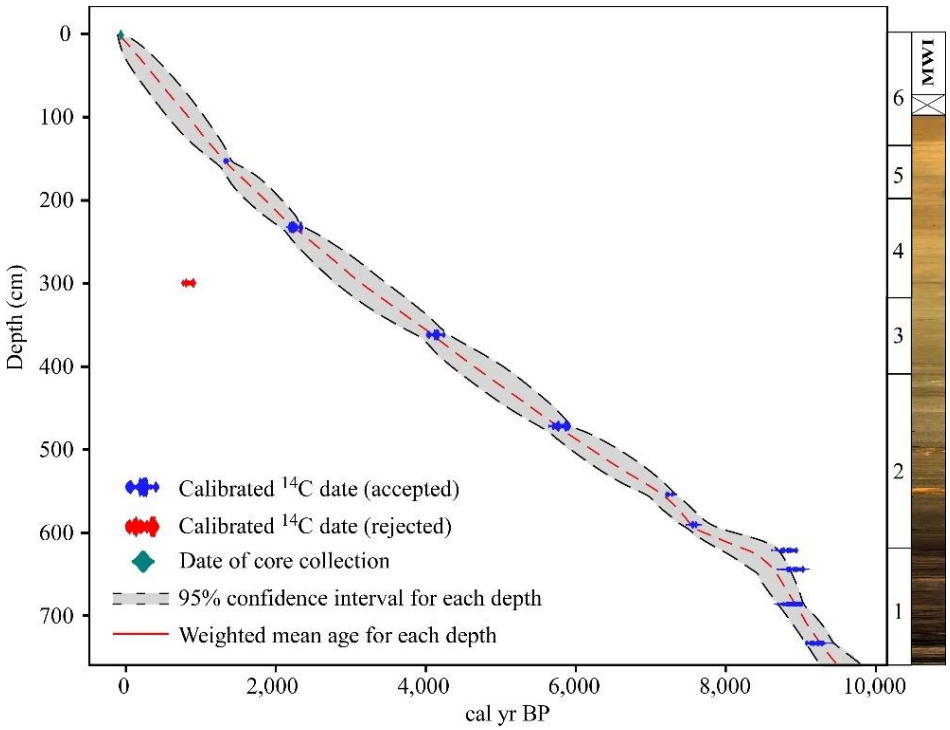

Figure 5. Age-depth model based on ten calibrated radiocarbon dates (blue) generated using Bacon package in R (Blaauw and Christen, 2011). MWI = mud water interface.

4.2. SEDIMENTOLOGY AND GEOCHEMISTRY OF CORE-5

Core-5 from Lake Izabal was subdivided into six stratigraphic zones based on lithological characteristics (Figure 6). The zonation is further supported by XRF data

(Figure 7; Figure S1; Table S2), PCA (Figure 8), and Procrustes analyses that indicates major geochemical changes in the relationships among elements across the sedimentological boundaries (Figure 9).

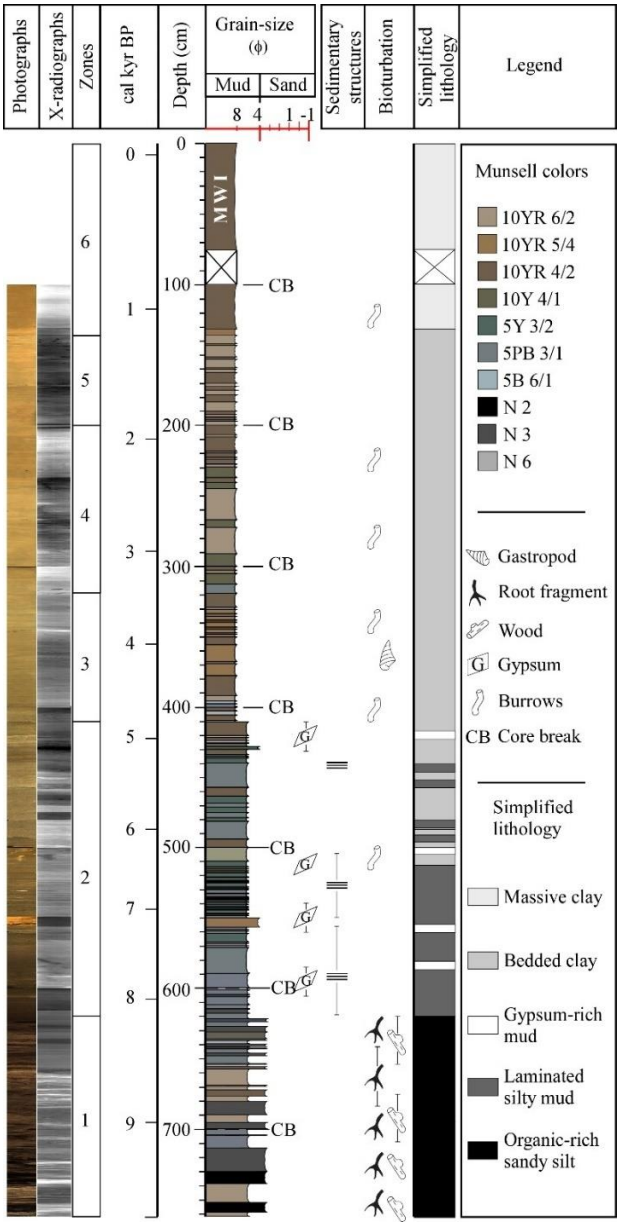

Figure 6. Sedimentological description and simplified lithology versus age for core-5, showing X-radiographs, line scan photographs, color, sedimentary texture and structure, and fossil content.

4.2.1. Zone 1 (760 – 620 cm; 9,500 [9,740-9,300] – 8,300 [8,640-7,990] cal yr BP). Zone 1 (Z1) is characterized by organic-rich silt with abundant wood fragments. This zone is thinly bedded with some thickly laminated intervals (Figure 6). PC1 and PC2 scores increase from -0.8 to -0.1 and -0.2 to 0.1, respectively (Figure 8). Zonal PCA (Figure 9) shows that the main mode of variability is associated with Ti, K, Al, Si, Fe, Ca, and Mn (Figure S2). Whereas the first six elements point towards the positive end of the axis, Mn is negatively correlated (Figure 9). S was independent from these elements, pointing towards the positive end of zPC2 (Figures 7, 9). MS and density are low at the bottom of the section and increase slightly in the upper part, with MS increasing from 4.5 to 14 SI and density increasing from 1.16 to 1.26 g cm^{-3} (Figure 7). The log(Ca/Ti) ratio is characterized by an increasing trend, whereas the log(Fe/Ti) ratio is high in the lower part and decreases in the upper part of the zone (Figure 7).

4.2.2. Zone 2 (620 – 410 cm; 8,300 [8,640-7,990] –4,800 [5,130-4,540] cal yr BP). The transition to Z2 is characterized by a sharp contact between the organic-rich silt of Z1 to thinly laminated mud. This zone is characterized by the appearance of sub-mm laminae with some rich in gypsum. Laminae are persistent throughout the interval until ca. 6,000 cal yr BP. From ca. 6,000 to ca. 4,800 cal yr BP, laminae are less abundant and are interbedded with homogeneous mud (Figure 6). PC1 scores increase from -0.5 to 0.09, while PC2 scores remain fairly constant with two prominent peaks (Figure 8). Ti, K, Al, Si, and Mn have an upward-increasing trend and are positively correlated (Figures 7, 9; Figures S1, S3). From Z1 to Z2, S increases abruptly (Figure 7) and is correlated to Ca along zPC2 (Figure 9). Fe aligns with the zPC2 but is negatively correlated with Ca and S (Figure 9). MS remains low throughout the interval with an average value of 8.0

SI, while density increases upward from 1.22 to 1.45 g cm^{-3} (Figure 7). The log(Ca/Ti) ratio decreases sharply from Z1 to Z2 and remains low throughout the zone. The log(Fe/Ti) ratio increases from Z1 to Z2, followed by an overall decreasing trend (Figure 7).

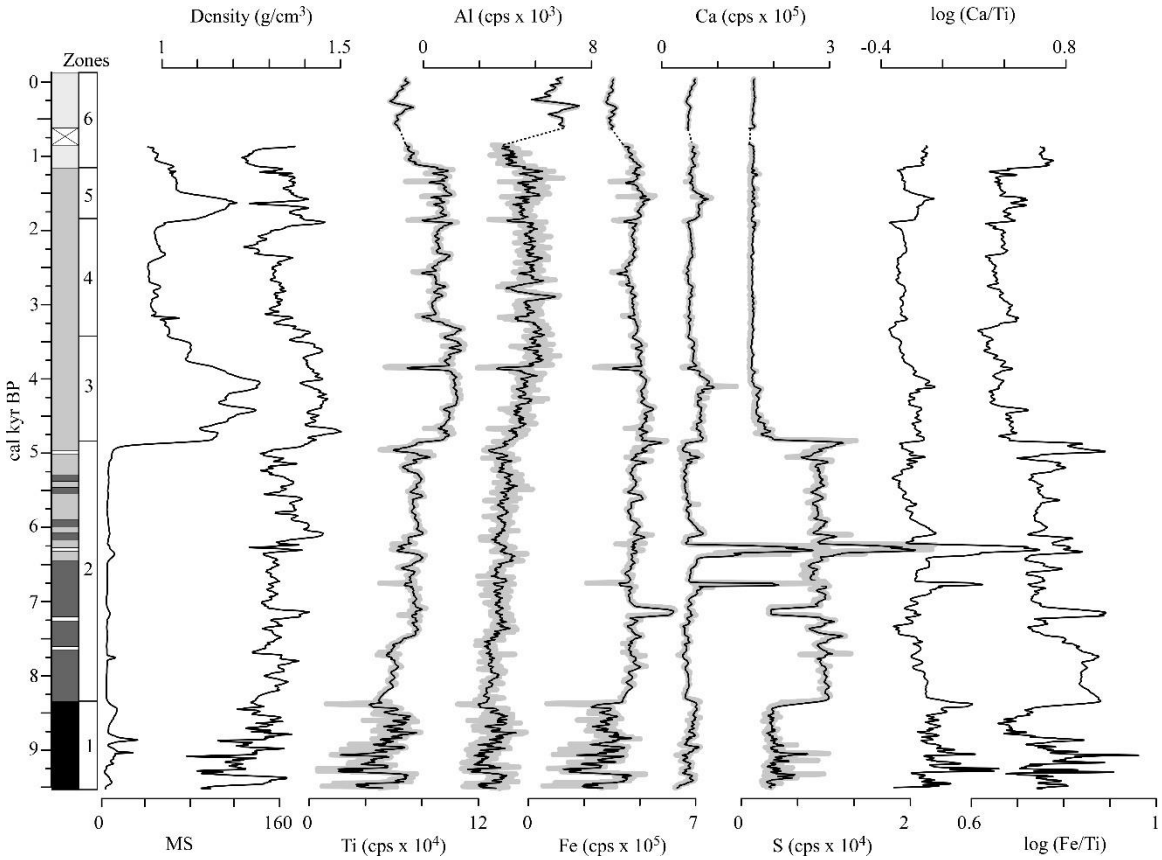

Figure 7. Proxy data and simplified lithology versus age for core-5. Magnetic susceptibility (MS), density, and elemental abundances in counts per second (cps). For elemental abundances, the gray lines show the unfiltered data and black lines show the five-point moving average. Dashed black line highlights intervals where data is missing. See Figure 6 for lithological legend.

4.2.3. Zone 3 (410 – 318 cm; 4,800 [5,130-4,540] –3,400 [3,700-3,130] cal yr BP). The transition to Z3 is characterized by a gradational contact between laminated and

interbedded homogeneous mud in Z2 to bedded mud in Z3 (Figure 6). PC1 scores increase sharply from 0.09 at the top of Z2 to 0.16 at the bottom of Z3 and then increase to 0.4 until ca. 3,400 cal yr BP. PC2 scores are roughly constant at the bottom of the interval, increase for ~300 years at ca. 4,000 cal yr BP and decrease in the uppermost part (Figure 8). The zPCA shows a positive correlation among Ti, Si, Al, and K (Figures 7, 9; Figures S1, S4). Ca and S are positively correlated and associated with the positive end of zPC2 (Figure 9). S decreases abruptly after Z2 and remains low throughout the interval (Figure 7). Fe and Mn are to some extent associated with both components of the zPCA (Figure 9). MS increases rapidly from 97 to 143 SI between ca. 4,800 to ca. 4,000 cal yr BP and then decreases to 62 SI at ca. 3,400 cal yr BP. Density remains high throughout the interval, with an average value of 1.43 g cm^{-3} (Figure 7). The log(Ca/Ti) values are relatively constant between ca. 4,800 to ca. 4,100 cal yr BP and then decrease until ca. 3,400 cal yr BP. The log(Fe/Ti) decreases sharply from Z2 to Z3 and remains low throughout the zone (Figure 7).

4.2.4. Zone 4 (318 – 200 cm; 3,400 [3,700-3,130] –1,800 [2,060-1,680] cal yr BP). The boundary between Z3 and Z4 is marked by a gradational contact from thinly bedded mud to thickly bedded clay (Figure 6). In the lower part of Z4, PC1 scores decrease relative to Z3, and then remain constant with an average value of 0.30, while PC2 scores remain constant, with an average of -0.05 (Figure 8). In the zPCA, Ti, Si, Al, and K remain high (Figure 7) and are aligned towards the positive side of zPC1, whereas Ca, Mn, and Fe are aligned with the positive end of zPC2 (Figure 9; Figure S5). S abundance substantially decreases in Z4, and MS remains constant throughout the zone with an average value of 51 SI (Figure 7). Density is characterized by an upward

decreasing trend from ca. 3,400 to ca. 2,200 cal yr BP (from 1.38 to 1.22 g cm^{-3}), followed by an increasing trend to 1.45 g cm^{-3} towards the top of the interval (Figure 7). Average log(Ca/Ti) and log(Fe/Ti) ratios remain relatively constant in Z4 (Figure 7).

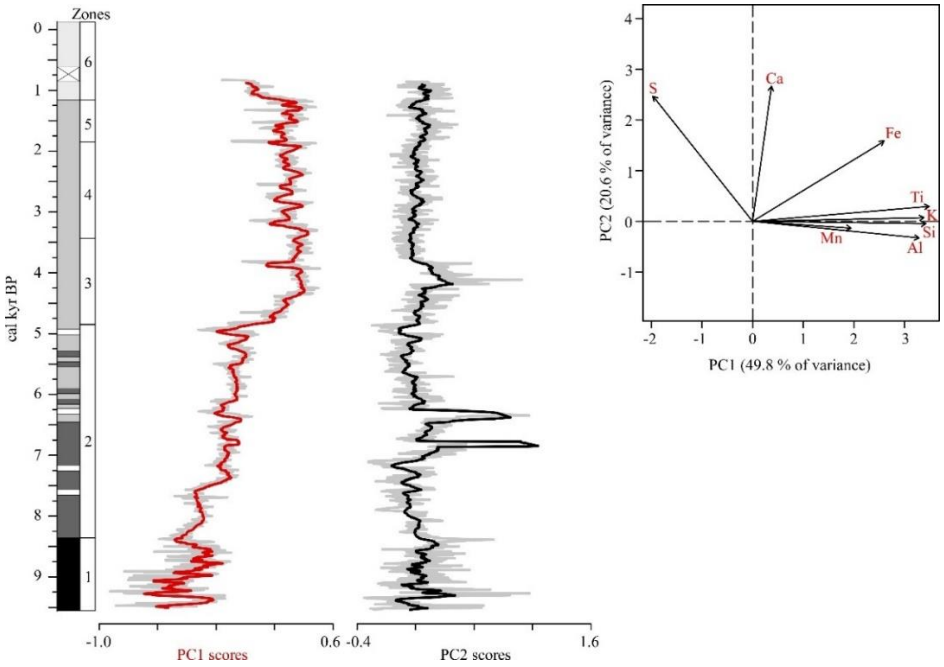

Figure 8. Simplified lithology for core-5 and principal component analysis (PCA). Positive PC1 scores indicate more detrital sediments, whereas positive PC2 scores indicate an increase in authigenic carbonate precipitation. See Figure 6 for lithological legend.

4.2.5. Zone 5 (200 – 136 cm; 1,800 [2,060-1,680]–1,200 [1,290-1,030] cal yr BP). The transition to Z5 is marked by a gradational contact from thickly bedded mud to medium-bedded mud (Figure 6). PC1 scores remain high throughout the zone with an average value of 0.3, while PC2 scores remain relatively constant around an average of 0.01 (Figure 8). XRF results for Z5 indicate high abundance and variability in Ti, Si, K, and Al (Figure 7), which are positively correlated (Figure 9). Ca and Fe align along the

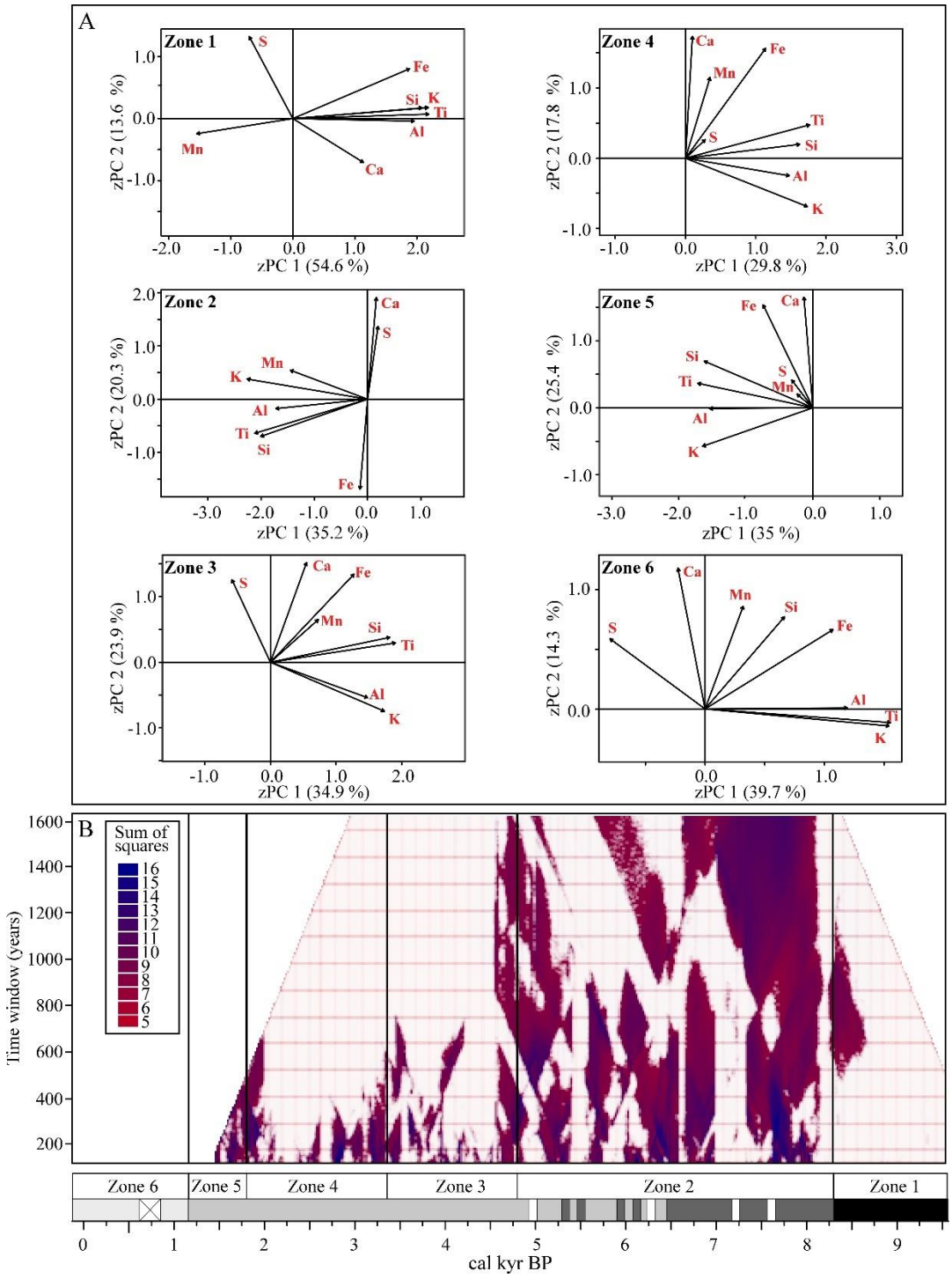

Figure 9. A) Zonal principal component analyses (zPCA) for the six stratigraphic zones. B) Procrustes analysis; light pink regions represent non-significant differences between contiguous intervals of the record at the time scale represented in the y-axis, whereas the magnitude of significant differences is represented by the colored areas. Note how the zonation defined by the sedimentological characteristics are close to the inflection points identified by the Procrustes analyses.

positive side of zPC2, whereas the variability of both Mn and S is low (Figures 7, 9; Figures S1, S6). MS increases from 70 to 125 SI, followed by an upward decreasing trend from 118 to 62 SI. Density decreases from 1.45 to 1.32 g cm^{-3} (Figure 7). The log(Ca/Ti) and log(Fe/Ti) ratios increase slightly until ca. 1,600 cal yr BP and then decrease until ca. 1,200 cal yr BP (Figure 7).

4.2.6. Zone 6 (136 – 0 cm; 1,200 [1,290-1,030] cal yr BP– present). The uppermost section of core-5 is characterized by a sharp boundary from medium-bedded mud to massive brown mud (Figure 6). PC1 scores decrease, changing from 0.4 at the top of Z5 to 0.2 at the bottom of Z6, while PC2 scores remain around 0.03 (Figure 8). In the zPCA, Ti, Al, Fe, and K are aligned along the positive side of zPC1, whereas S is negatively correlated (Figure 9). Ca, Mn, Fe, S and Si are positively correlated and aligned with the positive side of zPC2 (Figures 7, 9; Figures S1, S7). MS decreases from 62 to 42 SI, and density decreases from 1.32 to 1.22 g cm^{-3} until ca. 1,000 cal yr BP (Figure 7). The log(Ca/Ti) ratio increases from -0.24 to -0.09, and the log(Fe/Ti) ratio increases from Z5 to Z6, and remains at an average of 0.75 (Figure 7).

5. DISCUSSION

5.1. PROXIES FOR PALEOENVIRONMENTAL INTERPRETATIONS

The sedimentological and XRF data reveal several abrupt changes in Lake Izabal during the Holocene. Changes in the abundance of terrigenic elements, such as Ti, Al, K, and Si, in lacustrine and marine basins have been related to catchment erosion resulting from precipitation changes (e.g., Haug et al., 2001; Kylander et al., 2011). In Izabal, Ti,

Al, K, and Si align to the positive side of PC1 (Figure 8). We interpret the temporal variation in these terrigenic elements to indicate changes in precipitation and erosion (Figure 8). We also utilized MS and density as proxies for changes in catchment erosion (e.g., Wahl et al., 2006), but the former is known to change due to redox conditions (Nowaczyk et al., 2007; Balascio et al., 2011), thus complicating its interpretation. Ca and S align to the positive side of PC2 (Figure 8), indicating that these are not terrigenic (Figure 9). Studies have used Ca abundance to estimate authigenic carbonate mineral production (Mueller et al., 2009; Kylander et al., 2011), which often occurs during dry conditions (Mueller et al., 2009). Sulfur abundance has been used as an indicator for the presence of marine waters in isolated lake basins, which prevent mixing of the water column, leading to episodes of bottom-water anoxia (Balascio et al., 2011). Based on the above described relationships, we used the ratio log(Ca/Ti) to infer dry conditions and S abundance to infer the presence of sulfur-rich waters and bottom-water anoxia in Lake Izabal.

Changes in Fe abundance indicate terrigenous sediment input, but Fe abundance can also be influenced by redox processes. This is further supported by Fe variations in the zPCA results, showing that Fe, in certain intervals, is decoupled from immobile terrigenic elements (e.g., Zone 2; Figure 9). Thus, we infer that changes in redox conditions in the lake are reflected by shifts in the log(Fe/Ti) ratio. Our inference is supported by the negative correlation between log(Fe/Ti) and MS values (Figure 7), which can indicate redox controlled alteration of magnetite (Nowaczyk et al., 2007).

5.2. HOLOCENE PALEOENVIRONMENTAL RECONSTRUCTION

The abundance of woody fragments and organic-rich silt in Z1 (ca. 9,500-8,300 cal yr BP; Figure 6) suggests that during the early Holocene Lake Izabal was a shallow lake, supported by high log(Ca/Ti). The high log(Fe/Ti) ratio at the bottom of the core (Figure 7) indicates episodes of bottom water anoxia in the lake at that time, supported by low MS values. The decrease in log(Fe/Ti) and a slight increase in MS suggest that anoxia was reduced in the uppermost part of Z1.

The abrupt changes observed between Z1 and Z2 at 8,300 cal yr BP, such as the appearance of laminae, the rapid increase in S, and the abrupt increase in log(Fe/Ti) (Figures 6, 7), suggest the establishment of bottom water anoxia and the presence of sulfur-rich waters. Decoupling of Fe from terrigenic-derived elements (Figure 9) indicates that redox conditions influenced Fe abundance in the sediment. The gradual decrease in the log(Fe/Ti) ratio, however, indicates episodic reintroduction of oxygen to bottom waters, supported by the occasional disappearance of laminations in the upper part of Z2.

The transition from laminated to homogeneous mud, the rapid increase in MS, PC1 scores, and Ti, and a rapid decrease in S and in the log(Fe/Ti) ratio after Z2 (ca. 4,800 cal yr BP; Figures 6, 7), indicates an increase in erosion, a change from anoxic to oxic bottom waters, and decrease in S abundance. From Z3 to the present, the presence of homogeneous mud and minimal variations in log(Ca/Ti) and log(Fe/Ti) indicate that Lake Izabal has been a freshwater lake since ca. 4,800 cal yr BP.

The rapid increase in MS in Z5 (ca. 1,800 cal yr BP), with negligible changes in Ti, Al, K, and Si and in the PC1 scores, could be a signal of anthropogenic disturbance.

Archeological investigations have found that burning associated with forest clearance can enhance MS in soils (e.g., Tite and Mullins, 1971). Archeological investigations in the Izabal area indicate that Maya settlements were common at ca. 2,000 cal yr BP (Voorhies, 1971). However, the first peak in MS at ca. 4,800 cal yr BP (Z3) occurs ~2,800 years before any known Maya occupation in Lake Izabal. This peak is also associated with an increase in Ti (Figure 7) and in the PC1 scores (Figure 8), as well as with a relatively anomalous zonal PCA result (Figure 9). These observations suggest the potential for human settlements in the Izabal area during that time, similar to other locations in the Maya lowlands that show catchment disturbance during the middle Holocene (e.g., Leyden, 2002; Wahl et al., 2014). Development of the pollen record in Lake Izabal could help clarify the relationships between proxy data variability and human occupation.

5.3. PALEOCLIMATIC RECONSTRUCTION AND REGIONAL CORRELATIONS

We compared the XRF elemental abundances and the PCA scores with other records from Guatemala, Mexico, and the Caribbean region in order to assess spatiotemporal trends in hydroclimate during the Holocene. Low lake levels in Izabal during the early Holocene are coincident with the lowest PC1 scores and Ti abundance values of the entire record, indicating minimal catchment erosion/precipitation (Figure 10). Low lake levels during the early Holocene were common throughout the region, as indicated by records from Petén Itzá in northern Guatemala and the Yucatan Peninsula (e.g., Hodell et al., 1995; Mueller et al., 2009). Low precipitation at this time is also supported by the presence of gypsum beds in Lake Puerto Arturo (Wahl et al., 2006), and

high $\delta^{18}O$ from the Rey Marcos speleothem in the central highlands of Guatemala (Winter et al., 2020). Records from the western Caribbean also indicate low precipitation, shown by high $\delta^{18}O$ in the Cuba Pequeño speleothem in Cuba (Fensterer et al., 2013).

The abrupt change at ca. 8,300 cal yr BP (from Z1 to Z2) observed in the sediment record was accompanied by an overall increase in the PC1 scores and a progressive increase in Ti (Figure 10), both indicating intensification of erosion and precipitation at that time. This inferred increase in precipitation is similar to the pattern suggested by data from Petén and several Caribbean records that indicate an increase in moisture availability during the early- to mid-Holocene (Hodell et al., 1991; Haug et al., 2001; Hillesheim et al., 2005; Mueller et al., 2009; Horn, 2011; Fensterer et al., 2013). Furthermore, the Rey Marcos record from the Guatemalan highlands indicates an increase in precipitation ca. 9,000 cal yr BP (Winter et al., 2020). The slight increase in both PC1 scores and Ti abundance during the mid-Holocene indicates that precipitation slightly increased until ca. 4,800 cal yr BP (Figure 10). This is in contrast to records from the Cariaco Basin (Haug et al., 2001) and Lake Petén Itzá (Hillesheim et al., 2005) that indicate an overall drying trend after ca. 8,000 cal yr BP, both hypothesized to have resulted from a southward displacement of the ITCZ in response to declining summer insolation (Figure 10).

The overall increase in terrigenic-derived elements and PC1 scores (Figures 7, 8) at ca. 4,800 cal yr BP indicates an intensification in catchment erosion at that time. Our inference is supported by records from the Caribbean region, such as the $\delta^{18}O$ records from Lake Miragoane (Hodell et al., 1991) and from the Cuba Pequeño speleothem (Fensterer et al., 2013), which indicate higher precipitation during the mid-Holocene.

This transition is supported by high precipitation amounts derived from the Rey Marcos speleothem from the highlands of Guatemala (Winter et al., 2020). This pattern differs, however, from the hydroclimate trends indicated by both the Lake Kail $\delta^{18}O$ record from western Guatemala which suggests that dry conditions occurred between 6,000 and 4,100 cal yr BP (Stansell et al., 2020) and from those of the Petén region suggesting a decrease in lake level in Petén Itzá at ca. 4,500 cal yr BP (Hillesheim et al., 2005; Mueller et al., 2009; Figure 10).

High abundances of terrigenic derived elements and PC1 scores indicate that erosion remained high during the mid- to early-Holocene transition, albeit at lower rates than in Z3. The decrease in MS, density, and the slight decrease in Ti and PC1 scores (Figure 10) at ca. 3,400 cal yr BP indicate a reduction in catchment erosion. Stansell et al. (2020) suggest increasing precipitation starting ca. 3,000 cal yr BP in western Guatemala.

Similarly, Winter et al. (2020) inferred persistent wet conditions in the highland area of Guatemala at that time, with a gradual decreasing trend starting at ca. 3,800 cal yr BP (Figure 10). In the Petén region, dry conditions at ca. 3,500 cal yr BP are suggested by an increase in authigenic carbonate and gypsum deposition in Lake Petén Itzá (Hillesheim et al., 2005; Mueller et al., 2009). Several records from the Caribbean region also suggest a drying trend from the middle to the late Holocene. For example, low Ti concentrations in the Cariaco Basin record demonstrate drying starting at ca. 3,400 cal yr BP (Haug et al., 2001), and the oxygen isotope record from Lake Miragoane indicates higher evaporation rates and lower lake levels between 3,200 and 2,400 cal yr BP (Hodell et al., 1991).

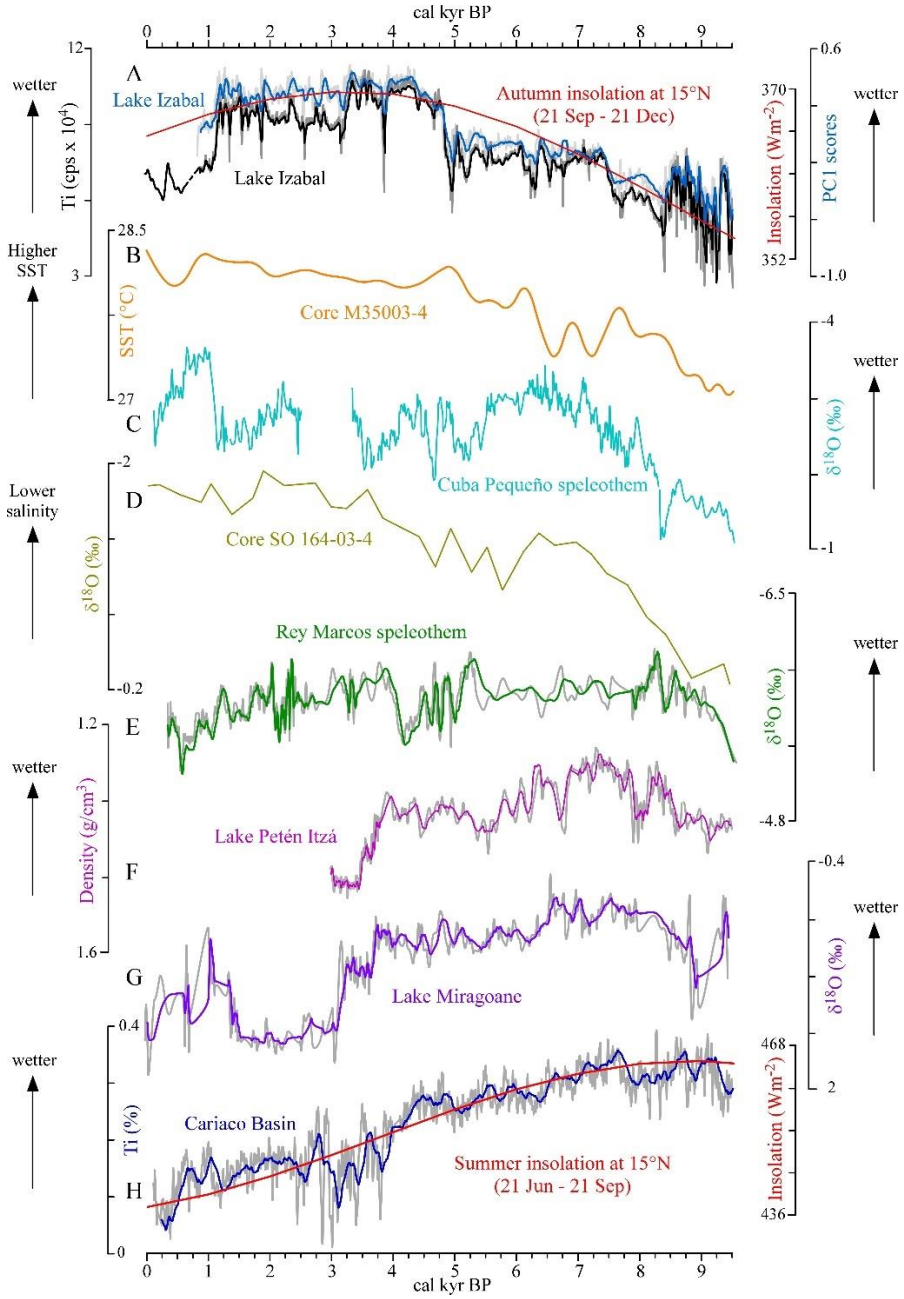

Figure 10. Comparison of Central American and Caribbean precipitation and erosion records. A) Lake Izabal Ti, PC1 scores, and autumn insolation at 15°N. B) Sea surface temperature from the core M35003-4, southeastern Caribbean Sea (Rühlemann et al., 1999); C) $\delta^{18}O$ record from the Cuba Pequeño speleothem, northwestern Cuba (Fensterer et al., 2013). D) $\delta^{18}O$ record from core SO 164-03-4, central Caribbean Sea (Horn, 2011). E) $\delta^{18}O$ record from Rey Marcos speleothem (Winter et al., 2020). F) Density record from Lake Petén Itzá (Hillesheim et al., 2005). G) $\delta^{18}O$ record from Lake Miragoane (Hodell et al., 1991). H) Ti record from the Cariaco Basin (Haug et al., 2001) and summer insolation at 15°N. Insolation curves were calculated after Laskar et al. (2004). See Figure 1 for record locations.

Similarly, sedimentological results from Cuba suggest a decrease in precipitation and the onset of dry conditions at ca. 4,000 cal yr BP (Gregory et al., 2015), similar to the $\delta^{18}O$ record from the Cuba Pequeño speleothem which suggests the onset of drier conditions at ~5,500 cal yr BP that persisted until ~1,200 cal yr BP (Fensterer et al., 2013). Although somewhat inconsistent, these records collectively suggest low precipitation during the late Holocene, potentially due to a southward displacement of the ITCZ in response to a decline in summer insolation (Haug et al., 2001) and to a corresponding increase in eastern Pacific SSTs (Koutavas et al., 2006).

High terrigenic-derived elemental abundances and PC1 scores indicate that erosion remained high during Z5, between 1,800 and 1,200 cal yr BP (Figure 10). Precipitation amounts in the Guatemalan highlands are inferred to have been high at that time but had already started to decrease (Winter et al., 2020). Records from northern Guatemala indicate dry conditions, such as $\delta^{18}O$ from Lake Chichancanab between 2,200 and 1,200 cal yr BP (Hodell et al., 1995) and Lake Punta Laguna between 1,785 and 930 cal yr BP (Curtis et al., 1996).

A decrease in MS, elemental abundances, and PC1 scores at ca. 1,200 cal yr BP suggests a significant reduction in erosion and precipitation at that time (Figure 10). The onset of this drying trend coincides with the well-known Maya droughts (Hodell et al., 1995). Our observations are consistent to those from the Rey Marcos speleothem (Winter et al., 2020) and the nearby Yok Balum speleothem (Kennett et al., 2012), which show pronounced dry conditions during this period. Dry conditions are also inferred for Lake Chichancanab between 1,300 and 1,100 cal yr BP (Hodell et al., 1995), Lake Miragoane

since ca. 900 cal yr BP (Hodell et al., 1991), and in the Cariaco Basin between 1,200 and 1,000 cal yr BP (Haug et al., 2001).

5.4. HOLOCENE HYDROCLIMATE IN EASTERN GUATEMALA

Our sedimentological record from Lake Izabal indicates an increase in erosion and precipitation from the early to the middle Holocene and sustained, high levels of erosion and precipitation until ~1,200 cal yr BP. This result is at odds with several records from Central America and the Caribbean that show a progressive decrease in precipitation from the early through the late Holocene, such as the sediment records from the Cariaco Basin (Haug et al., 2001), Lake Miragoane (Hodell et al., 1991) and Lake Petén Itzá (Hillesheim et al., 2005). Similarities between these records have been explained by invoking a southward displacement of the mean position of the ITCZ during the Holocene (Haug et al., 2001), which is thought to have caused a reduction in regional precipitation. The controlling mechanism is that a decrease in northern tropical summer insolation weakened the inter-hemispheric meridional SST gradient causing the ITCZ to gradually shift southward toward the relatively warmer hemisphere. This was accompanied by an increase in SSTs in the eastern Pacific Ocean, a strengthening of the Pacific zonal SST gradient (e.g., Koutavas et al., 2006), and thus a transition to a more El Niño like mean state of the tropical Pacific Basin. Other records from the western Caribbean, however, suggest that this pattern of Holocene hydroclimatic change was not ubiquitous, challenging the view of meridional shifts in ITCZ position as the sole factor responsible for the inferred precipitation changes. Speleothem records from Cuba (Fensterer et al., 2013) and central Guatemala (Winter et al., 2020) suggest that

alternative processes should be considered, and that it is possible that purported changes in ITCZ position either did not substantially contribute to precipitation variability in some locations or that other factors (as discussed below regarding Izabal) were more influential.

In light of recent studies suggesting that ITCZ width/strength can largely explain spatiotemporal patterns in tropical American precipitation over the last millennium (e.g., Asmeron et al., 2020), one plausible explanation for the decrease in northern tropical precipitation throughout the Holocene inferred from the Cariaco basin record (and supported by data from Lake Miragoane and Petén Itzá), is that a decrease in the strength of the ITCZ, rather than a southerly shift in its mean position, occurred in response to changes in solar insolation. This decrease in strength would have been accompanied by latitudinal expansion, leading to less precipitation in the core region (e.g., in the Cariaco Basin and at Lake Petén Itzá) but greater amounts in locations near the flanks of the ITCZ. Although plausible, this hypothesis is not conclusively supported by several hydroclimatic reconstructions. For example, the lake sediment $\delta^{18}O$ record from Lake Miragoane, located near the edge of the ITCZ zone of influence (Martinez et al., 2019), exhibits a Holocene trend toward drier conditions, when an increase in precipitation (were the ITCZ to have widened considerably) or no change (were ITCZ changes to have not been influential) would be expected under this scenario. Similarly, the Cuba Pequeño speleothem $\delta^{18}O$ record, also from a location near the fringe of ITCZ influence, exhibits marked inconsistency with both the Lake Miragoane and Cariaco Basin records (Hodell et al., 1991; Haug et al., 2001), demonstrating no long-term trend in Holocene precipitation. Furthermore, both the Rey Marcos speleothem (Winter et al., 2020) and

Izabal records, whose sites are located within the present day ITCZ core region, are inconsistent with the expected trend of a progressive decrease in precipitation in the northern tropics in association with a weakening of the ITCZ (Figure 10). These data are, however, insufficient, both in spatial distribution and number of records, for a comprehensive investigation of hypotheses related to ITCZ dynamical changes over the Holocene.

One hypothesis for explaining the precipitation trends inferred from the Izabal data is that the progressive increase in autumn insolation at 15° N (the latitudinal location of Lake Izabal and the central location where the CLLJ originates; Wang, 2007) led to greater AWP SST later into the year. This promoted increased inland moisture delivery through enhanced evaporation, amplifying precipitation associated with zonal convergence and orographic uplift along the eastern coast of Central America, particularly during the fall when the AWP is prominent in the western Caribbean (Figure 4C). This relationship is expressed in observational data through the strong correlation between precipitation at Izabal and regional SST patterns (Figure 10), highlighting the role of SST as a major control on tropical precipitation (e.g., Good et al., 2021). Consistent with this hypothesis, the Caribbean SST records of Rühlemann et al. (1999) and Schmidt et al. (2004) indicate an overall trend toward warmer temperatures through the Holocene (Figure 10). Our hypothesis is also supported by global circulation model results from Bhattacharya et al. (2017) that indicate a potential connection between SST changes in the tropical Atlantic and a decrease in precipitation starting at ~1,200 cal yr BP. Furthermore, our hypothesis partially explains inconsistency between records from the Cariaco Basin (Haug et al., 2001), Lake Miragoane (Hodell et al., 1991), Lake Petén

Itzá (Hillesheim et al., 2005), and Izabal, in that at present, AWP variability during the fall is a strong control on precipitation along the Caribbean coast of Central America, whereas this is not the case at the former three sites (Figure 4). In particular, this is not true for Petén Itzá (Figure 4) due to its location to the west of the Maya Mountains in Belize which partially block moisture-rich, low-elevation Caribbean air masses from penetrating into the interior of the Yucatan. Our modern climatological analyses and Holocene hydroclimate reconstruction from Izabal indicate that substantial spatial heterogeneity in climatology and in paleoclimate reconstructions exists over relatively short distances in Central America, likely due to topographic complexity and interactions with circulation dynamics occurring within both the Atlantic and Pacific basins. Additional proxy records from geographically unrepresented regions and from locations with hydroclimate influenced to varying degrees by seasonal ITCZ dynamics and SST patterns are thus essential for more thorough investigation of the mechanisms relating Central American precipitation responses to insolation forcing through the Holocene.

6. CONCLUSIONS

Analysis of the 760 cm-long sediment core from Lake Izabal provides new insights into Holocene hydroclimatic and paleoenvironmental changes in the eastern lowlands of Guatemala. Our results indicate a transition toward wetter conditions from the early to the latest middle Holocene, and then a relatively stable climate thereafter until ca. 1,200 cal yr BP. Lake Izabal also underwent episodes of bottom-water anoxia as well as possible anthropogenic disturbance in the area starting at ca. 4,800 cal yr BP. The

decrease in MS, elemental abundances, and PC1 scores at ca. 1,200 cal yr BP indicate a significant and abrupt reduction in erosion/precipitation, which corresponds to the well-known Maya droughts. This inferred pattern of hydroclimate change is potentially explainable by a mechanism wherein a progressive increase in autumn insolation throughout the middle and late Holocene drove an increase in Caribbean SST during the latter part of the wet season, which at present, is the wettest time of year in the study area. Warmer SST would have increased moisture availability through enhanced evaporation, amplifying precipitation in the eastern Guatemalan lowlands. Additional paleoclimate records from the Central American region, an area where multiple dynamic oceanic and atmospheric processes converge, are needed to improve our understanding of regional climatic changes related to SST and ITCZ dynamics and to reconcile differences between the Izabal record and other regional paleoclimate datasets.

ACKNOWLEDGMENTS

The authors thank two anonymous reviewers for their valuable comments that significantly improved the quality of this manuscript. This research was supported by two Geological Society of America Graduate Student Research Grants, an American Association of Petroleum Geologists Grants-in-Aid, and the Visiting Graduate Student Travel Grant Program from the National Lacustrine Core Facility and the Continental Scientific Drilling Coordination Office. We thank Robert Brown at the Large Lakes Observatory, and University of Minnesota-Duluth for the XRF analysis.

APPENDIX A.

SUPPLEMENTARY FIGURES

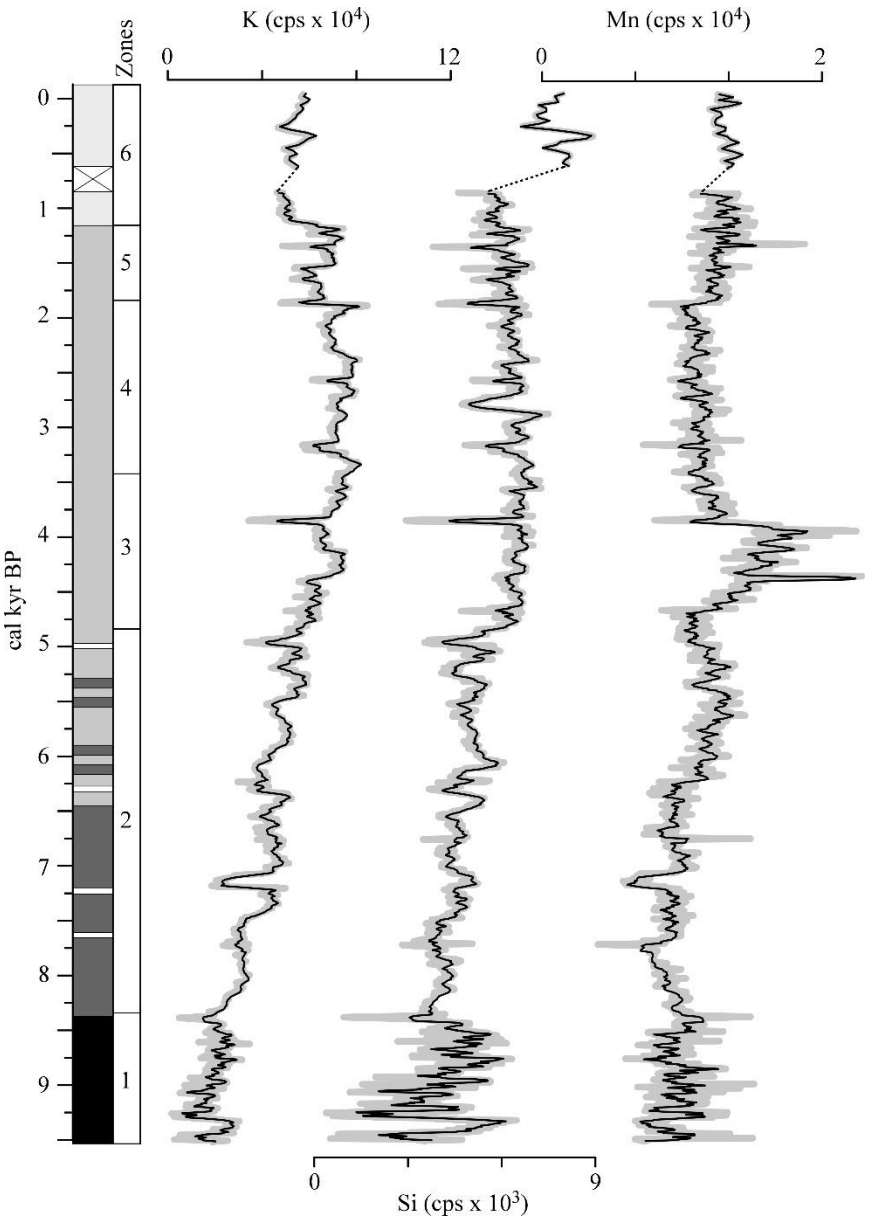

Figure S1. Proxy data and simplified lithology versus age for core-5. Elemental abundances in counts per second (cps). For elemental abundances, the gray lines show the unfiltered data and black lines show the five-point moving average. Dashed black line highlights intervals where data is missing.

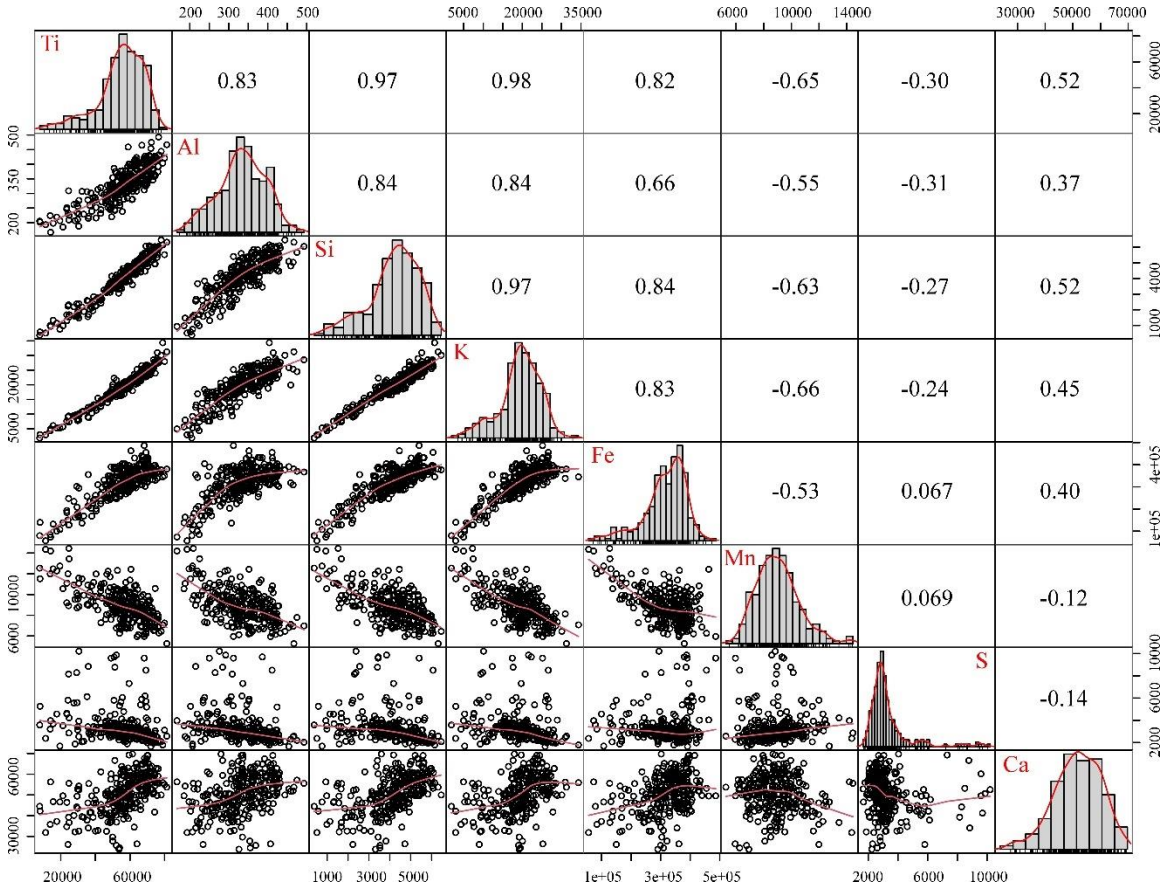

Figure S2. Correlation matrix for Zone 1 (760 to 620 cm). The distribution of each element is plotted as a histogram and elemental relationships are plotted using scatter plots and their relationships calculated using Pearson's r.

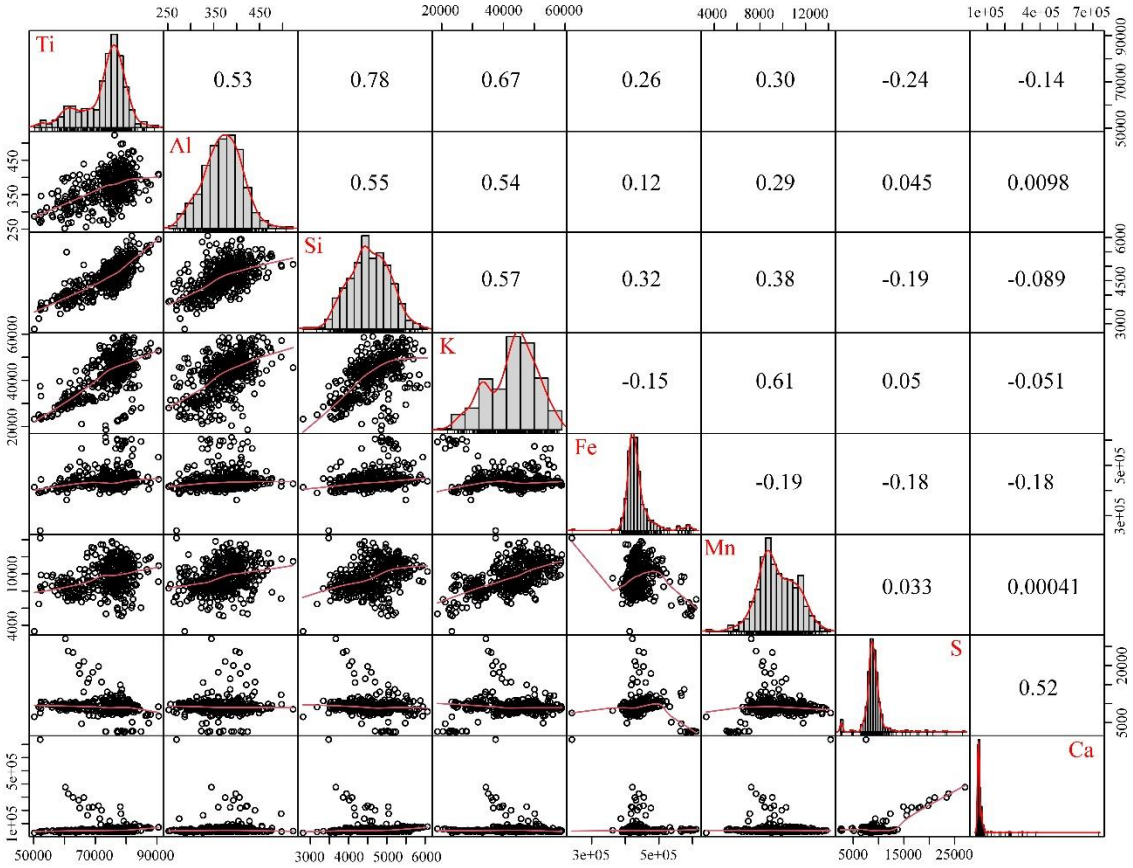

Figure S3. Correlation matrix for Zone 2 (620 to 410 cm). The distribution of each element is plotted as a histogram and elemental relationships are plotted using scatter plots and their relationships calculated using Pearson's r.

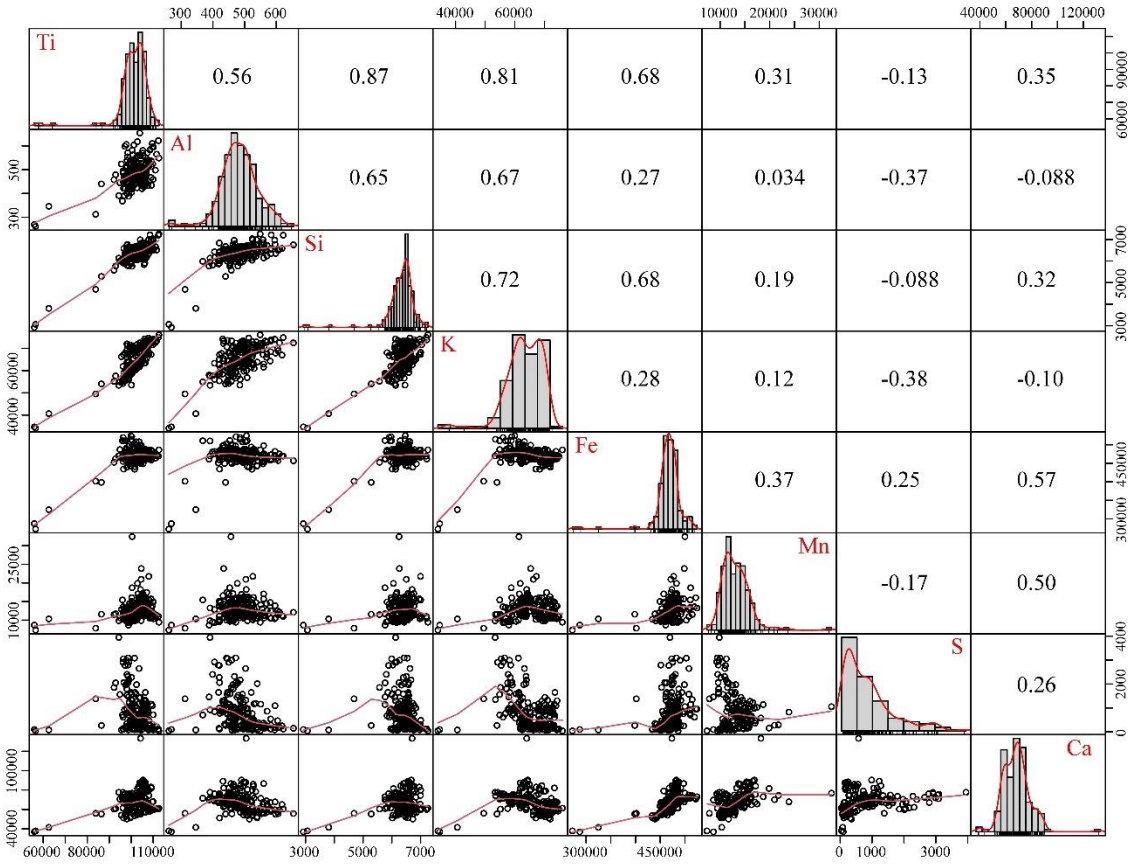

Figure S4. Correlation matrix for Zone 3 (410 to 318 cm). The distribution of each element is plotted as a histogram and elemental relationships are plotted using scatter plots and their relationships calculated using Pearson's r.

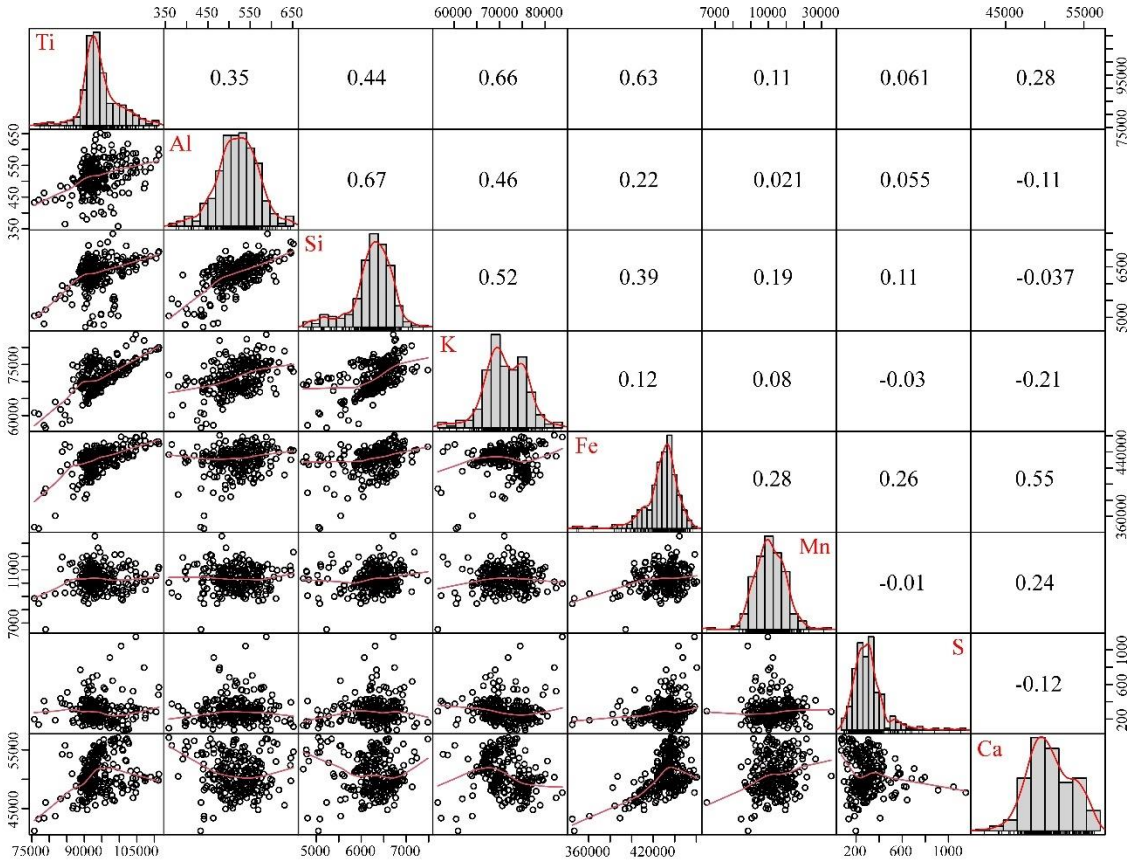

Figure S5. Correlation matrix for Zone 4 (318 to 200 cm). The distribution of each element is plotted as a histogram and elemental relationships are plotted using scatter plots and their relationships calculated using Pearson's r.

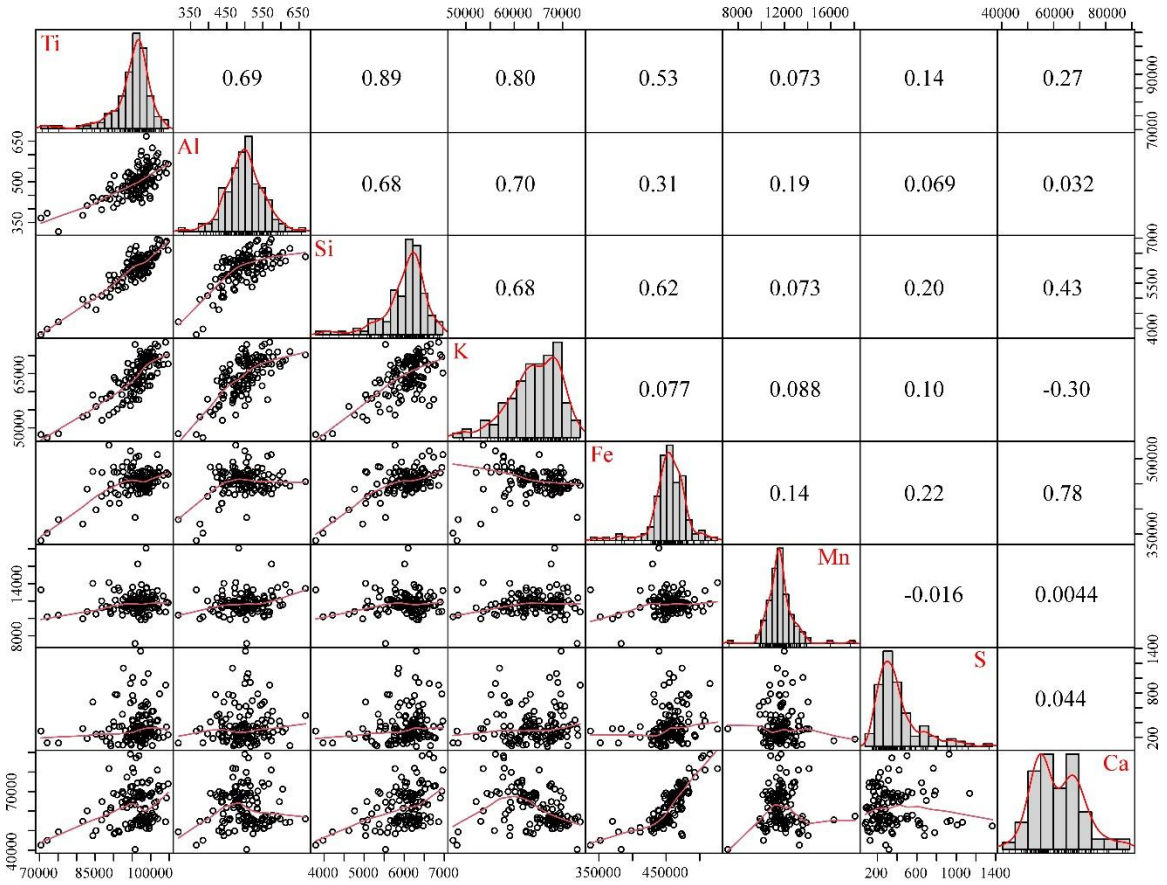

Figure S6. Correlation matrix for Zone 5 (200 to 136 cm). The distribution of each element is plotted as a histogram and elemental relationships are plotted using scatter plots and their relationships calculated using Pearson's r.

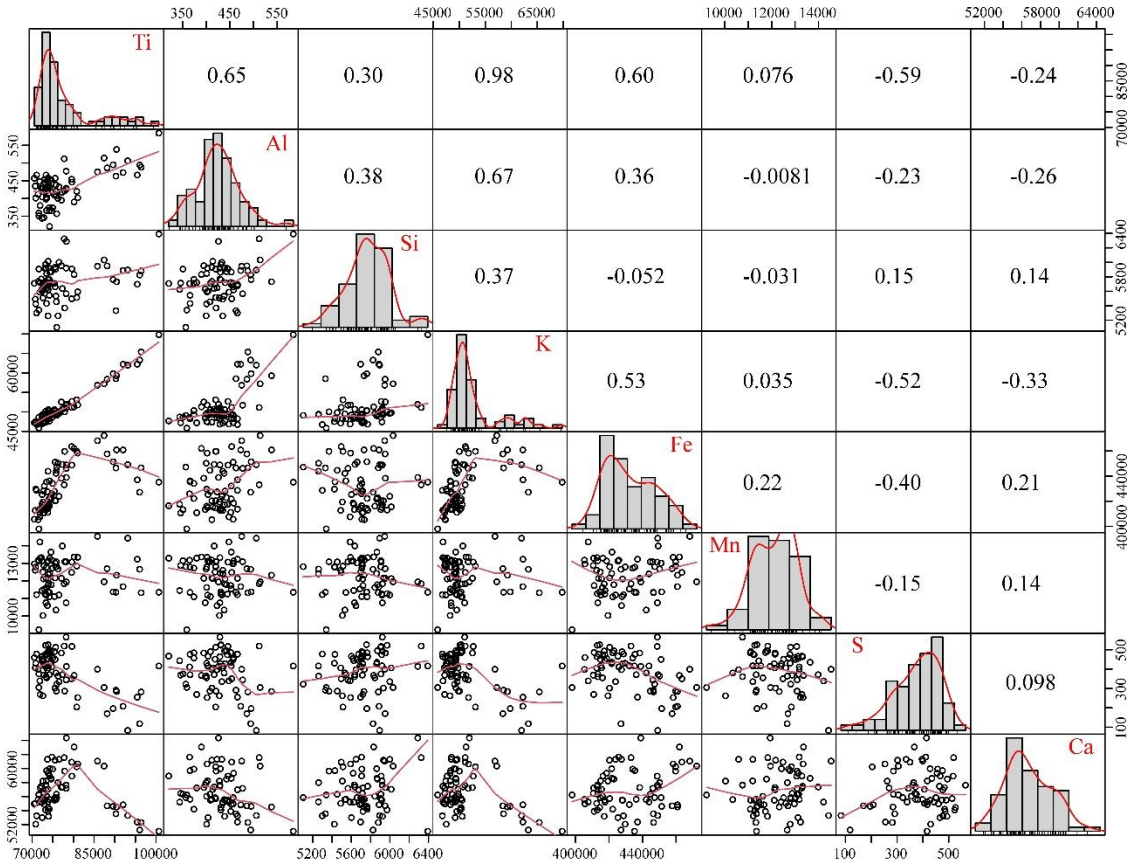

Figure S7. Correlation matrix for Zone 6 (136 to 100 cm). The distribution of each element is plotted as a histogram and elemental relationships are plotted using scatter plots and their relationships calculated using Pearson's r.

APPENDIX B.

SUPPLEMENTARY TABLES

Table S1. Radiocarbon dates on samples from core 5 in Lake Izabal, Guatemala.

Sample type	Accession number	Depth (cm)	^{14}C age	± 1σ	Mean age (cal yr BP)	Error (1σ)	Modeled age (cal yr BP)	95% range (cal yr BP)[b]
Wood fragment	CAMS-180972	153	1415	30	1321	20	1330	1286-1400
Wood fragment	CAMS-180973	232	2240	30	2239	54	2244	2149-2337
Wood fragment[c]	CAMS-180974	301	910	30	840	47	--	--
Mollusk fragment[a]	Beta-545400	362	3750	30	4105	59	4105	3981-4234
Wood fragment	CAMS-180975	473	5020	35	5779	70	5787	5637-5896
Wood fragment	Beta-545401	556	6310	30	7231	37	7190	7030-7288
Wood fragment	CAMS-180976	592	6675	35	7544	31	7591	7493-7739
Wood fragment	Beta-545402	623	8010	30	8885	74	8419	8055-8662
Wood fragment	CAMS-180977	646	8025	40	8891	83	8660	8427-8812
Wood fragment	Beta-545403	688	7970	30	8853	85	8918	8768-8994
Wood fragment	CAMS-180978	735	8205	35	9164	70	9257	9111-9405

[a]Uncorrected for possible hard water lake error

[b]Radiocarbon ages at depth in the core (m below lake floor) were converted into calendar ages (cal yr BP) using IntCal20 and an age-depth model with a 95% confidence range was constructed using Bacon in R (See methods).

[c]Wood fragment was obtained close to a core break, is likely out of place, and was not included in the age-depth model.

Table S2. Raw magnetic susceptibility (MS), density, and X-ray fluorescence (XRF) data.

Depth in core (cm)	Composite Depth in Core (cm)	Calibrated Age (cal yr BP)	MS (SI)	Density (g/cm^3)	Al (cps)	Si (cps)	S (cps)	K (cps)	Ca (cps)	Ti (cps)	Mn (cps)	Fe (cps)
0	0	-68.3										
0.5	0.5	-63.8										
1	1	-59.4										
1.5	1.5	-55.2										
2	2	-50.9										
2.5	2.5	-46.6										
3	3	-42.4			960.35	9287.5	648.35	56828.2	60591.8	70694.8	11860.8	350630
3.5	3.5	-38.1										
4	4	-33.8										
4.5	4.5	-29.6										
5	5	-25.4										
5.5	5.5	-20.9										
6	6	-16.6			912.2	8918.65	557.9	55991.9	58189.8	69783.4	12806.1	345745
6.5	6.5	-12.2										
7	7	-7.7										
7.5	7.5	-3.2										
8	8	1.2										
8.5	8.5	5.5										
9	9	9.9			938.15	8997.4	589.25	58479.8	60542.8	72576.7	11807.8	347530
9.5	9.5	14.3										
10	10	18.6										
10.5	10.5	23.2										
11	11	27.9										
11.5	11.5	32.4										
12	12	37.1			945.15	9055.75	594.4	57141.8	57600.6	70467.9	13362	345463
12.5	12.5	41.6										
13	13	46										
13.5	13.5	50.5										
14	14	54.9										
14.5	14.5	59.3										

Table S2. Raw magnetic susceptibility (MS), density, and X-ray fluorescence (XRF) data. (cont.)

Depth in core (cm)	Composite Depth in Core (cm)	Calibrated Age (cal yr BP)	MS (SI)	Density (g/cm^3)	Al (cps)	Si (cps)	S (cps)	K (cps)	Ca (cps)	Ti (cps)	Mn (cps)	Fe (cps)
15	15	63.8			870.15	8267.3	640.2	54619.7	53428.2	67314.4	12568.2	338426
15.5	15.5	68.6										
16	16	73.3										
16.5	16.5	78.1										
17	17	83										
17.5	17.5	87.6										
18	18	92.5			911.4	8582.85	534.7	55965.4	54525.9	68853.4	11270.3	347930
18.5	18.5	97.3										
19	19	102.1										
19.5	19.5	106.9										
20	20	111.8										
20.5	20.5	116.7										
21	21	121.6			897.6	8579.85	632.75	54865.4	50534.9	65856.1	11951.2	347299
21.5	21.5	126.5										
22	22	131.4										
22.5	22.5	136.3										
23	23	141.1										
23.5	23.5	145.9										
24	24	150.8			851.15	8187.7	645	53181.1	49826.9	64239.5	12051.2	330088
24.5	24.5	155.6										
25	25	160.3										
25.5	25.5	164.9										
26	26	169.4										
26.5	26.5	174										
27	27	178.5			833.05	8266.55	620.4	52701.9	50562.7	64744.7	11661	333306
27.5	27.5	183.1										
28	28	187.6										
28.5	28.5	192.3										
29	29	196.8										
29.5	29.5	201.3										

Table S2. Raw magnetic susceptibility (MS), density, and X-ray fluorescence (XRF) data. (cont.)

Depth in core (cm)	Composite Depth in Core (cm)	Calibrated Age (cal yr BP)	MS (SI)	Density (g/cm^3)	Al (cps)	Si (cps)	S (cps)	K (cps)	Ca (cps)	Ti (cps)	Mn (cps)	Fe (cps)
30	30	205.9			875.05	8709.2	768.75	51076	46580.4	62912.9	11555.9	324336
30.5	30.5	210.4										
31	31	214.8										
31.5	31.5	219.3										
32	32	223.7										
32.5	32.5	228.2										
33	33	232.7			812.75	8303.15	621.45	49686.2	45435.1	62039.4	11598	327222
33.5	33.5	237.2										
34	34	241.6										
34.5	34.5	246.1										
35	35	250.6										
35.5	35.5	255.2										
36	36	259.9			739.5	7540.85	689.4	46264.7	43754.6	59220.7	12292.5	318485
36.5	36.5	264.5										
37	37	269.2										
37.5	37.5	273.9										
38	38	278.6										
38.5	38.5	283.2										
39	39	287.9			880.75	8803.25	570.65	50513.6	45659.9	63045.2	12267.5	326648
39.5	39.5	292.7										
40	40	297.3										
40.5	40.5	301.9										
41	41	306.5										
41.5	41.5	311.2										
42	42	315.8			1001.7	9779.25	538.95	57439.1	50214.5	71012.9	11679.8	352031
42.5	42.5	320.3										
43	43	324.9										
43.5	43.5	329.5										
44	44	334.1										
44.5	44.5	338.7										

Table S2. Raw magnetic susceptibility (MS), density, and X-ray fluorescence (XRF) data. (cont.)

Depth in core (cm)	Composite Depth in Core (cm)	Calibrated Age (cal yr BP)	MS (SI)	Density (g/cm^3)	Al (cps)	Si (cps)	S (cps)	K (cps)	Ca (cps)	Ti (cps)	Mn (cps)	Fe (cps)
45	45	343.2			1080.35	10392.7	505.9	61093	52283.4	75826.2	12415.8	364539
45.5	45.5	347.8										
46	46	352.3										
46.5	46.5	356.9										
47	47	361.5										
47.5	47.5	366.1										
48	48	370.6			1018.8	10179	459	57641.9	50540.9	70134.9	12644.4	355020
48.5	48.5	375.1										
49	49	379.7										
49.5	49.5	383.9										
50	50	388.3										
50.5	50.5	393										
51	51	397.7			955.65	9152.6	503	56057.4	48963.2	69076.5	13201	339546
51.5	51.5	402.4										
52	52	407.1										
52.5	52.5	411.8										
53	53	416.6										
53.5	53.5	421.2										
54	54	426			934.75	8982.45	583.65	53866.4	48519.9	67543.4	12497.7	355734
54.5	54.5	430.7										
55	55	435.4										
55.5	55.5	440										
56	56	444.6										
56.5	56.5	449.2										
57	57	453.7			857.25	8422.75	448	48726.4	46984.3	64141.6	12030.7	346709
57.5	57.5	458.2										
58	58	462.7										
58.5	58.5	467.2										
59	59	471.7										
59.5	59.5	476.2										

Table S2. Raw magnetic susceptibility (MS), density, and X-ray fluorescence (XRF) data. (cont.)

Depth in core (cm)	Composite Depth in Core (cm)	Calibrated Age (cal yr BP)	MS (SI)	Density (g/cm^3)	Al (cps)	Si (cps)	S (cps)	K (cps)	Ca (cps)	Ti (cps)	Mn (cps)	Fe (cps)
60	60	480.5			910.842	9009.74	410.579	51743.8	47904.1	64255.5	12823.9	329769
60.5	60.5	485.2										
61	61	489.9										
61.5	61.5	494.5										
62	62	499.3										
62.5	62.5	503.9										
63	63	508.5			960.95	9479.75	367	53220.8	48649.2	65472.3	13458.7	340765
63.5	63.5	513.2										
64	64	517.8										
64.5	64.5	522.3										
65	65	526.8										
65.5	65.5	531.4										
66	66	536.1			958.85	9516.4	411.5	50152.2	47728.3	63256.1	13001.7	333675
66.5	66.5	540.7										
67	67	545.4										
67.5	67.5	550										
68	68	554.7										
68.5	68.5	559.2										
69	69	563.7			957.1	9327.4	398.65	50012.6	47400.3	62650.7	12218.5	336742
69.5	69.5	568.1										
70	70	572.3										
70.5	70.5	577										
71	71	581.6										
71.5	71.5	586.2										
72	72	590.8			933.421	9229.74	749.737	51847	48130.1	64740.1	12845.7	350815
72.5	72.5	595.3										
73	73	599.9										
73.5	73.5	604.7										
74	74	609.2										
74.5	74.5	613.8										

Table S2. Raw magnetic susceptibility (MS), density, and X-ray fluorescence (XRF) data. (cont.)

Depth in core (cm)	Composite Depth in Core (cm)	Calibrated Age (cal yr BP)	MS (SI)	Density (g/cm^3)	Al (cps)	Si (cps)	S (cps)	K (cps)	Ca (cps)	Ti (cps)	Mn (cps)	Fe (cps)
75	75	618.5			972.25	9475.5	584.2	53704.3	46160.4	65017.2	12653.2	338554
75.5	75.5	622.7										
76	76	627.1										
76.5	76.5	631.6										
77	77	636										
77.5	77.5	640.3										
78	78	644.8										
78.5	78.5	649.3										
79	79	653.7										
79.5	79.5	658										
80	80	662.3										
80.5	80.5	666.9										
81	81	671.3										
81.5	81.5	675.9										
82	82	680.5										
82.5	82.5	685										
83	83	689.5										
83.5	83.5	694										
84	84	698.4										
84.5	84.5	703										
85	85	707.4										
85.5	85.5	711.8										
86	86	716.2										
86.5	86.5	720.8										
87	87	725.2										
87.5	87.5	729.6										
88	88	734.1										
88.5	88.5	738.5										
89	89	742.9										
89.5	89.5	747.3										
90	90	751.6										

Table S2. Raw magnetic susceptibility (MS), density, and X-ray fluorescence (XRF) data. (cont.)

Depth in core (cm)	Composite Depth in Core (cm)	Calibrated Age (cal yr BP)	MS (SI)	Density (g/cm^3)	Al (cps)	Si (cps)	S (cps)	K (cps)	Ca (cps)	Ti (cps)	Mn (cps)	Fe (cps)
90.5	90.5	756.3										
91	91	760.9										
91.5	91.5	765.6										
92	92	770.3										
92.5	92.5	775										
93	93	779.7										
93.5	93.5	784.2										
94	94	789.1										
94.5	94.5	793.6										
95	95	798.2										
95.5	95.5	803										
96	96	807.7										
96.5	96.5	812.4										
97	97	817.2										
97.5	97.5	821.9										
98	98	826.7										
98.5	98.5	831.3										
99	99	836.1										
99.5	99.5	840.9										
0	100	845.5			333	4602	221	40592	51617	64525	8363	356890
0.5	100.5	850.1			359	5340	305	45840	56233	71644	9222	397982
1	101	854.8		1.3742	398	5632	361	48421	57658	73359	10757	413292
1.5	101.5	859.7			403	5918	417	47403	58237	73411	11192	414964
2	102	864.4	42.472	1.3317	429	5769	464	46843	57468	72236	13323	412829
2.5	102.5	869.3			423	5648	397	48447	61313	73724	10589	427435
3	103	874	47.223	1.289	428	5507	262	48233	58206	72620	10031	419395
3.5	103.5	878.8			380	5719	269	47184	57228	71938	13295	410840
4	104	883.4	48.133	1.2761	346	5714	369	47196	56450	72835	12876	410596
4.5	104.5	888.3			412	5735	398	47343	55588	71469	13180	405349
5	105	893	47.864	1.2698	344	5625	443	48688	55204	72380	11452	417573

Table S2. Raw magnetic susceptibility (MS), density, and X-ray fluorescence (XRF) data. (cont.)

Depth in core (cm)	Composite Depth in Core (cm)	Calibrated Age (cal yr BP)	MS (SI)	Density (g/cm^3)	Al (cps)	Si (cps)	S (cps)	K (cps)	Ca (cps)	Ti (cps)	Mn (cps)	Fe (cps)
5.5	105.5	897.5			457	5709	460	47247	54956	70537	12968	405626
6	106	902.1	47.165	1.2634	414	6014	406	49774	57032	73880	12130	415523
6.5	106.5	906.6			351	5907	375	48622	56324	71646	13152	413280
7	107	911	46.852	1.2581	435	5490	406	47101	55026	70774	12607	412641
7.5	107.5	915.6			431	5971	523	50102	54079	73245	11276	413004
8	108	920.1	47.086	1.2538	452	5721	486	49530	53885	73816	11733	411123
8.5	108.5	924.8			419	5699	451	49354	55831	72588	12509	414745
9	109	929.3	47.437	1.2638	431	5757	526	50330	54437	73857	11367	414378
9.5	109.5	933.8			439	5922	493	50577	53177	73989	11826	417158
10	110	938.3	49.295	1.2478	401	5844	355	49628	56038	73533	11626	416093
10.5	110.5	943.1			433	5999	335	49596	61303	76521	11198	423881
11	111	947.7	50.213	1.2579	412	5933	302	49370	61185	75549	12170	420322
11.5	111.5	952.6			426	6289	414	51929	64364	78293	11939	438932
12	112	957.2	52.177	1.2316	512	6325	519	51125	61550	77772	11836	433112
12.5	112.5	962			430	5863	428	49015	59976	74263	12421	421589
13	113	966.7	51.253	1.2574	374	5709	457	49329	59914	74962	12726	434132
13.5	113.5	971.5			420	5905	513	50329	55710	75699	12808	420414
14	114	976.1	51.789	1.2338	443	5871	495	49371	58497	74638	11782	422898
14.5	114.5	980.8			321	5707	467	47673	58926	74225	13293	416365
15	115	985.5	50.235	1.2409	365	5706	411	48507	61633	74796	13177	425865
15.5	115.5	989.7			453	5865	435	49294	58606	74567	13641	421780
16	116	994.1	51.135	1.228	466	5676	477	48242	56969	73373	12145	413728
16.5	116.5	998.3			458	5619	455	48257	59317	73886	13132	418535
17	117	1002.6	50.844	1.2206	448	5587	339	46871	55215	71882	14217	407583
17.5	117.5	1006.9			445	5915	474	49385	55504	73140	11251	417458
18	118	1011.3	49.15	1.2459	409	5708	490	50542	55493	75417	11108	427791
18.5	118.5	1015.8			395	5953	483	52535	57289	77092	12147	438306
19	119	1020.4	49.313	1.2307	374	5764	484	50335	54190	74149	11092	422190
19.5	119.5	1024.8			404	5601	466	49209	52997	72447	13129	425300
20	120	1029.1	48.84	1.2407	401	5424	430	47504	52053	70871	12794	429647

Table S2. Raw magnetic susceptibility (MS), density, and X-ray fluorescence (XRF) data. (cont.)

Depth in core (cm)	Composite Depth in Core (cm)	Calibrated Age (cal yr BP)	MS (SI)	Density (g/cm^3)	Al (cps)	Si (cps)	S (cps)	K (cps)	Ca (cps)	Ti (cps)	Mn (cps)	Fe (cps)
20.5	120.5	1033.9			435	5259	416	49284	55237	73844	12402	443855
21	121	1038.6	49.329	1.2414	466	5299	478	46741	53252	71080	11217	428636
21.5	121.5	1043.2			366	5430	476	48348	59694	73507	12779	435453
22	122	1047.9	50.029	1.2478	453	5690	417	48317	54855	72960	11539	432103
22.5	122.5	1052.7			440	5718	428	47684	55466	72756	12111	428121
23	123	1057.5	51.938	1.2338	366	5543	371	48248	55608	74188	11339	436221
23.5	123.5	1062.2			438	5533	380	49506	55562	75766	10340	442235
24	124	1066.9	53.554	1.2359	457	5660	450	49211	55844	75574	13015	451086
24.5	124.5	1071.4			429	5921	565	51030	57627	78235	10754	448858
25	125	1076.2	55.129	1.2521	446	5910	517	52686	58914	79635	13070	448740
25.5	125.5	1080.5			477	5565	344	51713	57170	78250	13090	446100
26	126	1084.8	58.404	1.2369	417	5637	371	50684	57369	77319	13988	449333
26.5	126.5	1089.2			408	5454	286	49815	56324	75888	13081	444599
27	127	1093.6	59.76	1.2579	357	5101	322	49091	55854	75961	12813	447204
27.5	127.5	1098			400	5260	364	49400	57990	76272	12672	450201
28	128	1102.5	61.666	1.2636	421	5368	286	50021	59637	77873	13088	459697
28.5	128.5	1106.9			454	5495	350	51153	60910	79569	12481	463489
29	129	1111.3	63.951	1.2586	402	5592	253	51773	60647	81042	13342	458311
29.5	129.5	1115.9			390	5831	367	51294	63071	80164	13361	462018
30	130	1120.3	65.155	1.2804	420	5513	204	53107	60245	80799	12843	459717
30.5	130.5	1124.9			475	5946	399	56855	61057	85828	14537	468184
31	131	1129.6	65.915	1.3031	514	6033	305	57202	60349	87420	11950	472274
31.5	131.5	1134.3			538	5731	284	59275	54515	90442	12325	460876
32	132	1139.1	64.428	1.3361	473	5887	208	62226	54820	92013	11674	460814
32.5	132.5	1143.5			463	5331	291	58515	53539	90287	11351	446484
33	133	1148.4	62.817	1.3397	466	5696	255	62239	52364	95450	13233	437022
33.5	133.5	1153.1			494	5825	118	63291	51225	96029	12663	427169
34	134	1157.8	60.756	1.3414	506	5893	83	61987	53290	93144	14430	449068
34.5	134.5	1162.5			486	5950	170	58377	54672	88155	12698	457639
35	135	1167	61.201	1.3151	495	5761	196	59810	54594	89619	11375	451419

Table S2. Raw magnetic susceptibility (MS), density, and X-ray fluorescence (XRF) data. (cont.)

Depth in core (cm)	Composite Depth in Core (cm)	Calibrated Age (cal yr BP)	MS (SI)	Density (g/cm^3)	Al (cps)	Si (cps)	S (cps)	K (cps)	Ca (cps)	Ti (cps)	Mn (cps)	Fe (cps)
35.5	135.5	1171.7			488	5880	282	65394	52298	96390	11325	446594
36	136	1176.4	62.17	1.3094	584	6392	416	69792	51045	100667	11354	435180
36.5	136.5	1181.1			569	6857	907	73662	54511	104028	10733	446688
37	137	1185.8	62.273	1.3308	554	6198	679	68311	51247	98780	10181	433116
37.5	137.5	1190.5			552	6194	269	69546	51106	99625	10341	432530
38	138	1195.3	69.328	1.2125	567	6476	209	70913	52447	99549	10410	440334
38.5	138.5	1200.1			625	6655	87	71074	54426	100444	13027	445447
39	139	1204.7	62.656	1.3592	516	6304	75	66878	53400	97218	10834	442266
39.5	139.5	1209.6			528	5609	95	64750	51491	94772	12163	437220
40	140	1214.2	61.812	1.3911	472	5272	102	62476	49859	91227	13522	428189
40.5	140.5	1218.6			437	5403	344	62485	49248	91491	13214	411351
41	141	1223.1	65.609	1.312	455	5579	781	63307	48994	90470	12109	431815
41.5	141.5	1227.6			523	5776	353	63954	48418	90153	13294	473158
42	142	1232.1	63.739	1.3476	442	5035	677	59081	47414	84385	14030	474488
42.5	142.5	1236.8			505	6278	1009	67322	52933	95140	13594	461176
43	143	1241.4	64.587	1.337	502	6304	1366	69721	52352	97296	11979	439533
43.5	143.5	1246			515	6364	942	69038	55181	98112	12703	454942
44	144	1250.5	63.641	1.3756	543	6125	632	69531	53924	97848	11651	454450
44.5	144.5	1255			503	6354	620	70478	52858	97375	9836	444593
45	145	1259.6	65.278	1.365	501	6305	349	71240	53021	97113	12037	441178
45.5	145.5	1264.2			591	6363	298	71003	57288	98964	13548	447893
46	146	1268.8	65.465	1.3807	555	6656	225	73195	57123	101227	12364	452533
46.5	146.5	1273.5			548	6569	434	72597	56191	101884	11156	453956
47	147	1278	66.564	1.3703	492	6352	371	71821	55826	99934	11691	450661
47.5	147.5	1282.6			536	6038	388	68566	54378	98736	12234	445622
48	148	1287.3	67.563	1.3609	613	6242	317	68791	54084	97529	13892	450718
48.5	148.5	1291.8			668	6383	496	70149	56012	98812	13440	454086
49	149	1296.5	67.493	1.3691	521	6332	224	69376	55909	98645	11499	446985
49.5	149.5	1301			520	6208	214	69302	55175	98494	11188	446186
50	150	1305.6	68.461	1.3551	533	5855	148	67881	50968	93819	11687	446256

Table S2. Raw magnetic susceptibility (MS), density, and X-ray fluorescence (XRF) data. (cont.)

Depth in core (cm)	Composite Depth in Core (cm)	Calibrated Age (cal yr BP)	MS (SI)	Density (g/cm^3)	Al (cps)	Si (cps)	S (cps)	K (cps)	Ca (cps)	Ti (cps)	Mn (cps)	Fe (cps)
50.5	150.5	1310.3			501	6005	198	67843	50925	93921	12032	427615
51	151	1315.2	68.469	1.359	556	6045	397	68288	52991	96413	11946	440384
51.5	151.5	1320			578	6141	266	69620	55355	98951	12452	440308
52	152	1324.7	67.899	1.3744	483	6096	175	68352	57408	98748	18075	439231
52.5	152.5	1329.5			574	6009	153	67622	55517	96509	16252	429833
53	153	1334.3	68.095	1.3785	546	6077	279	69667	55033	98811	11834	435852
53.5	153.5	1339.2			366	3790	284	48144	42550	70380	13286	337334
54	154	1343.9	68.65	1.3727	428	4617	241	55891	49997	85238	10498	398192
54.5	154.5	1348.7			436	5041	200	59140	51593	88968	11253	411232
55	155	1353.5	69.21	1.3616	520	5372	288	63238	53213	93181	12454	431687
55.5	155.5	1359.4			526	5656	147	67358	55201	97914	11603	441083
56	156	1365.4	67.908	1.3783	439	5748	224	66415	54868	97281	11440	430852
56.5	156.5	1371.2			550	5818	319	65313	56393	98044	11312	446379
57	157	1377.1	67.797	1.3684	507	5925	207	64723	56698	96960	12996	442662
57.5	157.5	1383			457	5787	262	65845	55436	96027	11778	452324
58	158	1388.9	67.857	1.3537	451	5799	163	64773	55793	96753	11555	447817
58.5	158.5	1394.8			497	6176	327	67084	56951	99627	11661	449976
59	159	1400.7	67.966	1.3447	577	6362	555	69604	57972	100689	12633	463166
59.5	159.5	1406.5			459	6305	509	67543	56090	98520	9885	449233
60	160	1412.4	68.277	1.3373	598	6170	354	66965	56021	97368	11462	452543
60.5	160.5	1417.9			557	6487	326	68631	57684	99884	11664	453165
61	161	1423.5	68.08	1.3479	504	6002	270	67356	57412	97244	10916	451825
61.5	161.5	1429.3			444	5748	315	65329	53897	94638	12032	436136
62	162	1435.2	67.977	1.3648	484	5845	612	68712	55073	98434	11681	455788
62.5	162.5	1441			509	5841	1063	68742	54321	99302	12056	454829
63	163	1446.8	68.819	1.364	510	5871	499	67926	57444	99001	11234	454211
63.5	163.5	1452.5			535	6180	281	66056	60972	97132	11141	473122
64	164	1458.3	70.488	1.3513	506	6107	237	69375	58912	100402	11175	460727
64.5	164.5	1464			483	6354	205	69675	62129	101228	11307	471068
65	165	1469.9	71.188	1.3727	487	6279	237	67914	60964	98590	11800	467462

Table S2. Raw magnetic susceptibility (MS), density, and X-ray fluorescence (XRF) data. (cont.)

Depth in core (cm)	Composite Depth in Core (cm)	Calibrated Age (cal yr BP)	MS (SI)	Density (g/cm^3)	Al (cps)	Si (cps)	S (cps)	K (cps)	Ca (cps)	Ti (cps)	Mn (cps)	Fe (cps)
65.5	165.5	1475.6			534	5973	114	66736	61446	98525	11588	473857
66	166	1481.4	74.391	1.3703	482	6509	308	68833	64313	101053	11250	471625
66.5	166.5	1487.1			596	6408	419	67677	64799	101587	12051	466705
67	167	1492.8	79.555	1.3551	532	6899	340	70194	66713	104254	11878	472001
67.5	167.5	1498.5			536	6939	787	69618	70202	102390	10805	482319
68	168	1504.2	83.057	1.3863	605	6517	272	68392	71265	102022	11566	474219
68.5	168.5	1509.9			515	6775	189	67318	72981	102132	11502	471294
69	169	1515.6	89.321	1.3732	566	6596	235	67672	74005	104713	11801	468887
69.5	169.5	1521.3			553	6735	200	67501	72738	103413	12573	466715
70	170	1526.9	94.479	1.3807	573	6963	420	65177	81019	101810	13200	507863
70.5	170.5	1532.5			475	5769	311	53557	81745	88744	14118	526631
71	171	1538.3	98.519	1.4023	412	4761	183	53588	60146	82859	10794	439576
71.5	171.5	1544.2			376	4962	318	53066	54792	81675	9949	370176
72	172	1550	104.29	1.4047	467	6256	767	57933	81900	95127	11599	484079
72.5	172.5	1555.8			500	6627	927	56093	89164	94532	11689	515233
73	173	1561.6	107.89	1.4241	563	6446	500	57778	88359	96829	10809	505122
73.5	173.5	1567.3			510	6733	347	57840	87219	96061	11441	502662
74	174	1573.2	114.17	1.3747	504	6310	230	59388	79853	95435	12166	492213
74.5	174.5	1578.9			467	5933	211	57652	77351	93588	11292	493375
75	175	1584.7	113.12	1.3834	473	5793	115	59456	72414	94608	12875	481919
75.5	175.5	1590.5			476	6027	209	61233	72628	95054	11877	472338
76	176	1596.3	119.06	1.2943	496	6381	183	60611	74433	96422	10620	471516
76.5	176.5	1602			490	6020	151	60921	74840	97642	12884	469295
77	177	1607.9	118.89	1.2746	508	6066	118	60839	74540	97793	12750	475464
77.5	177.5	1613.7			508	6433	311	61639	75781	99809	11616	478604
78	178	1619.5	124.41	1.2099	548	6464	648	61617	74529	99228	11747	480683
78.5	178.5	1625.2			419	5632	777	55169	68319	90936	11543	472679
79	179	1631.2	114.82	1.3269	429	5350	511	56372	69984	92381	10375	484076
79.5	179.5	1636.9			405	5396	408	54370	69122	90006	11021	483155
80	180	1642.4	115.77	1.3469	438	5069	209	52098	64833	86866	11220	472465

Table S2. Raw magnetic susceptibility (MS), density, and X-ray fluorescence (XRF) data. (cont.)

Depth in core (cm)	Composite Depth in Core (cm)	Calibrated Age (cal yr BP)	MS (SI)	Density (g/cm^3)	Al (cps)	Si (cps)	S (cps)	K (cps)	Ca (cps)	Ti (cps)	Mn (cps)	Fe (cps)
80.5	180.5	1648.2			475	5532	352	59196	64546	92221	11031	455551
81	181	1653.9	115.38	1.3841	466	5860	1136	56951	69086	92628	11377	473693
81.5	181.5	1659.6			472	5897	665	58732	69993	94534	11865	475324
82	182	1665.3	114.24	1.4139	521	6061	696	62392	65421	95378	10569	466828
82.5	182.5	1670.9			435	5702	416	62638	64679	95190	11974	459103
83	183	1676.6			486	6017	476	62567	67273	96660	11702	462568
83.5	183.5	1682.3			423	6036	492	63052	67410	97650	12347	462915
84	184	1687.8	112.38	1.4095	500	6194	384	63099	67532	96508	12199	458510
84.5	184.5	1693.5			486	6268	347	64419	68481	97575	10554	458297
85	185	1699.1	112.9	1.3723	469	6141	300	61878	69424	95984	11973	459654
85.5	185.5	1705			507	6201	262	62140	68992	97086	10932	458536
86	186	1710.6	110.05	1.3703	472	5930	273	63151	68079	98132	11497	464636
86.5	186.5	1716.5			484	6173	216	64380	66496	97713	10640	448379
87	187	1722.3	107.1	1.3669	515	6149	177	64538	67936	96542	11229	447041
87.5	187.5	1728			438	6012	273	61308	69283	95250	12641	449554
88	188	1733.9	105.83	1.3496	442	6358	280	61944	68367	96743	10141	451648
88.5	188.5	1739.7			497	6214	438	62324	65797	95083	10801	457004
89	189	1745.3	102.69	1.3694	474	6268	353	62345	64934	95264	11436	458120
89.5	189.5	1751.1			458	6202	353	63020	67253	96813	11490	457660
90	190	1756.7	102.15	1.365	479	6172	214	61351	66017	93571	10841	461640
90.5	190.5	1762.7			484	5876	158	61147	65429	93209	11258	458159
91	191	1768.7	99.746	1.3841	480	5746	161	60182	69880	97033	11778	471156
91.5	191.5	1774.6			497	6070	299	64437	69112	100081	11869	464313
92	192	1780.6	96.734	1.4044	438	6221	401	64101	67541	99855	12218	462006
92.5	192.5	1786.5			447	6250	446	64042	68238	99735	11714	471990
93	193	1792.5	95.935	1.3865	515	6394	551	64117	69290	100344	12657	467536
93.5	193.5	1798.4			494	6430	358	64026	69355	97613	11536	464774
94	194	1804.4	93.358	1.3885	535	6475	247	63817	64414	94074	11100	459451
94.5	194.5	1810.2			469	6092	203	63576	63240	94655	11712	458845
95	195	1816.2	90.189	1.3986	512	6586	205	65955	63365	95717	12546	451738

Table S2. Raw magnetic susceptibility (MS), density, and X-ray fluorescence (XRF) data. (cont.)

Depth in core (cm)	Composite Depth in Core (cm)	Calibrated Age (cal yr BP)	MS (SI)	Density (g/cm^3)	Al (cps)	Si (cps)	S (cps)	K (cps)	Ca (cps)	Ti (cps)	Mn (cps)	Fe (cps)
95.5	195.5	1822			449	6195	140	65453	61759	93619	11440	446852
96	196	1827.5	87.662	1.4013	484	5673	95	61796	62130	92490	12172	448128
96.5	196.5	1833.3			469	5318	84	59448	61700	89243	10538	449588
97	197	1838.9	85.436	1.396	491	5603	116	58845	60428	89117	10783	438340
97.5	197.5	1844.8			440	5188	145	58175	58586	88005	11375	431093
98	198	1850.4	77.32	1.4631	316	4213	122	48381	49366	75123	10376	378997
98.5	198.5	1856.3			397	5085	247	57930	55399	86759	12013	425159
99	199	1861.9	70.384	1.4535	384	3975	125	47321	45030	72083	10190	352070
0	200	1873.4			505	5531	316	73033	40348	95790	7110	383042
0.5	200.5	1879.4			542	6766	522	82420	46840	103937	9626	434581
1	201	1884.9	56.925	1.4526	588	6714	1151	83786	47731	104742	9964	458406
1.5	201.5	1891			478	6740	795	82022	50347	107095	10099	460590
2	202	1896.7	57.439	1.4124	516	5535	643	69920	46469	98090	9253	431489
2.5	202.5	1902.7			527	6510	340	74872	50190	103876	9694	451431
3	203	1908.5	57.97	1.371	497	6390	242	74818	49140	100790	9685	443524
3.5	203.5	1914.2			559	6223	543	73903	47665	100863	9095	437004
4	204	1920.2	56.136	1.357	539	6308	1045	74514	48729	100523	8832	443533
4.5	204.5	1926			464	6069	911	71854	48147	97296	10250	447507
5	205	1931.8	53.857	1.3515	551	6035	361	70908	47821	96351	9359	440113
5.5	205.5	1937.6			491	6228	267	71072	47675	95013	10279	434767
6	206	1943.3	52.27	1.3399	478	6145	126	72014	48198	96626	8965	422606
6.5	206.5	1949.3			527	6502	163	73728	49193	99171	9396	422185
7	207	1955	50.483	1.3474	573	6791	307	73759	49318	96962	9742	427098
7.5	207.5	1960.8			576	6869	546	73067	50232	95887	10081	442159
8	208	1966.6	49.718	1.3313	501	6238	683	66916	50136	92364	9276	438942
8.5	208.5	1972.4			514	6205	584	66415	50995	92047	9648	435867
9	209	1978.3	49.766	1.3005	576	6555	564	70597	51952	95534	10474	443580
9.5	209.5	1984.2			503	6319	393	70174	50696	95942	9850	432229
10	210	1990.1	48.823	1.3106	555	6345	704	67988	51819	93634	10327	447585
10.5	210.5	1996.1			491	6148	312	67194	51209	92801	10302	436664

Table S2. Raw magnetic susceptibility (MS), density, and X-ray fluorescence (XRF) data. (cont.)

Depth in core (cm)	Composite Depth in Core (cm)	Calibrated Age (cal yr BP)	MS (SI)	Density (g/cm^3)	Al (cps)	Si (cps)	S (cps)	K (cps)	Ca (cps)	Ti (cps)	Mn (cps)	Fe (cps)
11	211	2001.8	48.749	1.3051	486	6105	380	67833	52268	93021	10166	436318
11.5	211.5	2007.7			514	6091	425	68141	51358	91999	10597	435796
12	212	2013.4	48.513	1.3039	563	6111	376	67530	51285	92091	9964	432912
12.5	212.5	2019.2			541	5991	319	66682	51504	93046	9119	432631
13	213	2025.1	48.688	1.2916	480	6116	315	66390	51930	92843	11174	429396
13.5	213.5	2031			440	6328	319	67657	52622	93808	11066	435080
14	214	2036.8	48.538	1.2899	481	6188	322	67882	51632	93455	10215	426833
14.5	214.5	2042.7			513	6342	335	67825	53403	93898	10970	434292
15	215	2048.6	49.187	1.2729	521	6293	256	66952	52275	92693	9296	430139
15.5	215.5	2054.4			487	5861	382	65085	51365	90303	9962	422525
16	216	2060.3	49.454	1.2679	479	5580	345	63530	50837	91163	10924	425795
16.5	216.5	2066.2			506	5852	372	64663	51225	90861	9966	425509
17	217	2072.1	49.05	1.284	472	5987	423	64970	52099	91114	8460	427043
17.5	217.5	2077.9			611	6061	355	66336	53008	92813	8840	431349
18	218	2083.8	49.398	1.2842	488	5911	375	65778	51395	91789	10353	427804
18.5	218.5	2089.7			464	6027	308	66469	51477	92420	10166	426193
19	219	2095.6	48.931	1.3077	558	6102	243	66614	53555	93655	9988	431244
19.5	219.5	2101.4			530	6470	203	66882	54667	94800	10041	435230
20	220	2107.4	49.997	1.2835	507	6175	382	66835	52345	94311	11044	440495
20.5	220.5	2112.8			506	6498	409	69065	54401	95794	11295	443066
21	221	2118.1	49.827	1.2842	476	5967	283	65227	51578	90844	10758	429185
21.5	221.5	2123.6			573	6328	330	66901	52765	92786	11234	433300
22	222	2128.9	50.233	1.272	528	6209	312	67195	52961	92419	11450	435289
22.5	222.5	2134.4			506	6055	277	65926	52318	92753	10983	428432
23	223	2139.8	50.614	1.2624	550	6117	341	65980	52270	91015	10100	430976
23.5	223.5	2145.2			543	5927	386	65766	51901	91074	10142	428090
24	224	2150.7	50.339	1.2729	491	6169	212	67182	54100	91765	9712	431309
24.5	224.5	2156			486	6154	248	67819	54103	93972	10673	441564
25	225	2161.6	50.544	1.2696	438	6013	215	66929	54189	92530	10095	438518
25.5	225.5	2167.1			483	6227	225	67444	55222	93682	10768	439896

Table S2. Raw magnetic susceptibility (MS), density, and X-ray fluorescence (XRF) data. (cont.)

Depth in core (cm)	Composite Depth in Core (cm)	Calibrated Age (cal yr BP)	MS (SI)	Density (g/cm^3)	Al (cps)	Si (cps)	S (cps)	K (cps)	Ca (cps)	Ti (cps)	Mn (cps)	Fe (cps)
26	226	2172.7	51.054	1.2569	532	6320	235	67658	55454	93615	11323	436413
26.5	226.5	2178.3			503	6350	214	68352	54660	94213	10641	438157
27	227	2183.6	51.244	1.254	514	6040	166	68681	54130	92904	9966	435344
27.5	227.5	2189.2			539	6349	209	68741	53255	92497	10635	431535
28	228	2194.6	52.289	1.2342	538	6557	277	69545	54628	95189	10689	433040
28.5	228.5	2200.2			545	6541	157	69431	54319	94271	9872	436562
29	229	2205.6	53.389	1.2226	498	6511	310	68754	54423	93573	11301	436268
29.5	229.5	2211.1			572	6250	321	69072	54841	93945	9909	437970
30	230	2216.7	52.343	1.2662	510	6291	286	68666	55853	95200	10339	440821
30.5	230.5	2222.8			481	6495	290	68288	55095	94078	9909	439847
31	231	2229	52.917	1.2698	606	6226	307	67990	56281	94318	10476	445325
31.5	231.5	2235.5			477	6401	343	70011	55953	95578	10207	450800
32	232	2241.8	53.204	1.2768	517	6551	306	70282	56767	95556	9961	451052
32.5	232.5	2248.4			535	6123	425	66574	53222	90089	10357	435764
33	233	2254.8	53.835	1.2703	499	5914	228	66996	53396	91382	9734	438899
33.5	233.5	2261.2			464	5973	213	66324	54428	91996	10410	440244
34	234	2267.7	53.953	1.2777	529	6276	445	69375	54610	94477	9300	436064
34.5	234.5	2274.1			451	6250	396	66280	55738	92718	10906	434278
35	235	2280.6	55.259	1.2674	537	6206	325	68233	55610	93094	10514	436460
35.5	235.5	2287.3			529	6402	539	68820	53528	92420	9556	439627
36	236	2294.2	57.966	1.2509	517	6428	439	68032	52167	90683	12035	424996
36.5	236.5	2301.2			494	6416	402	69572	54847	95503	11669	429281
37	237	2308	57.766	1.3108	578	6357	320	72046	56141	100089	11191	433476
37.5	237.5	2314.9			511	6576	141	73336	56369	102492	9893	432867
38	238	2321.8	58.146	1.3322	464	6279	128	71875	55086	100869	11138	430706
38.5	238.5	2328.7			462	6342	82	73292	56078	102721	11675	436367
39	239	2335.5	55.938	1.3766	512	6572	74	72271	56676	101828	10010	438444
39.5	239.5	2342.3			587	6608	76	73783	56899	102108	9155	439243
40	240	2349.1	54.782	1.3655	598	6790	72	75614	54906	101068	9468	444228
40.5	240.5	2356			577	6512	117	75435	52582	98279	10100	441972

Table S2. Raw magnetic susceptibility (MS), density, and X-ray fluorescence (XRF) data. (cont.)

Depth in core (cm)	Composite Depth in Core (cm)	Calibrated Age (cal yr BP)	MS (SI)	Density (g/cm^3)	Al (cps)	Si (cps)	S (cps)	K (cps)	Ca (cps)	Ti (cps)	Mn (cps)	Fe (cps)
41	241	2362.9	52.926	1.351	548	6410	97	75532	49620	97236	11069	425999
41.5	241.5	2369.7			552	6820	166	78307	50282	99320	9425	423636
42	242	2376.5	50.098	1.3486	570	7123	233	80500	53098	101987	9354	435203
42.5	242.5	2383.4			493	6699	333	77904	52028	99446	9245	434863
43	243	2390.3	47.772	1.3375	599	6698	405	76030	49146	95299	9684	422158
43.5	243.5	2397.1			546	6373	317	76395	51602	97040	9742	430736
44	244	2404	46.107	1.3202	480	6003	245	74288	50798	95924	10594	424123
44.5	244.5	2410.8			511	5816	320	75691	48703	95279	9026	414051
45	245	2417.7	44.321	1.3279	534	5942	264	76319	48212	93449	8934	412337
45.5	245.5	2424.4			472	5771	188	75495	48215	92183	9592	408920
46	246	2431	43.019	1.3382	441	5831	183	74610	48163	91594	9716	409072
46.5	246.5	2437.9			527	5996	243	76151	49547	94474	9683	417436
47	247	2444.7	42.655	1.3346	533	6265	287	77191	49665	94255	9782	424677
47.5	247.5	2451.5			515	6100	278	75310	49212	92982	11500	420201
48	248	2458.4	43.263	1.3031	534	6104	258	75140	47607	91802	9628	416842
48.5	248.5	2465.2			560	6393	199	75609	46160	90754	10495	406058
49	249	2472	42.334	1.3231	503	6015	269	76005	46011	90094	10375	404608
49.5	249.5	2478.8			492	6006	210	74360	44941	87965	9997	393728
50	250	2485.7	42.693	1.3034	507	6249	145	77021	46663	91517	11498	402386
50.5	250.5	2492.6			558	6179	121	75428	45531	89452	9934	401440
51	251	2499.9	42.435	1.3156	509	6052	181	74866	45064	86704	9859	397467
51.5	251.5	2507			531	6187	536	75757	47302	90815	11004	402747
52	252	2514.2	42.819	1.3231	558	6562	230	77078	49508	91959	10869	402067
52.5	252.5	2521.3			465	6513	188	76222	49948	93856	10101	408896
53	253	2528.6	43.437	1.3212	535	6418	151	76254	47709	92453	10454	409083
53.5	253.5	2535.6			576	6503	190	74939	47725	91108	10488	408048
54	254	2542.6	43.97	1.3135	550	6655	240	75033	48308	91398	10091	417120
54.5	254.5	2549.8			491	6358	158	71817	46421	88506	9351	398664
55	255	2556.8	43.884	1.3139	433	5046	198	60846	41208	75722	8848	346571
55.5	255.5	2563.2			441	5079	136	60436	43241	76948	8452	344764

Table S2. Raw magnetic susceptibility (MS), density, and X-ray fluorescence (XRF) data. (cont.)

Depth in core (cm)	Composite Depth in Core (cm)	Calibrated Age (cal yr BP)	MS (SI)	Density (g/cm^3)	Al (cps)	Si (cps)	S (cps)	K (cps)	Ca (cps)	Ti (cps)	Mn (cps)	Fe (cps)
56	256	2569.6	43.715	1.3127	441	5543	187	63978	43727	81698	9210	360716
56.5	256.5	2576.2			504	6044	158	70585	45485	86859	9259	384317
57	257	2582.8	43.543	1.3137	526	6490	269	72748	46199	89479	10697	403082
57.5	257.5	2589.1			522	6647	251	74870	47558	92317	10947	409732
58	258	2595.8	43.377	1.3188	531	6685	205	75648	49417	92832	9126	415045
58.5	258.5	2602.2			520	6514	307	73803	46975	91435	10187	411093
59	259	2608.6	43.143	1.3216	497	6353	265	72073	46502	89277	10627	408130
59.5	259.5	2615			551	6585	281	73069	47941	91374	9401	407088
60	260	2621.4	43.177	1.3163	559	6772	224	75006	48970	93122	10422	413380
60.5	260.5	2628.4			529	6450	284	73693	47991	90796	9157	413482
61	261	2635.4	43.752	1.2991	506	6215	229	73764	47966	90798	9985	418979
61.5	261.5	2642.3			459	6500	215	75900	48562	92740	12067	421210
62	262	2649.4	43.515	1.3103	595	6435	239	75739	47031	92768	9565	413511
62.5	262.5	2656.3			569	6583	222	77326	44792	90839	10945	411513
63	263	2663.2	43.577	1.319	631	6734	172	78905	45572	93145	10987	411341
63.5	263.5	2670.3			546	6464	225	75880	48387	92437	11054	416555
64	264	2677.2	43.714	1.3358	556	6321	310	74313	49297	91863	11372	421584
64.5	264.5	2684.2			532	6204	339	75414	47113	91601	11763	421120
65	265	2691.4	44.841	1.337	514	6241	233	76010	47519	91867	11592	412955
65.5	265.5	2698.1			565	6085	238	75811	48083	91642	9982	419111
66	266	2705	47.428	1.3298	477	6275	188	78031	47958	93267	9204	416832
66.5	266.5	2712.1			483	5698	257	71087	48583	90223	8833	382277
67	267	2719	50.503	1.3305	380	5399	348	68519	50484	90661	8986	386930
67.5	267.5	2725.7			516	5612	241	72156	54612	98463	9454	423466
68	268	2733	52.901	1.3361	485	5524	172	71808	55658	98673	9546	430203
68.5	268.5	2739.8			399	5251	155	71035	56418	98363	10329	431255
69	269	2746.7	53.787	1.3464	456	5338	138	70999	56868	98704	12140	436948
69.5	269.5	2753.7			358	5044	96	71905	57100	99661	10035	436595
70	270	2760.8	53.533	1.3443	418	5093	174	69934	56540	97581	11406	435435
70.5	270.5	2767.2			396	4777	171	68979	55020	95549	10901	433892

Table S2. Raw magnetic susceptibility (MS), density, and X-ray fluorescence (XRF) data. (cont.)

Depth in core (cm)	Composite Depth in Core (cm)	Calibrated Age (cal yr BP)	MS (SI)	Density (g/cm^3)	Al (cps)	Si (cps)	S (cps)	K (cps)	Ca (cps)	Ti (cps)	Mn (cps)	Fe (cps)
71	271	2773.8	52.802	1.3195	397	4788	121	69012	54292	92725	10843	426681
71.5	271.5	2780.3			439	4711	128	69109	51730	90307	10348	427676
72	272	2786.9	49.548	1.3469	474	4832	169	69968	53088	91643	10263	423883
72.5	272.5	2793.3			435	5075	194	70152	54575	94761	10043	428326
73	273	2799.7	47.43	1.3549	403	5102	245	70130	55574	94826	11245	428958
73.5	273.5	2806.5			437	5026	303	69929	54553	92353	10595	424000
74	274	2812.9	47.333	1.3286	489	5276	232	70810	52801	90064	11179	423589
74.5	274.5	2819.3			455	5377	314	67287	50927	86523	11522	412478
75	275	2825.8	48.133	1.3084	537	5890	271	69932	51542	90022	10330	420669
75.5	275.5	2832.5			491	6122	309	70760	52058	93306	10723	427225
76	276	2839.2	48.819	1.3257	493	6394	417	71883	53437	93945	12657	433712
76.5	276.5	2845.8			569	6433	315	71714	52946	93465	10501	430909
77	277	2852.5	51.075	1.3156	525	6652	314	72898	53997	95904	11908	438006
77.5	277.5	2859.1			614	6936	200	72750	56023	97792	10962	444331
78	278	2865.7	51.363	1.3368	591	7482	162	73359	56840	98136	10191	446390
78.5	278.5	2872.4			652	7182	112	72892	54681	94550	12330	441674
79	279	2879	52.114	1.307	646	7236	151	74275	53635	96671	10609	442602
79.5	279.5	2885.5			645	6945	197	73938	52375	95870	11282	441529
80	280	2892.3	49.544	1.3322	646	6906	393	73775	49722	93428	10958	430199
80.5	280.5	2898.6			540	7134	634	73524	48709	91204	10777	427130
81	281	2905.3	47.773	1.3298	598	6759	309	70567	50042	89971	10202	427795
81.5	281.5	2911.8			578	6758	413	73830	48195	90916	10940	425241
82	282	2918.5	45.978	1.3498	537	6761	227	73049	49580	93952	10976	427012
82.5	282.5	2925			539	6819	241	72202	49799	91048	10947	434396
83	283	2931.6	46.426	1.3269	505	6727	412	71080	50957	92071	10993	429145
83.5	283.5	2938.4			506	6354	207	69893	50694	90192	9468	433195
84	284	2944.8	46.575	1.3188	463	6504	222	70064	50072	89711	10416	432480
84.5	284.5	2951.3			451	6353	264	69559	50763	89566	10412	428916
85	285	2957.9	45.77	1.3339	570	6104	286	69136	49481	89907	8670	425963
85.5	285.5	2964.8			466	6121	425	69697	50126	89321	11261	424756

Table S2. Raw magnetic susceptibility (MS), density, and X-ray fluorescence (XRF) data. (cont.)

Depth in core (cm)	Composite Depth in Core (cm)	Calibrated Age (cal yr BP)	MS (SI)	Density (g/cm^3)	Al (cps)	Si (cps)	S (cps)	K (cps)	Ca (cps)	Ti (cps)	Mn (cps)	Fe (cps)
86	286	2971.3	45.213	1.3341	477	6339	769	69021	49944	88858	9993	432016
86.5	286.5	2978.1			496	6078	315	68652	48864	87605	10946	426264
87	287	2984.8	44.857	1.3325	485	6320	318	69875	50177	88785	10472	436331
87.5	287.5	2991.5			562	6324	240	70544	52268	90709	9677	447000
88	288	2998.2	45.033	1.3171	438	6269	208	67881	49884	89291	9242	434784
88.5	288.5	3005.2			558	6663	199	68932	49061	89608	9922	428104
89	289	3011.7	45.037	1.3149	504	6526	268	69776	48549	89096	10197	427076
89.5	289.5	3018.7			477	6570	315	70625	48846	90290	11207	433383
90	290	3025.2	45.72	1.2993	546	6163	264	68728	47844	88958	11407	425843
90.5	290.5	3031.7			499	6470	367	68205	48743	88920	9737	429899
91	291	3038.2	46.091	1.3067	445	6188	430	68844	48523	89602	11111	434558
91.5	291.5	3044.8			519	6248	616	68599	48793	89967	10162	436963
92	292	3051.2	46.941	1.3065	496	6615	501	69704	49418	91084	11058	440928
92.5	292.5	3057.9			556	6653	251	69798	49757	90455	10700	434202
93	293	3064.3	47.124	1.3248	493	6539	225	69293	48889	89728	10022	429522
93.5	293.5	3070.8			502	6750	221	69160	49347	90941	10371	433439
94	294	3077.2	47.233	1.3411	554	6776	286	69934	50900	91261	9749	435915
94.5	294.5	3083.9			547	6878	319	70604	51266	91061	11729	438957
95	295	3090.4	49.948	1.2811	566	6799	397	70191	50413	92330	11352	436691
95.5	295.5	3097.1			493	6502	573	69601	50821	91424	10503	430597
96	296	3104	49.402	1.3027	513	6270	415	69626	49001	90657	10842	435981
96.5	296.5	3110.6			448	6367	354	70796	48834	92669	9587	435001
97	297	3117.2	49.852	1.2909	483	6707	285	71013	50557	93025	13543	444424
97.5	297.5	3124.1			568	6600	330	70083	51141	92902	9137	447595
98	298	3131	46.898	1.3566	530	6317	414	68240	49002	89453	10132	436612
98.5	298.5	3137.8			481	5861	509	64039	47196	85131	10067	423960
99	299	3144.4	45.011	1.3686	485	5647	439	61791	46676	83215	11061	415942
99.5	299.5	3151.3			463	4806	409	57140	43393	78502	9054	389178
0	300	3158.1			434	5228	291	56399	46043	78927	6522	394336
0.5	300.5	3165.4			365	5546	376	60124	55768	84495	9272	449206

Table S2. Raw magnetic susceptibility (MS), density, and X-ray fluorescence (XRF) data. (cont.)

Depth in core (cm)	Composite Depth in Core (cm)	Calibrated Age (cal yr BP)	MS (SI)	Density (g/cm^3)	Al (cps)	Si (cps)	S (cps)	K (cps)	Ca (cps)	Ti (cps)	Mn (cps)	Fe (cps)
1	301	3172.4	77.77		485	5620	330	63902	50565	90541	9794	436647
1.5	301.5	3179.7			542	6260	284	69051	50325	92886	10655	438509
2	302	3186.8	51.918	1.3455	391	6258	296	63029	53431	89512	11926	438853
2.5	302.5	3194.1			446	5941	384	57549	54264	83699	11975	440213
3	303	3201.3	56.353	1.3209	425	5715	357	58563	54127	85839	11445	446229
3.5	303.5	3208.6			495	5621	267	64274	48803	90569	9859	441500
4	304	3215.8	57.821	1.3207	519	6063	249	69161	47758	94585	9822	441282
4.5	304.5	3222.9			572	6385	354	73041	47235	97936	10799	439890
5	305	3230.1	59.031	1.3091	532	6733	344	74760	50388	100543	12165	458647
5.5	305.5	3237.6			537	6058	209	69297	47414	96254	10479	440317
6	306	3244.9	58.574	1.3334	524	6332	161	68033	48132	94559	9205	445192
6.5	306.5	3252.2			539	6573	133	71553	49511	97666	10076	442606
7	307	3259.5	57.53	1.3752	517	6520	213	72209	50097	99110	10945	449198
7.5	307.5	3266.9			555	6626	295	73211	53266	101749	11227	455467
8	308	3274.2	58.34	1.3843	591	6480	251	74143	48844	101094	11414	449223
8.5	308.5	3281.5			529	6654	404	74336	51411	103247	10990	453826
9	309	3288.9	60.472	1.3628	562	6735	315	75312	51544	105035	10102	457674
9.5	309.5	3296.4			548	6588	305	74632	49334	103353	11393	447548
10	310	3303.7	61.427	1.373	544	6771	318	76440	50840	105901	10414	453793
10.5	310.5	3311.4			566	6755	283	79406	49976	110548	10551	452104
11	311	3319.3	61.464	1.4035	602	6921	481	79526	49818	111190	11072	452747
11.5	311.5	3327			582	6953	567	80043	50881	111313	11203	449728
12	312	3335	62.283	1.4086	542	6815	298	79034	50397	108973	10190	450104
12.5	312.5	3342.9			492	6968	309	78699	49742	107407	10688	453512
13	313	3350.7	61.637	1.4248	553	6840	328	76923	49050	104627	11474	446186
13.5	313.5	3358.4			527	6502	290	76518	49049	104909	10532	448788
14	314	3366.5	61.603	1.4122	530	6609	209	77576	50096	107416	10272	446625
14.5	314.5	3374.4			566	6715	248	77073	50283	107488	9495	444893
15	315	3382	61.962	1.3863	566	6412	226	75765	50174	104728	10847	441765
15.5	315.5	3390			587	6644	198	76005	48718	103952	9428	436543

Table S2. Raw magnetic susceptibility (MS), density, and X-ray fluorescence (XRF) data. (cont.)

Depth in core (cm)	Composite Depth in Core (cm)	Calibrated Age (cal yr BP)	MS (SI)	Density (g/cm^3)	Al (cps)	Si (cps)	S (cps)	K (cps)	Ca (cps)	Ti (cps)	Mn (cps)	Fe (cps)
16	316	3397.8	59.998	1.4103	618	6665	350	75563	48180	102405	10348	439608
16.5	316.5	3405.7			580	6483	179	75349	48908	100977	8727	442259
17	317	3413.9	60.573	1.3863	513	6307	265	71195	45993	95906	9474	421953
17.5	317.5	3421.8			568	6531	298	74546	46345	98636	10711	422850
18	318	3429.7	62.455	1.3607	481	6567	334	73151	46979	96262	10311	427043
18.5	318.5	3437.6			515	6728	355	72003	50092	98047	11699	439548
19	319	3445.5	64.792	1.3696	539	6548	323	71508	51224	99609	10566	442638
19.5	319.5	3453.4			540	6484	189	70312	52260	99719	10455	443797
20	320	3461.4	70.894	1.3474	496	6512	120	71799	54458	102648	10554	451601
20.5	320.5	3468.9			558	6849	215	72037	56759	105383	11979	448481
21	321	3476.8	74.119	1.4001	584	7212	125	73802	59904	108502	10505	461335
21.5	321.5	3484.5			509	6562	205	72039	57038	105990	11509	461224
22	322	3492	77.839	1.4239	528	6622	243	70171	57055	106562	11999	462806
22.5	322.5	3499.5			524	7033	146	71610	60700	109781	10834	468632
23	323	3507.5	80.529	1.4241	540	6759	79	71308	59905	107855	12075	467287
23.5	323.5	3514.9			507	6670	330	71869	57029	105869	11074	465571
24	324	3522.5	80.618	1.4384	537	6992	164	72925	59546	108981	10465	466037
24.5	324.5	3530.2			622	7197	120	74847	60413	112364	10977	469426
25	325	3537.9	81.597	1.4212	595	6968	86	74142	59542	110050	10375	471366
25.5	325.5	3545.2			549	7253	40	76073	61253	112574	9436	486176
26	326	3553	80.828	1.4336	526	6222	95	70300	54553	102626	10090	453520
26.5	326.5	3560.4			421	6014	118	67121	51152	96521	10192	434421
27	327	3567.9	80.221	1.4501	523	6128	91	68403	53586	101524	10222	433999
27.5	327.5	3575.5			509	6125	115	69339	53694	101638	9847	441047
28	328	3583.1	81.025	1.4516	460	6207	73	70317	55436	104496	9878	449277
28.5	328.5	3590.5			513	6671	136	72601	59022	109178	11013	458594
29	329	3598.2	81.945	1.4465	498	6664	234	72607	60256	110981	11456	464014
29.5	329.5	3605.5			565	6510	215	73335	60544	111521	11152	471282
30	330	3613.1	80.681	1.4589	610	6562	193	72506	59479	109538	12137	474923
30.5	330.5	3620.4			583	6576	275	73235	58058	108546	12497	472832

Table S2. Raw magnetic susceptibility (MS), density, and X-ray fluorescence (XRF) data. (cont.)

Depth in core (cm)	Composite Depth in Core (cm)	Calibrated Age (cal yr BP)	MS (SI)	Density (g/cm^3)	Al (cps)	Si (cps)	S (cps)	K (cps)	Ca (cps)	Ti (cps)	Mn (cps)	Fe (cps)
31	331	3627.9	80.545	1.4341	499	6628	275	72554	56975	105788	11556	470413
31.5	331.5	3635.4			513	6626	120	74622	58261	107806	10974	466435
32	332	3642.8	79.026	1.428	514	6551	199	71736	57923	104536	11839	461493
32.5	332.5	3650.4			543	6432	386	69241	57039	100968	11062	456215
33	333	3657.8	78.379	1.4175	604	6517	468	70039	57486	101232	12504	464804
33.5	333.5	3665.2			518	6391	459	68671	56745	99328	10967	452604
34	334	3672.9	78.847	1.3998	582	6334	539	68451	58564	100447	10495	460728
34.5	334.5	3680.3			497	6479	328	69836	57994	101461	10655	452304
35	335	3687.7	78.185	1.4035	654	6748	150	72465	55785	103887	12105	456779
35.5	335.5	3695			555	6492	277	69320	56427	102610	13043	453040
36	336	3702.4	78.141	1.3914	487	6236	251	69866	57046	103034	10639	457437
36.5	336.5	3710			562	6639	145	70920	55772	100727	10613	453956
37	337	3717.4	76.144	1.4134	554	6761	187	71209	55625	98231	11545	461560
37.5	337.5	3725			562	6774	287	70809	59474	103938	11335	475116
38	338	3732.4	76.551	1.4059	606	6498	189	68896	55660	97791	11528	457377
38.5	338.5	3740			598	6348	188	67862	55022	97136	10671	460312
39	339	3747.5	77.75	1.4066	524	6036	84	66246	53965	95498	12887	464629
39.5	339.5	3755			536	6220	149	68769	57011	101445	11928	473393
40	340	3762.3	80.086	1.4137	571	6237	247	67356	57360	98415	12658	461161
40.5	340.5	3770			509	6502	155	67345	58206	100455	12347	461125
41	341	3777.8	85.14	1.4008	503	6198	202	66725	58513	99354	11838	460786
41.5	341.5	3785.5			511	6247	146	66201	58015	97919	13114	464018
42	342	3793.2	90.233	1.4132	471	6654	263	67980	62419	101812	11529	472966
42.5	342.5	3800.9			558	6983	232	67205	65292	104094	11144	473667
43	343	3808.6	95.973	1.4146	618	6584	253	66964	64999	102819	11197	470075
43.5	343.5	3816.3			476	6434	101	65379	62766	101029	12389	461216
44	344	3824	101.06	1.4078	494	5960	128	61897	61319	96231	12031	455219
44.5	344.5	3831.9			346	3806	80	40624	41466	62520	10331	324891
45	345	3839.5	103.04	1.4253	269	2926	99	34668	36865	55947	8661	287249
45.5	345.5	3847			261	3066	43	34065	37815	56522	7340	272342

Table S2. Raw magnetic susceptibility (MS), density, and X-ray fluorescence (XRF) data. (cont.)

Depth in core (cm)	Composite Depth in Core (cm)	Calibrated Age (cal yr BP)	MS (SI)	Density (g/cm^3)	Al (cps)	Si (cps)	S (cps)	K (cps)	Ca (cps)	Ti (cps)	Mn (cps)	Fe (cps)
46	346	3854.6	105.96	1.4258	440	5283	270	53996	55296	86423	11587	398555
46.5	346.5	3862.2			469	6165	86	62516	63541	98690	11370	453787
47	347	3869.8	108.44	1.4304	419	6270	148	62595	67379	100526	13848	468240
47.5	347.5	3877.5			468	6327	497	62537	66010	99724	13881	469834
48	348	3885.1	112.1	1.418	522	6410	472	62816	67691	100956	14608	459420
48.5	348.5	3892.7			510	6459	509	64699	72563	104256	16308	471539
49	349	3900.3	113.11	1.437	420	6834	1002	65089	72506	104888	15098	476726
49.5	349.5	3907.7			508	6598	640	65114	71854	104140	16062	471374
50	350	3915.3	113.74	1.4523	437	6148	324	62213	63606	100303	15008	449479
50.5	350.5	3922.9			581	6529	124	64298	67097	105249	14727	458230
51	351	3930.7	117.77	1.4268	560	6143	362	61532	67493	103021	17042	457231
51.5	351.5	3938.7			504	6504	279	66269	70070	104527	20973	471542
52	352	3946.7	120.28	1.4336	526	6995	294	67287	74434	107996	21761	477273
52.5	352.5	3954.4			569	6497	255	65973	68802	105200	14452	466128
53	353	3962.2	123.75	1.4445	461	6335	270	64833	74582	104335	14559	479523
53.5	353.5	3970.1			509	6705	168	65442	80449	106992	14670	481295
54	354	3977.7	126.67	1.4633	467	6954	165	67215	83061	109006	15717	485335
54.5	354.5	3985.6			477	6056	159	61839	81594	102873	19870	482827
55	355	3993.2	132.19	1.4397	450	6560	458	64304	75557	104988	17126	483528
55.5	355.5	4000.7			451	6468	268	62624	82163	103745	15769	491489
56	356	4007.7	137.48	1.4103	560	6584	246	62931	86654	104239	15700	497569
56.5	356.5	4014.8			500	6451	151	61836	87403	103837	15420	481592
57	357	4022	142.31	1.3843	504	6623	187	63434	87784	106412	15804	487411
57.5	357.5	4029.5			497	6580	251	63330	88407	105986	15353	487738
58	358	4037.1	143.32	1.3918	457	6404	201	62704	86636	104273	13685	483380
58.5	358.5	4044.7			527	6591	437	63290	85904	104501	14067	487192
59	359	4052.5	143.15	1.4006	465	6641	559	64952	85855	106222	13754	482350
59.5	359.5	4060.1			469	6785	401	65047	79197	103963	15735	486885
60	360	4067.9	141.94	1.4066	524	7001	484	68198	79916	107991	15424	485647
60.5	360.5	4075.5			495	6392	343	63442	83774	106278	16014	477698

Table S2. Raw magnetic susceptibility (MS), density, and X-ray fluorescence (XRF) data. (cont.)

Depth in core (cm)	Composite Depth in Core (cm)	Calibrated Age (cal yr BP)	MS (SI)	Density (g/cm^3)	Al (cps)	Si (cps)	S (cps)	K (cps)	Ca (cps)	Ti (cps)	Mn (cps)	Fe (cps)
61	361	4083.2	139.87	1.4248	463	6762	478	64178	84073	105206	17162	480069
61.5	361.5	4090.9			528	6706	526	62577	83782	103311	16096	479586
62	362	4098.5	141.05	1.4234	505	6702	578	64020	133291	104226	18228	473577
62.5	362.5	4106.3			490	6677	987	64359	90269	105396	16910	482609
63	363	4113.9	140.74	1.4304	432	6558	1228	64426	89085	105024	16580	480864
63.5	363.5	4121.5			449	6224	1168	67999	75783	103535	15369	466214
64	364	4129.3	136.29	1.4535	431	6126	1300	74265	67417	106061	13755	462179
64.5	364.5	4136.9			446	6219	1649	73539	66579	106432	13051	463253
65	365	4144.9	132.72	1.4409	551	6409	1157	72304	71393	106485	14144	466941
65.5	365.5	4152.6			434	6504	1159	73360	82081	109177	13328	468189
66	366	4160.3	126.95	1.4392	492	6386	724	70389	79029	104901	14887	457164
66.5	366.5	4168.1			487	6309	1278	69128	84444	106442	16040	473655
67	367	4175.8	119.43	1.4645	476	6097	1446	70179	66417	104141	14201	487711
67.5	367.5	4183.4			512	6320	797	72722	64503	107823	14001	466235
68	368	4191.1	114.83	1.4657	495	6393	601	73361	64853	106943	12232	463590
68.5	368.5	4198.5			498	6114	661	71894	64790	105407	16316	466907
69	369	4206	114.67	1.435	482	6094	875	70378	67128	104996	15286	473396
69.5	369.5	4213.6			473	6317	786	72334	67023	106124	15427	465791
70	370	4221.2	113.84	1.4382	459	6509	717	73327	68088	109968	14900	470843
70.5	370.5	4228.6			444	6177	1019	70691	65551	106998	17448	471837
71	371	4236.1	112.29	1.4638	433	6445	896	72199	62587	107590	14256	475281
71.5	371.5	4243.7			504	6598	1326	71064	68446	106386	14531	485185
72	372	4251.5	112.25	1.4733	487	6628	1053	68253	81976	106560	16084	479306
72.5	372.5	4259.1			535	6729	1194	69904	78376	107378	14766	482990
73	373	4266.7	113.41	1.4526	596	6772	1093	73888	67743	109629	13889	481967
73.5	373.5	4274.3			489	6486	1027	72886	63388	105843	14852	467278
74	374	4281.6	110.87	1.4511	464	6440	920	70939	64580	105453	13447	463489
74.5	374.5	4289			484	6611	996	71302	66667	106746	15617	467831
75	375	4296.5	106.96	1.457	571	6718	864	72831	65291	107285	12564	469310
75.5	375.5	4304.1			524	6764	764	73036	63234	106733	12259	459840

Table S2. Raw magnetic susceptibility (MS), density, and X-ray fluorescence (XRF) data. (cont.)

Depth in core (cm)	Composite Depth in Core (cm)	Calibrated Age (cal yr BP)	MS (SI)	Density (g/cm^3)	Al (cps)	Si (cps)	S (cps)	K (cps)	Ca (cps)	Ti (cps)	Mn (cps)	Fe (cps)
76	376	4311.6	106.03	1.4499	471	6583	828	69735	68176	105484	13829	469385
76.5	376.5	4319.1			470	6330	902	68720	65302	106362	12923	476772
77	377	4326.7	107.37	1.4506	509	6511	981	67992	66973	107207	12769	486092
77.5	377.5	4334.3			427	6237	904	67720	66408	105719	14027	481998
78	378	4341.7	111.87	1.4406	456	5906	805	66738	65026	106175	14316	482908
78.5	378.5	4349.2			454	5833	669	68050	61776	105849	14889	485015
79	379	4356.8	116.17	1.4599	434	6261	826	65345	67806	104571	23873	498667
79.5	379.5	4364.3			457	6249	1053	61415	76715	100414	32451	500019
80	380	4371.9	125.12	1.4411	453	5760	1143	58816	73041	100383	18703	511528
80.5	380.5	4379.1			473	5972	956	59005	70674	100238	16040	521898
81	381	4386.7	132.95	1.4329	506	6467	955	59982	73051	99838	13236	524325
81.5	381.5	4394			486	5911	614	56039	71512	96311	13583	519465
82	382	4401.4	138.78	1.4175	368	5985	705	54933	71509	95996	15424	510719
82.5	382.5	4408.7			508	6293	769	56839	73359	97564	13403	510844
83	383	4416.2	139.89	1.4103	391	5943	922	57645	71645	96920	13262	510224
83.5	383.5	4423.6			471	6317	754	62632	71877	103853	13387	497259
84	384	4431	137.18	1.4074	457	6238	584	62161	71438	102247	14287	482425
84.5	384.5	4438.6			496	6285	669	63309	70643	103199	14257	485410
85	385	4446	132.34	1.411	405	6429	846	63307	68673	100201	12827	481909
85.5	385.5	4453.4			466	6104	913	62379	68242	100857	14134	477005
86	386	4460.4	125.7	1.4382	446	6105	740	61585	70036	101882	14022	479388
86.5	386.5	4467.8			424	6046	867	61100	70837	102664	14803	482245
87	387	4475	121.71	1.4492	454	6118	572	60220	71207	101915	13735	482267
87.5	387.5	4482.3			430	6343	838	58434	71756	98788	13248	495796
88	388	4489.9	121.48	1.4217	493	6572	1574	61295	74805	102232	12869	507943
88.5	388.5	4497			530	6260	1170	60939	71745	101041	13126	487389
89	389	4504.6	119.11	1.4161	440	6672	1094	66547	65616	101874	12318	471881
89.5	389.5	4511.9			436	6529	1318	61987	68295	100509	11573	491754
90	390	4519.1	115.97	1.4229	521	6571	1648	61388	69370	101650	12332	493725
90.5	390.5	4526.4			474	6541	567	64778	67686	103493	13594	466833

Table S2. Raw magnetic susceptibility (MS), density, and X-ray fluorescence (XRF) data. (cont.)

Depth in core (cm)	Composite Depth in Core (cm)	Calibrated Age (cal yr BP)	MS (SI)	Density (g/cm^3)	Al (cps)	Si (cps)	S (cps)	K (cps)	Ca (cps)	Ti (cps)	Mn (cps)	Fe (cps)
91	391	4533.6	114.44	1.4355	431	6259	901	60226	71290	100850	13495	476107
91.5	391.5	4540.8			485	6456	1349	53480	74211	100105	11501	514754
92	392	4548	114.86	1.4319	498	6316	1022	59717	68105	99971	12692	481949
92.5	392.5	4555.4			468	6580	1028	60685	74450	99468	11534	485044
93	393	4562.7	113.77	1.427	422	6436	773	59411	75356	99753	13773	485199
93.5	393.5	4569.9			462	6590	703	59154	73967	99173	14439	484277
94	394	4577.3	111.21	1.4047	496	6523	1236	61351	69439	99075	13099	476845
94.5	394.5	4584.5			468	6507	2319	63791	62200	98518	10892	476608
95	395	4591.8	105.51	1.4023	486	6665	2168	63918	61575	98948	11170	473355
95.5	395.5	4599.6			540	6447	2019	63798	59640	98101	11717	473559
96	396	4607.3	101.73	1.4049	480	6584	1527	61658	63867	97988	11633	469594
96.5	396.5	4614.9			448	6329	987	58038	67902	97956	11617	471561
97	397	4622.6	99.207	1.4258	473	6581	2061	59101	66720	96621	11378	476760
97.5	397.5	4630.2			471	6336	1957	59173	65386	97377	12466	473985
98	398	4638	93.273	1.4801	479	5766	2048	57594	60867	92910	11703	462644
98.5	398.5	4645.6			458	5571	1856	55188	60310	92184	11494	452623
99	399	4653.2	88.33	1.5007	463	6575	1974	62990	70344	102419	13151	498964
0	400	4668.4			312	4687	1382	49514	55934	83845	7833	401590
0.5	400.5	4675.9			418	5864	1652	58251	67023	99864	9672	473337
1	401	4683.3	91.001	1.4909	503	6630	2649	63246	72436	103572	10977	508141
1.5	401.5	4690.7			443	6538	3085	61215	71011	101475	9992	502969
2	402	4698.3	97.055	1.5179	399	5808	2403	57762	70148	98055	9523	480665
2.5	402.5	4705.9			459	6266	2991	58248	71881	97722	9749	490187
3	403	4713.3	105.52	1.457	445	5997	1563	54909	70645	94858	10629	486942
3.5	403.5	4720.8			464	6088	1796	57207	73566	97981	9708	487631
4	404	4728.2	105.48	1.4592	388	5766	1459	57982	69730	98756	8660	461016
4.5	404.5	4735.6			476	6175	858	63654	67319	104692	11323	454542
5	405	4743.1	104.43	1.4397	491	6537	1427	62665	70661	103577	11174	473478
5.5	405.5	4750.9			454	6392	1589	60401	69427	100244	9674	461457
6	406	4758.7	104.76	1.4027	421	6248	2062	58587	68195	98601	9609	459224

Table S2. Raw magnetic susceptibility (MS), density, and X-ray fluorescence (XRF) data. (cont.)

Depth in core (cm)	Composite Depth in Core (cm)	Calibrated Age (cal yr BP)	MS (SI)	Density (g/cm^3)	Al (cps)	Si (cps)	S (cps)	K (cps)	Ca (cps)	Ti (cps)	Mn (cps)	Fe (cps)
6.5	406.5	4766.5			420	6398	2279	58490	73653	100131	10133	473808
7	407	4774.3	103.23	1.4146	472	6427	3092	56596	75573	98574	9433	482860
7.5	407.5	4782.1			450	6109	2907	54193	77554	96237	10451	475368
8	408	4789.9	101.49	1.4416	405	6163	2920	56097	76165	98950	9314	475147
8.5	408.5	4797.7			420	5888	2775	55391	76175	97189	11081	467564
9	409	4805.5	101.05	1.4307	417	6033	2794	58621	67046	98529	9631	451227
9.5	409.5	4813.2			446	5993	3056	55431	74875	96461	11267	473210
10	410	4821.1	97.433	1.4057	391	6131	3945	53382	77601	94317	9837	469782
10.5	410.5	4828.7			410	5939	9175	52761	70064	90481	9097	532275
11	411	4836.1	84.413	1.4248	386	5207	13724	50065	54766	78636	9640	575048
11.5	411.5	4843.7			337	5288	12799	53565	46596	78196	9073	565061
12	412	4851.1	66.655	1.4042	434	5164	12090	55193	38424	76587	9700	567096
12.5	412.5	4858.7			411	5277	10566	54404	39147	77243	10104	521714
13	413	4866.3	46.51	1.3955	364	5285	10443	55081	48736	81205	10337	501168
13.5	413.5	4873.6			412	5508	12090	56372	40387	78789	11494	492067
14	414	4881.3	30.613	1.4044	426	5529	11358	54703	41995	76966	9859	502935
14.5	414.5	4888.8			361	5105	10351	49630	40667	73842	9001	481325
15	415	4896.2	21.816	1.3783	398	5046	10193	51224	41306	73119	10955	493168
15.5	415.5	4903.6			388	5160	10433	50627	42025	72768	10657	485047
16	416	4911	16.448	1.3599	353	4978	10475	50004	40595	72805	10013	480913
16.5	416.5	4918.5			402	4683	10514	48455	37831	70904	10739	489444
17	417	4925.9	13.967	1.3192	306	4046	8433	44094	33606	63662	8928	459345
17.5	417.5	4933.3			326	3656	8216	39630	32078	58424	9037	439222
18	418	4940.9	12.489	1.2919	370	4628	9345	47140	41757	69917	10132	502348
18.5	418.5	4948.2			308	4412	9275	44126	42429	66631	10511	498493
19	419	4955.4	11.259	1.3272	291	3518	8713	33210	32530	52362	9876	443553
19.5	419.5	4962.9			294	3684	9161	38811	35722	61815	10054	494130
20	420	4970.5	11.073	1.2667	337	3790	9652	39947	37907	64929	10556	513165
20.5	420.5	4978.5			391	4968	8805	50156	51124	79002	9721	480598
21	421	4986.5	10.499	1.2835	379	5742	7131	56019	64208	87965	11964	430109

Table S2. Raw magnetic susceptibility (MS), density, and X-ray fluorescence (XRF) data. (cont.)

Depth in core (cm)	Composite Depth in Core (cm)	Calibrated Age (cal yr BP)	MS (SI)	Density (g/cm^3)	Al (cps)	Si (cps)	S (cps)	K (cps)	Ca (cps)	Ti (cps)	Mn (cps)	Fe (cps)
21.5	421.5	4994.4			327	5071	7534	52537	61088	80150	11683	433555
22	422	5002.3	10.114	1.2962	399	4885	7758	54552	39428	72742	10512	432305
22.5	422.5	5010.2			420	4334	9132	54388	35598	74499	11938	460559
23	423	5018.2	10.173	1.2796	429	5410	8605	57548	49574	80770	11566	449497
23.5	423.5	5026.1			388	5706	6860	53525	64815	86733	10520	435007
24	424	5034.2	9.8723	1.3464	407	5936	6710	52947	71806	90576	10968	444241
24.5	424.5	5041.9			383	5613	7318	50630	71948	87056	10247	453291
25	425	5050.1	10.113	1.3416	362	5557	6840	50362	69071	86324	11648	436216
25.5	425.5	5057.5			334	5481	4877	52880	64102	87322	11788	404666
26	426	5065	9.817	1.3354	287	4875	7166	49472	55401	78529	10768	439999
26.5	426.5	5072.6			411	4767	8562	55066	35557	71424	10660	427406
27	427	5080.1	9.108	1.3185	458	4993	8445	58391	37616	75968	9864	425493
27.5	427.5	5087.8			434	5100	8322	58148	52636	75700	11056	430776
28	428	5095.2	8.5776	1.3039	440	5149	9117	54419	46477	77160	11628	465095
28.5	428.5	5102.7			390	5460	10677	49503	59776	80815	11804	510226
29	429	5110	7.7909	1.3885	408	5691	10572	49189	60508	80382	11560	508776
29.5	429.5	5118			351	5199	10564	47923	55291	76990	11665	496831
30	430	5125.6	7.6856	1.3836	388	4928	8869	51122	45270	75664	9860	455613
30.5	430.5	5133.2			386	4932	8723	52720	41943	74429	10904	437879
31	431	5140.9	7.7048	1.3207	362	4841	8760	50549	44216	73792	11811	445807
31.5	431.5	5148.9			411	4378	8473	48928	41816	71176	11111	440967
32	432	5156.7	7.5443	1.288	410	4432	8134	46381	43806	69516	13034	435617
32.5	432.5	5164.4			352	4309	8412	46452	43321	68773	12576	443650
33	433	5172.3	7.2906	1.3077	372	4698	8387	45427	45902	68838	13116	440342
33.5	433.5	5180			372	4575	8539	45593	45177	67405	12428	434877
34	434	5187.7	7.0544	1.3255	402	4131	8046	43439	43980	67293	11959	421370
34.5	434.5	5195.4			351	4198	9364	46082	42920	70202	11003	425749
35	435	5203.2	7.2342	1.2672	418	4553	9444	51676	43231	73509	12802	430272
35.5	435.5	5210.8			412	4645	8043	53763	40573	71555	10841	425390
36	436	5218.5	7.0843	1.2811	334	4317	8463	48422	40120	71135	11080	433252

Table S2. Raw magnetic susceptibility (MS), density, and X-ray fluorescence (XRF) data. (cont.)

Depth in core (cm)	Composite Depth in Core (cm)	Calibrated Age (cal yr BP)	MS (SI)	Density (g/cm^3)	Al (cps)	Si (cps)	S (cps)	K (cps)	Ca (cps)	Ti (cps)	Mn (cps)	Fe (cps)
36.5	436.5	5226.1			339	4441	8835	52170	37934	73746	10980	440436
37	437	5234.1	6.7778	1.3255	367	4061	8412	48742	37671	69127	11018	412548
37.5	437.5	5241.8			406	4228	9199	52616	40235	73373	10561	422572
38	438	5249.7	6.94	1.2945	369	4400	9314	58612	43406	79091	11511	420617
38.5	438.5	5257.3			447	4631	8870	58944	45659	79822	12245	420710
39	439	5264.9	6.8801	1.3058	413	4488	8929	55701	44251	78411	11868	419060
39.5	439.5	5272.9			382	4717	8632	55791	43288	78397	12564	421549
40	440	5280.6	7.0276	1.3305	439	4921	8793	52959	43423	78917	11340	435589
40.5	440.5	5288.1			473	5367	9018	54054	43592	80770	11235	428923
41	441	5295.6	7.2338	1.3433	406	5037	8911	58552	40426	80227	11284	432375
41.5	441.5	5303.2			362	4975	8912	56837	40322	81165	10707	439403
42	442	5310.8	7.3178	1.3529	416	4758	8952	56134	37139	77737	11233	429287
42.5	442.5	5318.5			373	5317	8474	56240	40572	81934	10477	430795
43	443	5326.2	7.3492	1.3472	409	5402	9109	56437	39521	82153	9562	436935
43.5	443.5	5333.7			441	5592	9750	57514	39021	82334	9720	438352
44	444	5341.4	7.1771	1.3667	383	5412	9192	58474	38283	82536	9855	433261
44.5	444.5	5349.1			467	5276	8651	56625	39384	80636	10404	428016
45	445	5356.7	7.1898	1.3643	387	5292	9791	51454	43942	79943	11008	458776
45.5	445.5	5364.2			383	5207	9254	51169	43848	80822	9646	451356
46	446	5371.6	7.192	1.3766	475	5436	8768	52504	44391	82407	11278	442075
46.5	446.5	5379.3			402	5393	8850	52502	43307	80814	11180	441264
47	447	5386.8	7.332	1.3628	431	5305	8988	52623	43031	80688	12365	445633
47.5	447.5	5394.4			341	4934	8709	52149	41199	78502	10933	445304
48	448	5402.2	7.2314	1.3691	401	5057	9143	52931	41341	77208	12733	441213
48.5	448.5	5409.9			433	5196	9291	54663	39752	78595	11427	441933
49	449	5417.5	7.1451	1.3472	469	4778	9869	54362	40538	78395	12404	442627
49.5	449.5	5425.2			420	4970	9016	50919	42913	76983	13464	441776
50	450	5432.6	7.0775	1.3212	452	5345	9499	52595	44288	78399	11743	448690
50.5	450.5	5440.1			498	4994	9805	57184	38833	78929	11752	434412
51	451	5447.7	6.7296	1.3486	369	4967	9120	54224	39093	78270	13099	431670

Table S2. Raw magnetic susceptibility (MS), density, and X-ray fluorescence (XRF) data. (cont.)

Depth in core (cm)	Composite Depth in Core (cm)	Calibrated Age (cal yr BP)	MS (SI)	Density (g/cm^3)	Al (cps)	Si (cps)	S (cps)	K (cps)	Ca (cps)	Ti (cps)	Mn (cps)	Fe (cps)
51.5	451.5	5455			414	5015	8239	51127	43721	80081	12861	427118
52	452	5462.4	6.569	1.3537	449	5249	8559	51096	43414	78881	12498	435858
52.5	452.5	5469.9			356	4772	8932	47709	40406	74750	12157	431934
53	453	5477.3	6.4913	1.3416	372	4751	8248	46248	39342	75011	12487	422424
53.5	453.5	5484.8			523	5068	8505	45482	42689	76253	11474	426654
54	454	5492.1	6.4261	1.3267	405	5276	8794	45453	44275	76689	11503	425234
54.5	454.5	5499.5			400	4658	8171	45363	41812	75355	11745	416284
55	455	5507	6.3101	1.3366	360	4499	7912	43630	41543	73537	11698	405193
55.5	455.5	5514.6			378	4292	7250	41906	40956	71828	13450	400756
56	456	5522.2	6.6912	1.2741	407	4351	7678	41484	44504	72467	13419	407885
56.5	456.5	5529.9			328	4512	8034	42491	45759	76496	10608	431386
57	457	5537.6	6.7463	1.2909	439	4869	8579	45205	48037	81819	12182	454635
57.5	457.5	5545.5			441	4839	9019	46357	46826	82252	11007	469098
58	458	5553.5	6.6136	1.3723	397	4818	8551	45737	46099	81649	11707	465004
58.5	458.5	5561.5			381	4672	8615	45038	45861	81428	12397	467529
59	459	5569.4	6.8183	1.3848	360	4807	8865	45070	45691	82228	10882	472481
59.5	459.5	5577.4			396	5171	9651	45190	46385	82613	11683	464345
60	460	5585.3	6.7745	1.3938	405	5029	9286	45540	47247	83765	12076	465343
60.5	460.5	5592.6			411	4823	9432	44474	45014	79447	12208	475948
61	461	5600	6.6211	1.3984	390	4442	9411	43950	40330	73648	12784	480367
61.5	461.5	5607.4			465	4602	8904	44264	41995	74799	11213	476403
62	462	5614.6	6.4234	1.3843	377	4757	9600	45428	46923	77005	12665	471995
62.5	462.5	5622			386	4641	8903	45004	46059	75577	13617	450799
63	463	5629.5	6.352	1.371	354	4415	8547	46873	47518	75371	13814	447160
63.5	463.5	5637.1			295	4808	8373	47244	47178	75256	12261	425786
64	464	5644.5	6.1961	1.3611	444	5030	8672	48235	48493	76867	10269	433563
64.5	464.5	5652.1			387	4862	8256	48088	47483	73940	11633	423126
65	465	5659.4	6.1528	1.3558	392	4817	7972	48409	47771	75951	12543	421445
65.5	465.5	5666.9			361	5019	7740	48383	47375	76025	11418	423537
66	466	5674.3	5.9902	1.3773	361	5005	7486	47839	49740	74436	11167	418329

Table S2. Raw magnetic susceptibility (MS), density, and X-ray fluorescence (XRF) data. (cont.)

Depth in core (cm)	Composite Depth in Core (cm)	Calibrated Age (cal yr BP)	MS (SI)	Density (g/cm^3)	Al (cps)	Si (cps)	S (cps)	K (cps)	Ca (cps)	Ti (cps)	Mn (cps)	Fe (cps)
66.5	466.5	5682			360	4925	8532	48915	50137	75713	12506	432621
67	467	5689.8	6.0272	1.3689	359	4693	8329	47986	66247	74637	11884	419569
67.5	467.5	5697.4			354	4692	8139	50269	47253	76974	11056	427690
68	468	5705.2	5.955	1.3701	387	4790	8500	51186	46557	78265	11242	430302
68.5	468.5	5712.9			405	4864	8827	51157	44765	75007	10006	419061
69	469	5720.8	5.9236	1.3773	357	4897	8592	51038	46324	76859	11576	423337
69.5	469.5	5728.5			447	4789	8504	51275	44545	76477	12148	423441
70	470	5736.4	5.8232	1.3696	334	4866	8891	49373	44980	76738	10266	430424
70.5	470.5	5743.5			390	5051	8429	47820	46063	75562	11474	415270
71	471	5750.8	5.6821	1.3875	422	4930	8260	48089	43902	74229	9540	407060
71.5	471.5	5757.9			370	5113	8775	50283	42155	75046	10082	406214
72	472	5765	5.7308	1.3597	440	5134	8947	51493	42916	75130	10353	409954
72.5	472.5	5772.2			404	5081	8486	51331	45551	74425	11632	417368
73	473	5779.5	5.9773	1.2729	372	5075	8509	49573	48029	74322	11862	407738
73.5	473.5	5787			420	4977	8523	49653	49302	74368	11697	415758
74	474	5794.4	5.742	1.357	418	5205	9106	49464	49922	75762	11684	419749
74.5	474.5	5801.9			406	5205	8803	52573	47664	76963	11977	415425
75	475	5809.4	5.9839	1.3788	392	4997	8534	49970	50627	77018	9958	416368
75.5	475.5	5817.6			370	4949	8753	48715	49758	77531	10903	424856
76	476	5825.8	6.1998	1.3899	377	4949	8274	49247	48460	77088	10232	423059
76.5	476.5	5834			353	5141	8892	49881	49102	79082	11018	425733
77	477	5842.3	6.388	1.3633	417	5098	9175	48426	49912	77265	11098	421375
77.5	477.5	5850.6			293	5075	8245	49578	46585	75881	10724	417600
78	478	5858.9	6.4324	1.3681	365	4769	8170	48636	47569	75979	10741	422893
78.5	478.5	5867			377	5108	8082	51729	46885	76774	11935	416259
79	479	5874.9	6.6002	1.3611	390	5097	8485	48590	48794	78460	10879	423714
79.5	479.5	5882.6			394	4833	7870	47146	48974	77201	12118	419948
80	480	5890.3	6.7294	1.3759	335	5157	8791	48688	50239	78757	11019	431580
80.5	480.5	5898.9			411	5259	9946	46967	50989	77204	10448	429351
81	481	5907.4	6.6816	1.4132	352	5240	10158	45290	54475	79874	10951	445322

Table S2. Raw magnetic susceptibility (MS), density, and X-ray fluorescence (XRF) data. (cont.)

Depth in core (cm)	Composite Depth in Core (cm)	Calibrated Age (cal yr BP)	MS (SI)	Density (g/cm^3)	Al (cps)	Si (cps)	S (cps)	K (cps)	Ca (cps)	Ti (cps)	Mn (cps)	Fe (cps)
81.5	481.5	5916.1			384	5031	10088	43612	55641	78903	10971	454175
82	482	5924.6	6.977	1.4059	416	4925	9604	44153	55129	79702	10396	451262
82.5	482.5	5933.1			430	5123	9529	44525	55990	79445	9692	448046
83	483	5941.7	6.9963	1.4151	364	5086	9064	44789	55953	79312	10953	445828
83.5	483.5	5950.2			373	5180	9387	44115	56858	78644	11837	449284
84	484	5958.7	7.1185	1.4166	403	5261	9764	42853	59685	79646	11845	463804
84.5	484.5	5967.1			412	5423	9695	40759	62233	79162	10674	463311
85	485	5975.2	7.2315	1.4071	406	5340	8694	41584	62786	80578	11746	461323
85.5	485.5	5984			361	5183	9752	41011	62362	79209	11020	465845
86	486	5992.7	7.3441	1.4105	384	5313	8734	40872	64175	78683	12469	455444
86.5	486.5	6001.4			388	5298	8506	43770	61200	77671	12653	439602
87	487	6010	7.6034	1.3865	398	5297	9156	43152	64915	78480	10377	443197
87.5	487.5	6018.7			381	5356	9096	41614	72070	77354	11597	445375
88	488	6027.3	7.6122	1.4331	408	5459	8635	41741	63185	79225	10458	450295
88.5	488.5	6035.9			325	5845	8634	42439	64930	82394	9213	452393
89	489	6044.5	7.823	1.4531	455	5591	8212	38646	73641	81215	11255	444438
89.5	489.5	6053.3			337	6061	7899	38151	76222	81857	10284	436495
90	490	6061.9	8.0619	1.4555	356	5784	8155	37779	74860	84130	11062	436199
90.5	490.5	6070.5			373	5538	8266	36995	76274	82870	10200	444982
91	491	6079.3	8.1604	1.4492	366	5472	7718	36824	73588	82581	10639	427831
91.5	491.5	6088			341	5726	8506	36675	76564	81344	10625	429111
92	492	6096.8	7.9273	1.4455	390	5875	10769	36826	70534	80073	10821	460751
92.5	492.5	6105.4			346	4813	13070	36495	54872	73885	8507	513768
93	493	6113.9	7.6075	1.4219	400	4936	10966	37291	52095	72886	10583	493891
93.5	493.5	6122.6			337	4860	10425	37844	50632	72512	11518	470090
94	494	6131.4	7.2842	1.3718	275	4510	10016	37179	43017	69077	10615	466552
94.5	494.5	6140.1			395	4540	9538	41117	42653	73356	10665	454898
95	495	6148.8	7.0077	1.3474	355	4721	9634	38735	47082	73723	10010	455054
95.5	495.5	6157.6			360	4547	9355	38726	48896	72772	9605	445130
96	496	6166.3	6.6125	1.3447	277	4770	9057	38915	50881	72607	10166	440205

Table S2. Raw magnetic susceptibility (MS), density, and X-ray fluorescence (XRF) data. (cont.)

Depth in core (cm)	Composite Depth in Core (cm)	Calibrated Age (cal yr BP)	MS (SI)	Density (g/cm^3)	Al (cps)	Si (cps)	S (cps)	K (cps)	Ca (cps)	Ti (cps)	Mn (cps)	Fe (cps)
96.5	496.5	6175.2			390	4416	9025	38319	47673	70003	12250	439784
97	497	6183.9	6.6432	1.2971	378	4345	8682	39223	44343	71932	11914	427884
97.5	497.5	6192.6			339	4348	8511	42162	41537	74120	10901	418062
98	498	6201.6	6.3488	1.3573	345	4363	8223	41713	38930	73296	10045	428676
98.5	498.5	6210.4			391	5136	8833	40620	41423	74587	10333	462981
99	499	6219.3	6.2582	1.4355	377	5598	10513	42020	52608	77383	10406	485462
99.5	499.5	6228.3			400	5495	8160	29454	48856	60692	9513	362235
0	500	6237.1	7.7694	1.2035	398	3945	23801	35100	326295	61227	7660	440255
0.5	500.5	6245.5			393	4019	19987	36493	276253	64595	8174	431667
1	501	6254	8.1748	1.256	423	4496	19747	39886	234843	71052	9227	453967
1.5	501.5	6262.5			360	4595	18233	38689	223714	69155	8422	441518
2	502	6270.9	7.9164	1.4243	440	4692	15665	42492	200683	72039	9915	435675
2.5	502.5	6279.4			386	4438	16522	39486	222222	67917	10293	421488
3	503	6287.7	8.9539	1.3822	375	4090	21062	37577	296575	66267	8271	428273
3.5	503.5	6296.2			345	3666	27036	34320	375466	60293	7238	421005
4	504	6304.2	10.101	1.325	406	3859	23413	36037	298365	62783	9084	455000
4.5	504.5	6312.5			408	4146	17897	36729	217714	64932	8947	476040
5	505	6320.8	11.354	1.2919	327	4168	15528	40769	162318	67459	9267	460529
5.5	505.5	6329.1			404	4558	11502	48020	118138	74681	9776	432736
6	506	6337.6	12.438	1.2751	428	4615	10875	50481	118009	79236	6979	422147
6.5	506.5	6346.2			381	4987	8723	50601	95881	80073	8887	429203
7	507	6354.6	12.563	1.2988	497	5046	12321	50151	174447	78328	7112	416841
7.5	507.5	6363.1			421	5036	14903	47543	227650	78120	8419	417767
8	508	6371.5	11.983	1.3005	410	5281	9164	51438	96773	82790	8759	442121
8.5	508.5	6380			455	5429	8442	52030	81889	84448	9736	434394
9	509	6388.6	10.928	1.3171	430	5381	8547	45927	73539	81317	10462	432292
9.5	509.5	6396.9			430	5260	9368	45400	67815	80357	9539	424029
10	510	6405.1	9.5942	1.3281	399	5213	9402	47227	64520	83006	8676	421331
10.5	510.5	6413.8			430	5291	9460	46384	63667	83309	8718	432693
11	511	6422.2	8.3008	1.3252	435	5147	8725	46913	63674	79875	8254	424267

Table S2. Raw magnetic susceptibility (MS), density, and X-ray fluorescence (XRF) data. (cont.)

Depth in core (cm)	Composite Depth in Core (cm)	Calibrated Age (cal yr BP)	MS (SI)	Density (g/cm^3)	Al (cps)	Si (cps)	S (cps)	K (cps)	Ca (cps)	Ti (cps)	Mn (cps)	Fe (cps)
11.5	511.5	6430.7			414	5309	8617	47933	63687	81897	8624	421718
12	512	6439.2	7.3593	1.3079	415	4945	9965	46724	63807	77158	9545	432012
12.5	512.5	6447.7			477	5344	9511	47198	64870	81923	7846	448077
13	513	6456.5	6.6195	1.3156	388	4849	8435	41350	61715	75589	9774	432756
13.5	513.5	6465.1			344	4846	7936	39843	65071	74919	9472	447968
14	514	6473.5	6.1941	1.332	359	4848	7993	42280	62815	76487	8163	431329
14.5	514.5	6482			367	4745	7498	41451	62747	74887	8669	436610
15	515	6490.4	6.1297	1.331	371	4628	7889	43895	60920	75975	8577	416797
15.5	515.5	6499.3			423	4439	7442	43372	60851	74057	9608	416753
16	516	6508.2	6.0932	1.3089	375	4374	8125	41848	61718	73644	9075	433174
16.5	516.5	6517			344	4551	6829	38130	59358	69329	8271	429775
17	517	6525.8	5.9477	1.3101	348	4087	6922	39392	55275	67989	7882	408923
17.5	517.5	6534.8			381	3967	8499	38817	53872	66513	10019	426225
18	518	6543.8	5.9597	1.3075	327	4045	8278	34700	52754	64786	8102	432009
18.5	518.5	6552.8			357	3980	8892	38728	51518	69762	8923	423885
19	519	6561.7	6.0086	1.2816	327	4436	8709	43377	51665	73845	8155	417253
19.5	519.5	6570.6			387	4483	8594	45922	50724	78504	8647	405288
20	520	6579.6	5.8431	1.3022	345	4320	8260	41010	53531	76625	8305	415886
20.5	520.5	6587.9			360	4646	7042	41854	54339	75498	8429	403981
21	521	6596.3	5.9026	1.3046	353	4605	8130	46297	53625	79353	8868	395289
21.5	521.5	6604.7			375	4508	8196	45065	53165	74550	9395	392009
22	522	6613	5.794	1.3132	357	4268	8377	46593	51016	75434	9311	401314
22.5	522.5	6621.4			316	4257	8686	46722	48127	75758	8909	399775
23	523	6629.9	5.8528	1.3	352	4738	7608	44711	53179	77400	8124	414766
23.5	523.5	6638.3			380	4454	8178	41468	51077	72913	9624	404184
24	524	6646.5	5.8713	1.3115	343	4374	6688	36899	49531	70922	8085	435182
24.5	524.5	6655.1			263	4383	7855	41167	50914	74007	6744	407322
25	525	6663.3	6.0192	1.325	385	4734	8547	43774	49607	74891	7927	416437
25.5	525.5	6671.5			432	4634	7771	41356	51475	73043	6953	417155
26	526	6679.9	6.1834	1.3195	379	4571	7401	41299	50475	74703	8370	418423

Table S2. Raw magnetic susceptibility (MS), density, and X-ray fluorescence (XRF) data. (cont.)

Depth in core (cm)	Composite Depth in Core (cm)	Calibrated Age (cal yr BP)	MS (SI)	Density (g/cm^3)	Al (cps)	Si (cps)	S (cps)	K (cps)	Ca (cps)	Ti (cps)	Mn (cps)	Fe (cps)
26.5	526.5	6688.2			412	4502	7097	37588	49384	72853	8899	431415
27	527	6696.5	6.2031	1.3301	391	4857	7802	42624	48186	73039	7737	422301
27.5	527.5	6704.8			387	4575	8771	43003	46363	73617	7949	416279
28	528	6713.2	6.1796	1.3351	415	4620	8428	42480	50947	71710	6554	414698
28.5	528.5	6721.5			419	4837	8447	45524	50891	77014	8734	406427
29	529	6729.7	6.305	1.294	380	4903	8930	45552	53705	75798	7980	418780
29.5	529.5	6738			362	4590	9730	47133	53290	75132	8843	415708
30	530	6746.3	6.1146	1.3043	275	4411	9352	45715	136331	71458	8857	386385
30.5	530.5	6755.1			269	3480	7524	37462	737148	52114	14195	240667
31	531	6763.6	5.9292	1.3142	437	4776	9738	48724	57435	77064	7987	426559
31.5	531.5	6772.5			384	4613	9015	44981	77181	73522	8227	411919
32	532	6781.1	5.9109	1.3183	397	4563	9235	45376	79410	73873	8551	421204
32.5	532.5	6790.1			346	4477	10175	46788	61099	74885	8784	422973
33	533	6798.7	5.931	1.2983	374	4469	10304	48328	68159	75773	9107	423688
33.5	533.5	6807.4			391	4239	9602	41249	91595	71778	9205	446796
34	534	6816.2	6.0272	1.2928	406	4339	9504	44429	70296	75530	8603	428021
34.5	534.5	6824.9			388	4438	8636	47117	61278	80676	8132	411892
35	535	6833.8	5.9674	1.3058	300	4018	8234	43676	60107	75007	8909	410187
35.5	535.5	6842.4			323	4030	7819	42241	63565	75768	8622	405819
36	536	6850.7	5.9489	1.3252	323	3957	8736	43157	65992	73656	8913	416468
36.5	536.5	6859.3			422	4485	9174	41389	67490	75358	8570	435735
37	537	6867.9	5.9368	1.3125	341	4428	9107	43367	62114	77919	8711	432784
37.5	537.5	6876.4			374	4193	9132	45156	60032	75987	9281	410660
38	538	6885.1	5.8101	1.3411	388	3924	9699	43997	68718	75932	10494	410726
38.5	538.5	6893.8			342	4055	9574	44937	65918	76666	9282	410546
39	539	6902.2	5.7898	1.2983	353	4062	9967	46351	58565	76364	9981	413770
39.5	539.5	6910.7			280	4220	9938	45336	56448	75639	10184	419668
40	540	6918.9	5.4901	1.3024	397	4565	9256	44624	54940	76269	8539	410105
40.5	540.5	6927.7			404	4535	9302	49145	52633	79829	9194	411996
41	541	6936.5	5.2811	1.3192	415	4286	9436	45052	51692	77933	9264	423467

Table S2. Raw magnetic susceptibility (MS), density, and X-ray fluorescence (XRF) data. (cont.)

Depth in core (cm)	Composite Depth in Core (cm)	Calibrated Age (cal yr BP)	MS (SI)	Density (g/cm^3)	Al (cps)	Si (cps)	S (cps)	K (cps)	Ca (cps)	Ti (cps)	Mn (cps)	Fe (cps)
41.5	541.5	6945.2			335	4264	9684	45247	51195	76463	9083	423940
42	542	6954.1	5.2153	1.3007	360	4268	10238	48890	47917	78934	8917	416865
42.5	542.5	6962.8			346	4200	9362	47588	47510	76641	9520	417933
43	543	6971.6	5.255	1.2909	408	4339	9266	50882	46787	80624	9743	415975
43.5	543.5	6980.4			372	4072	8369	44344	50139	76432	9599	416299
44	544	6989.1	5.3412	1.2701	344	4081	9122	43748	49411	73823	8725	425071
44.5	544.5	6998			375	4120	9113	45993	51264	76282	10062	419182
45	545	7006.6	5.3231	1.2916	364	4052	8322	41110	56033	76402	9037	434259
45.5	545.5	7015.2			297	4201	8368	42181	54166	75430	10338	426068
46	546	7023.6	5.384	1.294	399	4502	8822	43816	53134	76240	10214	430197
46.5	546.5	7032.3			363	4784	8177	44400	54633	79325	8562	438435
47	547	7040.8	5.567	1.2844	317	4411	8141	44441	50837	77921	9122	432839
47.5	547.5	7049.3			384	4364	9221	43363	47391	77839	9156	448018
48	548	7057.9	5.644	1.3156	381	4319	8715	41095	46248	75009	8984	439928
48.5	548.5	7066.5			383	4418	9118	39330	44493	76551	8648	469875
49	549	7074.8	6.1828	1.2899	360	5035	5117	31744	46029	81955	6301	536658
49.5	549.5	7083.2			409	4921	2731	27879	48100	82243	7041	563998
50	550	7091.7	6.6084	1.3595	394	4904	2653	28112	47016	84833	6057	594251
50.5	550.5	7100.2			341	5041	2717	26606	48207	81731	6053	602891
51	551	7108.6	7.07	1.4263	364	4853	2527	24654	49652	79547	6169	596978
51.5	551.5	7117			337	5093	2513	22261	52684	77190	5815	598563
52	552	7125.4	7.7857	1.4129	389	4866	2662	20420	56323	73296	7023	610928
52.5	552.5	7133.8			323	4692	2772	22539	52785	77170	6042	604128
53	553	7142.3	8.3153	1.3781	371	5026	2826	23479	51138	78582	5088	596011
53.5	553.5	7150.6			342	5060	2679	24006	50640	79673	6645	588861
54	554	7159	8.2858	1.394	413	5230	2555	24528	50963	79167	5466	585398
54.5	554.5	7167.6			362	5173	2552	22800	52144	77543	5233	578476
55	555	7175.9	8.1884	1.3882	424	4850	2636	18599	60356	73462	5331	592690
55.5	555.5	7183.7			325	4339	4710	21127	61505	65560	6704	566630
56	556	7191.3	7.7936	1.388	338	4487	8630	44232	44041	78155	8071	414982

Table S2. Raw magnetic susceptibility (MS), density, and X-ray fluorescence (XRF) data. (cont.)

Depth in core (cm)	Composite Depth in Core (cm)	Calibrated Age (cal yr BP)	MS (SI)	Density (g/cm^3)	Al (cps)	Si (cps)	S (cps)	K (cps)	Ca (cps)	Ti (cps)	Mn (cps)	Fe (cps)
56.5	556.5	7199			401	4585	9105	49358	44621	81012	7716	423543
57	557	7206.8	7.3873	1.3154	385	4462	8687	45310	44461	77500	8167	410641
57.5	557.5	7214.8			423	4147	9112	41331	45945	74391	9131	422904
58	558	7222.9	6.6596	1.3077	362	4263	9347	42010	46634	76515	8212	430176
58.5	558.5	7230.9			345	4473	8919	42410	46735	79400	8504	453482
59	559	7239	5.6226	1.3043	368	4375	9690	41351	46268	77999	7586	448324
59.5	559.5	7247.1			362	4419	10058	42632	47509	78278	9433	448182
60	560	7255.1	5.8437	1.3334	434	4787	9971	39069	51775	76510	7588	467154
60.5	560.5	7260.1			401	4343	11099	46241	54569	80698	8658	447267
61	561	7265.2	5.9619	1.3224	408	4604	10901	44459	50012	79213	9195	441861
61.5	561.5	7270			364	4410	10585	44880	48407	78022	8477	437535
62	562	7274.7	5.8032	1.3269	403	4375	10786	43508	48503	74901	8685	441335
62.5	562.5	7279.4			363	4378	10519	41571	48613	73529	9970	449639
63	563	7283.9	5.8169	1.3238	376	4279	9517	41592	49746	73254	9011	427528
63.5	563.5	7288.5			344	4509	9641	42924	48694	76057	8137	432425
64	564	7293.3	5.7885	1.3303	372	4694	9516	44044	49101	77560	8553	434548
64.5	564.5	7297.9			335	4887	9341	43125	47480	77363	9591	442814
65	565	7302.5	5.7284	1.3443	408	4980	9547	42426	44459	75082	8738	432246
65.5	565.5	7307.8			386	4720	9707	43068	45496	74706	9045	422192
66	566	7312.9	5.6897	1.3373	391	4583	9822	45056	41295	77465	8458	417191
66.5	566.5	7318			368	4564	8912	42968	40423	75810	7683	403163
67	567	7323.1	5.6737	1.2926	377	4739	9465	45990	38446	77425	8529	408868
67.5	567.5	7328.2			390	4402	9237	44974	36118	77638	9319	405083
68	568	7333.3	5.5114	1.2974	331	4319	9000	45422	37301	77895	9584	411265
68.5	568.5	7338.5			424	4332	9205	46561	37653	79512	9452	419972
69	569	7343.6	5.5742	1.2828	441	4583	8644	43875	41092	77927	8684	420349
69.5	569.5	7348.8			421	4473	7502	43149	42824	76800	8607	411763
70	570	7353.9	5.651	1.2816	401	4859	7573	44102	44175	79310	9008	420328
70.5	570.5	7358.9			414	4522	7452	41754	39663	78358	8623	424550
71	571	7364.2	5.6133	1.3065	390	4896	7866	42896	40960	79901	8051	437677

Table S2. Raw magnetic susceptibility (MS), density, and X-ray fluorescence (XRF) data. (cont.)

Depth in core (cm)	Composite Depth in Core (cm)	Calibrated Age (cal yr BP)	MS (SI)	Density (g/cm^3)	Al (cps)	Si (cps)	S (cps)	K (cps)	Ca (cps)	Ti (cps)	Mn (cps)	Fe (cps)
71.5	571.5	7369.5			337	4692	7519	42118	39511	79950	8670	429027
72	572	7374.7	5.7304	1.3118	449	4752	7511	43009	39606	79276	9254	423413
72.5	572.5	7379.9			335	4824	7839	43839	40745	80240	7975	428711
73	573	7385.2	5.7971	1.3125	373	4728	7555	42473	40479	77457	7357	418699
73.5	573.5	7390.5			365	4763	8856	41171	43771	77492	8957	433804
74	574	7395.6	5.8745	1.3108	301	4510	8307	40303	40725	76598	7570	431095
74.5	574.5	7401			359	4480	8251	41635	40666	77317	7915	428822
75	575	7406	5.8659	1.3127	353	4472	8364	40231	39659	76682	7292	430761
75.5	575.5	7411.2			434	4476	8486	40436	39980	77321	9447	439735
76	576	7416	5.776	1.3173	346	4589	9000	40235	41547	78955	7981	445395
76.5	576.5	7421.2			341	4580	9076	38652	41577	77170	8279	433502
77	577	7426.3	5.795	1.313	372	4390	8853	38747	40815	76951	8323	437223
77.5	577.5	7431.4			356	4263	9559	37921	40804	77305	9006	445643
78	578	7436.7	5.8137	1.3245	306	4239	9964	37547	40076	77701	8441	446391
78.5	578.5	7441.6			366	4395	9839	37582	40215	77829	8804	441125
79	579	7446.7	5.8064	1.3262	339	4609	10823	35928	42587	76631	8481	451203
79.5	579.5	7451.9			360	4510	11850	35439	43944	76854	8242	470083
80	580	7457.1	5.8237	1.338	384	4513	11759	35671	44428	75825	10109	465928
80.5	580.5	7462.1			360	4090	11441	32564	45226	71965	8716	459489
81	581	7467.1	5.8258	1.3375	313	4247	11785	32472	47890	73537	8040	465064
81.5	581.5	7472.2			379	4724	12369	34031	49791	74891	7906	473243
82	582	7477.4	5.9349	1.3284	323	4286	10984	33335	48642	72403	7980	455841
82.5	582.5	7482.6			329	4039	11284	31086	48759	69979	8937	447484
83	583	7487.6	5.9076	1.319	297	3750	10665	31055	47922	69281	7264	441232
83.5	583.5	7492.7			335	4109	10452	32644	47358	68909	8741	438679
84	584	7497.8	5.8787	1.3255	360	3968	10184	33067	45237	67925	8969	431266
84.5	584.5	7502.9			328	3886	10110	31931	47380	67498	9661	434746
85	585	7508	5.8777	1.3101	327	3775	10373	31905	48699	69221	8370	439391
85.5	585.5	7513.1			387	3829	10091	31333	48464	69151	9049	436456
86	586	7518.5	5.8328	1.3202	301	3984	9878	32044	48764	68934	9203	429591

Table S2. Raw magnetic susceptibility (MS), density, and X-ray fluorescence (XRF) data. (cont.)

Depth in core (cm)	Composite Depth in Core (cm)	Calibrated Age (cal yr BP)	MS (SI)	Density (g/cm^3)	Al (cps)	Si (cps)	S (cps)	K (cps)	Ca (cps)	Ti (cps)	Mn (cps)	Fe (cps)
86.5	586.5	7523.7			314	3566	9417	30430	44892	65627	8065	415189
87	587	7529	5.7388	1.3099	256	3798	9838	31473	46368	67014	8784	418847
87.5	587.5	7534.2			284	3754	10181	31894	51969	67620	9141	422048
88	588	7539.6	5.7973	1.2808	340	4059	9908	31971	51142	68034	8121	424769
88.5	588.5	7544.7			338	4098	9936	31804	52647	65979	9346	424006
89	589	7549.9	5.5692	1.3168	321	4285	9530	30148	49078	66053	7947	439255
89.5	589.5	7555.2			303	4075	9161	29819	44078	64670	8408	434510
90	590	7560.5	5.658	1.2962	316	4000	8833	29443	39115	62054	8195	426023
90.5	590.5	7565.4			339	3676	8707	29538	42368	62774	8331	410439
91	591	7570.5	5.6049	1.2921	314	3652	8654	27751	39332	60898	8369	390393
91.5	591.5	7575.6			335	3953	9068	30821	40772	63210	7744	422551
92	592	7580.5	5.4559	1.2938	310	3952	8467	28510	39786	60033	8169	425920
92.5	592.5	7585.5			252	3766	8364	28048	42438	60057	8325	414837
93	593	7590.6	5.4741	1.2895	345	3857	8667	29606	45085	62537	9222	420959
93.5	593.5	7595.6			300	3865	8872	30054	46209	62315	8984	417418
94	594	7600.8	5.4518	1.2947	292	4323	8595	31613	45639	64691	9100	434454
94.5	594.5	7605.9			301	3971	9095	31849	42084	64598	8282	418337
95	595	7611	5.5308	1.2928	345	3615	8656	28019	43702	57959	9249	408361
95.5	595.5	7622			311	3706	9025	29370	45766	60067	8670	409844
96	596	7633	5.6953	1.2555	320	3837	9333	30215	46271	60091	9072	417616
96.5	596.5	7644.2			348	3983	9554	31859	44395	62206	9216	421895
97	597	7655.3	5.6921	1.2562	306	3806	9706	32331	40175	60256	7893	418773
97.5	597.5	7666.4			328	3520	9771	30209	42630	60559	8474	427437
98	598	7677.3			313	3341	10712	28592	41579	58641	8308	446958
98.5	598.5	7688.2			277	3177	9095	25114	36135	51672	6490	390140
99	599	7698.9	5.6785	1.3399	308	3961	10095	28312	36596	56866	7972	418620
99.5	599.5	7709.8			439	5047	13056	34195	42014	66235	8080	442437
0	600	7720.7	5.9887	1.3317	287	2810	6534	23274	29529	50206	3290	412931
0.5	600.5	7735			292	3526	9114	30702	39213	61014	6851	484493
1	601	7749.4	15.476		335	4059	9397	32975	40869	62990	7183	450269

Table S2. Raw magnetic susceptibility (MS), density, and X-ray fluorescence (XRF) data. (cont.)

Depth in core (cm)	Composite Depth in Core (cm)	Calibrated Age (cal yr BP)	MS (SI)	Density (g/cm^3)	Al (cps)	Si (cps)	S (cps)	K (cps)	Ca (cps)	Ti (cps)	Mn (cps)	Fe (cps)
2	602	7778.2	5.7899	1.3933	328	3774	8912	31667	47549	61828	7554	424468
2.5	602.5	7792.8			359	3965	9089	32327	48161	62571	6928	431993
3	603	7807.2	5.9071	1.3346	269	3626	8692	28449	49539	62256	7381	429755
3.5	603.5	7821.7			332	3780	9115	31341	45464	63286	7302	447882
4	604	7836.2	5.9946	1.3151	302	3762	9332	31553	46212	64535	7191	452143
4.5	604.5	7850.9			320	4513	9308	30769	42459	64756	7300	458791
5	605	7865.1	5.7448	1.3404	368	4682	9278	32967	41002	66887	7114	472357
5.5	605.5	7879.2			374	4603	10418	31860	39223	67499	7300	489188
6	606	7892.9	5.7089	1.3488	309	3676	9799	30373	41137	59941	8223	419753
6.5	606.5	7907			267	4123	9755	31318	44997	61249	7292	406112
7	607	7920.8	5.606	1.3409	322	3998	9490	30974	45515	60304	7245	413416
7.5	607.5	7934.8			396	4053	8847	31807	45260	59386	7805	405645
8	608	7948.5	5.7021	1.2701	337	4127	9209	31023	50126	60170	9241	422007
8.5	608.5	7962.4			389	4404	10007	32283	44732	59988	8550	419909
9	609	7976.2	5.4247	1.3012	359	4144	9897	31742	50268	62220	8390	425258
9.5	609.5	7989.8			355	4477	9559	34372	46401	63904	7309	430026
10	610	8003.6	5.4539	1.3111	347	4244	9754	33884	47711	63413	7944	441617
10.5	610.5	8017.5			367	4394	9951	33495	49084	62761	8063	435357
11	611	8031.3	5.3338	1.3578	313	4009	9621	33123	47748	59987	9572	413010
11.5	611.5	8045.1			307	4157	9475	31850	49791	60846	7732	412928
12	612	8059	5.331	1.3585	329	3896	9425	28926	47009	57837	8941	397069
12.5	612.5	8073			284	3924	9651	29517	47486	58685	8080	402521
13	613	8087	5.3926	1.326	361	3899	9090	29224	48004	57919	7543	394007
13.5	613.5	8100.7			383	4280	10170	31706	49102	63612	7403	430288
14	614	8114.6	5.4087	1.3051	332	4449	10358	31308	50611	63572	8797	439426
14.5	614.5	8128.5			301	4473	10320	30595	48938	61862	8551	439075
15	615	8142.3	5.2229	1.3515	291	4049	10027	27990	46119	59935	8946	426715
15.5	615.5	8156.3			277	3832	9870	27373	47269	59035	9611	416121
16	616	8170.5	5.2966	1.3154	322	3936	9807	25496	46578	57771	8693	413687
16.5	616.5	8184.7			353	3797	9013	24720	42408	55919	9643	407486

Table S2. Raw magnetic susceptibility (MS), density, and X-ray fluorescence (XRF) data. (cont.)

Depth in core (cm)	Composite Depth in Core (cm)	Calibrated Age (cal yr BP)	MS (SI)	Density (g/cm^3)	Al (cps)	Si (cps)	S (cps)	K (cps)	Ca (cps)	Ti (cps)	Mn (cps)	Fe (cps)
17	617	8198.9	5.2511	1.2919	290	3813	9592	24428	44157	55977	8581	405841
17.5	617.5	8213			285	3816	9974	25603	44998	56217	9883	404631
18	618	8227.3	5.1647	1.278	312	3720	9812	24102	44151	54229	9776	402347
18.5	618.5	8241.3			299	3557	9479	23809	39682	52189	8501	394587
19	619	8255.6	5.1509	1.2636	300	3526	10346	24535	41483	53665	8771	398531
19.5	619.5	8269.6			274	3735	10160	24327	42311	52451	8048	393722
20	620	8283.7	5.1969	1.2701	346	3623	10459	23249	42354	52399	8291	396843
20.5	620.5	8297.8			386	3451	9691	22288	41236	50813	9315	380169
21	621	8311.5	5.6074	1.2588	292	3844	9864	21587	50604	52207	8583	387916
21.5	621.5	8325.4			250	3440	9590	17440	60122	49135	9440	390226
22	622	8339.2	6.5875	1.2385	284	3410	8772	17636	66627	51265	9946	386308
22.5	622.5	8353.1			336	4178	7313	19717	69238	59464	8829	395921
23	623	8367	8.0186	1.2919	310	3364	4123	16457	63735	55206	9720	309515
23.5	623.5	8380.9			167	940	3967	4950	56268	14094	14196	73600
24	624	8394.5	10.27	1.2943	245	2802	3800	14550	61103	43165	10659	237136
24.5	624.5	8408.2			335	3803	3276	19373	61348	59975	10237	334038
25	625	8422.1	14.046	1.1617	335	4350	2799	21518	62706	62069	8951	334224
25.5	625.5	8429.1			308	4409	3201	21807	65178	63794	9636	336169
26	626	8436.1	14.75	1.2493	386	4968	2787	23159	64810	66394	9069	349879
26.5	626.5	8443.1			408	4969	2597	23638	64595	67465	8755	350887
27	627	8450.2	14.907	1.2914	333	4273	2557	20298	65173	63516	10888	312468
27.5	627.5	8457			357	4565	2883	22062	63365	63977	8742	344576
28	628	8464.1	14.942	1.2638	332	4349	2957	19522	59141	59679	10108	329403
28.5	628.5	8471			325	3939	3117	18731	59489	55531	10329	313028
29	629	8478.2	14.31	1.2684	304	4195	2942	19248	61494	55789	9517	305211
29.5	629.5	8485.3			326	3682	3006	17573	57549	48896	9511	249827
30	630	8492.6	14.225	1.2438	339	4164	2673	19845	59275	56390	9860	281730
30.5	630.5	8498.1			395	4681	2655	22226	59317	60609	9304	318213
31	631	8503.7	13.735	1.2615	380	4652	3037	22148	60535	64070	9245	347755
31.5	631.5	8509.1			409	5136	2845	23398	59619	64424	10485	364302

Table S2. Raw magnetic susceptibility (MS), density, and X-ray fluorescence (XRF) data. (cont.)

Depth in core (cm)	Composite Depth in Core (cm)	Calibrated Age (cal yr BP)	MS (SI)	Density (g/cm^3)	Al (cps)	Si (cps)	S (cps)	K (cps)	Ca (cps)	Ti (cps)	Mn (cps)	Fe (cps)
32	632	8514.6	13.494	1.284	290	3442	3625	15954	50453	47319	12246	248926
32.5	632.5	8520.1			429	5308	2169	26077	57822	70971	7003	362255
33	633	8525.6	12.989	1.3127	418	5561	1987	26278	57171	72914	6860	356140
33.5	633.5	8531			408	5350	2302	25719	58174	73550	7768	362631
34	634	8536.4	12.403	1.3378	346	5362	2724	26390	57988	73298	8003	372979
34.5	634.5	8541.9			428	5556	2228	26984	59542	74438	7256	364068
35	635	8547.4	12.02	1.3346	364	5843	2102	26743	60718	74212	7822	374563
35.5	635.5	8552.9			426	5382	2431	25086	60033	71445	8883	356292
36	636	8558.3	11.745	1.3269	360	4906	2682	22268	59916	66865	8557	325103
36.5	636.5	8563.9			280	3597	4042	17974	69695	61433	8665	302211
37	637	8569.2	11.421	1.3163	428	4465	2690	23432	53692	68768	8905	302618
37.5	637.5	8574.9			361	4921	3054	23969	55951	74577	10585	329512
38	638	8580.3	11.229	1.2899	393	5941	2049	28080	62631	76401	7917	367562
38.5	638.5	8585.7			423	5984	2549	28192	62753	75158	7630	387729
39	639	8591.2	10.495	1.3276	410	5181	2298	25011	60540	69148	8832	346155
39.5	639.5	8596.6			355	3848	3393	20075	62974	58956	8747	290091
40	640	8602.2	9.7414	1.3645	216	2668	3382	13138	46126	40407	11979	201032
40.5	640.5	8607.6			423	4558	3128	22280	57275	63758	8159	309568
41	641	8613	9.7583	1.2588	414	5531	2455	30971	56154	75879	8124	338341
41.5	641.5	8618.6			404	6143	1784	34362	55874	78971	7071	345100
42	642	8623.9	9.1775	1.2586	336	4372	3149	21629	56302	63445	7994	295760
42.5	642.5	8629.5			381	5149	2425	26322	54796	70120	8663	320689
43	643	8635	8.4823	1.3185	465	5029	2515	25358	51950	66902	6929	308914
43.5	643.5	8640.4			420	4858	2575	24176	57303	68107	6148	323285
44	644	8645.8	8.1704	1.3127	365	4767	2656	23965	59541	70245	8212	341308
44.5	644.5	8651.3			367	5527	2574	26280	63846	72548	8706	362140
45	645	8656.7	8.0145	1.2811	341	5179	2585	25691	59364	70381	7968	336263
45.5	645.5	8662.1			305	3751	2691	20068	50342	57619	9386	268330
46	646	8667.6	7.4022	1.3127	269	3550	3058	17237	53789	53903	9962	260145
46.5	646.5	8672.8			360	3763	2621	19078	56167	57367	9335	281524

Table S2. Raw magnetic susceptibility (MS), density, and X-ray fluorescence (XRF) data. (cont.)

Depth in core (cm)	Composite Depth in Core (cm)	Calibrated Age (cal yr BP)	MS (SI)	Density (g/cm^3)	Al (cps)	Si (cps)	S (cps)	K (cps)	Ca (cps)	Ti (cps)	Mn (cps)	Fe (cps)
47	647	8678.1	7.4246	1.2347	242	3378	2819	17006	50413	51281	8203	249188
47.5	647.5	8683.4			329	3716	2874	17954	55190	54346	7608	257499
48	648	8688.9	7.1824	1.2381	307	4698	2905	21488	57915	61591	7301	310931
48.5	648.5	8694.2			418	5065	2580	23176	60850	68444	8127	324581
49	649	8699.6	7.1755	1.2392	406	4506	2693	20922	57009	64354	8926	310388
49.5	649.5	8704.9			349	4530	2747	19968	55649	59143	9587	288277
50	650	8710.3	7.1511	1.2947	342	4929	2910	22812	61009	69489	9094	349440
50.5	650.5	8713.4			358	4963	2994	23106	57187	69950	7948	336824
51	651	8716.5	7.2731	1.2856	384	5183	2417	25474	56990	73168	7888	333497
51.5	651.5	8719.5			392	5160	2820	25635	52465	69925	7973	323381
52	652	8722.7	6.9789	1.3267	335	4445	3023	21923	53440	60113	10136	285915
52.5	652.5	8725.6			375	3606	3744	17613	49038	51577	10067	255239
53	653	8728.8	6.8072	1.2928	367	4238	2903	21398	48169	60165	8551	290726
53.5	653.5	8732			245	3121	3129	15281	47923	48557	9046	243349
54	654	8735.1	6.7201	1.255	350	4407	3029	21386	52705	66355	7968	337829
54.5	654.5	8738.3			359	5398	2375	25628	50689	73681	6530	357703
55	655	8741.3	6.6577	1.2392	384	5567	2221	25209	52626	72949	6854	357673
55.5	655.5	8744.5			313	3581	3614	16520	46240	51682	8159	317898
56	656	8747.5	6.3051	1.3231	328	3137	3503	13960	51620	46985	9355	237839
56.5	656.5	8750.6			279	4333	3271	20594	50688	61135	7302	318342
57	657	8753.5	6.5423	1.3031	389	4656	2961	23524	44766	66059	8420	332795
57.5	657.5	8756.6			424	5599	2464	27163	51223	74022	7702	347022
58	658	8759.7	7.0225	1.2662	493	6043	2030	28546	55550	76543	6973	367166
58.5	658.5	8762.8			467	6312	2579	31275	53718	81299	5261	380063
59	659	8765.8	7.2018	1.3366	421	5520	3117	27958	54883	79997	7249	350457
59.5	659.5	8768.9			432	5950	1987	27590	55730	76691	6291	370197
60	660	8772	7.6327	1.3812	374	5826	2091	27386	59028	76153	7626	369366
60.5	660.5	8775.1			416	5604	2134	25611	57918	73178	8389	356707
61	661	8778.2	8.4652	1.3537	397	5990	2149	25468	58357	73392	7970	377487
61.5	661.5	8781.3			475	5663	2198	24514	57093	72430	7780	370469

Table S2. Raw magnetic susceptibility (MS), density, and X-ray fluorescence (XRF) data. (cont.)

Depth in core (cm)	Composite Depth in Core (cm)	Calibrated Age (cal yr BP)	MS (SI)	Density (g/cm^3)	Al (cps)	Si (cps)	S (cps)	K (cps)	Ca (cps)	Ti (cps)	Mn (cps)	Fe (cps)
62	662	8784.3	9.112	1.3481	391	5319	2724	23424	55789	71534	7273	367236
62.5	662.5	8787.5			359	5680	2054	25267	60468	72489	7868	368465
63	663	8790.5	10.307	1.2986	386	5529	2353	22784	60661	69432	8872	375282
63.5	663.5	8793.7			332	4423	3108	18384	60650	54751	9324	294464
64	664	8796.9	10.832	1.3626	394	5108	2741	21888	58491	63765	8587	355756
64.5	664.5	8799.9			366	5514	2170	23846	58876	67089	8050	369452
65	665	8803.1	13.114	1.2443	406	5997	2202	26023	61532	71434	7450	394391
65.5	665.5	8806.2			406	5617	2252	24280	63128	71602	9452	386959
66	666	8809.2	13.354	1.3317	328	5085	2826	21365	55563	65207	7464	343550
66.5	666.5	8812			316	3945	2903	17261	58075	51991	10511	279239
67	667	8815	14.436	1.3082	364	4631	2801	18535	61068	55991	10419	285855
67.5	667.5	8818.1			348	5300	2432	24283	56578	65923	7944	368424
68	668	8821.2	15.538	1.2921	404	5221	3364	22849	49613	65141	8622	398071
68.5	668.5	8824.3			414	4930	2925	22835	45773	62901	10174	383343
69	669	8827.3	17.103	1.2971	382	4868	2669	23082	46367	64190	9105	387073
69.5	669.5	8830.3			391	5120	2638	23437	49931	66561	9810	402974
70	670	8833.4	19.969	1.2808	345	5359	2971	25008	51923	70495	9832	427972
70.5	670.5	8836.4			386	5593	2494	25217	53888	69569	8607	431703
71	671	8839.3	23.234	1.2981	376	5349	2774	22983	56738	67571	9989	433721
71.5	671.5	8842.5			412	5025	2682	21972	55080	62661	10834	430087
72	672	8845.5	27.305	1.2926	355	4147	2868	19915	46513	57382	10492	403091
72.5	672.5	8848.5			329	3728	2881	17610	41412	48510	11708	328313
73	673	8851.6	31.398	1.2321	277	3298	3572	16001	40598	46660	11962	310995
73.5	673.5	8854.6			297	3927	3059	18102	44964	52775	12325	363772
74	674	8857.7	34.077	1.1406	352	4459	4033	21103	49482	60531	12434	462845
74.5	674.5	8860.8			361	3973	3515	18952	45111	54227	9225	377933
75	675	8863.8	30.175	1.1757	331	4141	2863	18223	49448	49438	9400	312953
75.5	675.5	8867			327	4195	3043	19632	47177	54603	8479	347015
76	676	8869.9	25.926	1.1563	357	4082	2793	19453	50101	55525	9081	345565
76.5	676.5	8872.7			400	4517	2267	21103	43203	59934	9571	357342

Table S2. Raw magnetic susceptibility (MS), density, and X-ray fluorescence (XRF) data. (cont.)

Depth in core (cm)	Composite Depth in Core (cm)	Calibrated Age (cal yr BP)	MS (SI)	Density (g/cm^3)	Al (cps)	Si (cps)	S (cps)	K (cps)	Ca (cps)	Ti (cps)	Mn (cps)	Fe (cps)
77	677	8875.7	20.685	1.17	353	4694	2376	21722	43740	62834	10057	366901
77.5	677.5	8878.8			385	4457	2780	20255	45851	63349	9601	361805
78	678	8881.6	15.994	1.2552	339	4603	2984	21201	46243	60798	9978	366149
78.5	678.5	8884.6			383	4434	3179	20667	46867	60002	11390	357236
79	679	8887.6	13.688	1.2591	360	4606	3014	22073	44303	61377	9805	352315
79.5	679.5	8890.6			378	4109	3409	19788	43669	57538	11158	331648
80	680	8893.6	12.653	1.2462	402	4587	2959	22260	45915	63291	7757	355185
80.5	680.5	8896.6			366	3931	3092	19425	44024	57414	8750	312435
81	681	8899.4	10.864	1.2404	256	3318	3343	15618	39859	48172	8163	269921
81.5	681.5	8902.5			378	4111	2737	19201	43540	55821	7595	300832
82	682	8905.5	9.5248	1.2223	319	3748	3027	17915	41994	51964	8296	272613
82.5	682.5	8908.6			322	4121	3186	19895	48826	59498	7627	312200
83	683	8911.6	8.246	1.234	359	4569	2635	21033	46056	60164	9032	309866
83.5	683.5	8914.6			313	3894	3016	18500	43165	55045	8160	286940
84	684	8917.7	7.2163	1.2576	259	3402	3222	17553	43585	54194	8124	285219
84.5	684.5	8920.9			244	3542	3773	17686	42196	51192	8696	273215
85	685	8924.1	6.9066	1.2211	288	3200	3375	15721	40767	46514	9110	252493
85.5	685.5	8927.1			230	1954	3927	9554	32587	30453	11588	169405
86	686	8930.2	6.8608	1.2026	360	4407	3157	19862	49006	56541	7971	327981
86.5	686.5	8933.2			333	4123	3156	18166	52203	55116	10362	284299
87	687	8936.3	6.8623	1.2156	393	4495	3135	20337	49076	58760	8230	331545
87.5	687.5	8939.4			269	4040	4566	17938	51076	51345	8335	343827
88	688	8942.5	7.1343	1.2464	306	2588	6124	11308	37837	35193	9039	257319
88.5	688.5	8945.5			334	4620	3887	20891	60669	64340	8046	357931
89	689	8948.6	8.061	1.2168	324	4464	3216	20549	62021	64534	8706	346719
89.5	689.5	8951.7			325	5032	3420	22695	66236	69109	8025	378826
90	690	8954.8	8.7187	1.2828	392	5376	2840	24001	67419	69564	7270	389797
90.5	690.5	8958			332	5591	2696	24451	68979	69925	7943	393549
91	691	8961.2	9.5696	1.3411	336	5327	2847	23234	67642	68414	8010	397109

Table S2. Raw magnetic susceptibility (MS), density, and X-ray fluorescence (XRF) data. (cont.)

Depth in core (cm)	Composite Depth in Core (cm)	Calibrated Age (cal yr BP)	MS (SI)	Density (g/cm^3)	Al (cps)	Si (cps)	S (cps)	K (cps)	Ca (cps)	Ti (cps)	Mn (cps)	Fe (cps)
91.5	691.5	8964.4			413	5211	3050	23662	69044	70413	9289	415133
92	692	8967.7	10.675	1.3568	401	5631	2506	25045	65683	68570	8349	391781
92.5	692.5	8971.1			374	5385	2446	23935	65066	70726	9428	386951
93	693	8974.4	11.71	1.3151	415	5621	2118	25063	65114	68929	7769	385071
93.5	693.5	8977.7			370	4933	3810	21317	60093	62424	9814	391139
94	694	8981.2	12.283	1.2911	417	4814	2353	22851	56122	63075	8001	377662
94.5	694.5	8984.4			313	4781	2620	21965	54360	60232	8808	365202
95	695	8987.8	12.932	1.2689	320	4763	2605	22074	58343	62489	8703	364846
95.5	695.5	8991.2			284	4108	2948	19301	59419	58495	8792	350999
96	696	8994.8	13.424	1.2634	209	1529	2862	7267	55579	24665	14449	127721
96.5	696.5	8998.3			334	4483	2732	19849	62334	55795	9398	344082
97	697	9001.9	14.122	1.2593	320	4169	3335	19264	54874	59040	9337	374835
97.5	697.5	9005.5			246	3271	4400	15596	50087	48543	10652	349665
98	698	9009	14.7	1.2784	362	4107	3258	20055	62427	56759	10498	404530
98.5	698.5	9012.5			294	4232	3624	17838	55453	52425	9906	368654
99	699	9016.1	15.261	1.2555	360	4226	2498	19310	53459	56079	7824	349722
99.5	699.5	9019.8			341	3945	2613	16568	52209	52906	10547	297152
0	700	9023.4			326	5157	3324	23698	54721	64840	6119	362461
0.5	700.5	9027			315	4475	2903	20642	49915	58633	7636	375144
1	701	9030.6	33.217		275	3166	3908	15274	49813	46116	9521	302546
1.5	701.5	9034.2			225	1684	4218	7418	36705	24839	13448	128505
2	702	9037.8	18.52		220	3671	3789	16918	52774	49403	9464	342629
2.5	702.5	9041.4			326	4350	3808	20636	51900	59607	7575	380895
3	703	9045	12.646	1.2686	363	3993	3678	17908	52457	53485	9353	338240
3.5	703.5	9048.5			262	2189	5551	9506	40129	27607	10915	233861
4	704	9052.1	12.937	1.2259	265	2376	8285	9849	44224	29169	10132	301997
4.5	704.5	9055.5			276	2382	10209	10084	52515	30504	8837	294507
5	705	9059.1	12.739	1.1873	309	2313	8155	9347	39264	24536	8918	247909
5.5	705.5	9062.8			246	1679	4630	7594	34713	23489	9195	193121

Table S2. Raw magnetic susceptibility (MS), density, and X-ray fluorescence (XRF) data. (cont.)

Depth in core (cm)	Composite Depth in Core (cm)	Calibrated Age (cal yr BP)	MS (SI)	Density (g/cm^3)	Al (cps)	Si (cps)	S (cps)	K (cps)	Ca (cps)	Ti (cps)	Mn (cps)	Fe (cps)
6	706	9066.5	13.107	1.0771	219	1137	4569	5250	37226	17687	12276	99964
6.5	706.5	9070.1			234	2234	5808	8985	26099	24149	11995	150440
7	707	9073.7	13.038	1.0477	311	3985	5309	19252	44879	53955	9034	394980
7.5	707.5	9077.4			238	3836	6056	18404	42130	55618	7340	404495
8	708	9081.1	12.013	1.1446	320	4307	3791	20184	44030	57940	7102	390366
8.5	708.5	9084.7			322	4402	3382	19475	45379	59596	9787	378387
9	709	9088.2	11.536	1.2237	345	4126	4785	18698	42687	56376	7654	400010
9.5	709.5	9091.9			280	4183	3821	19416	44063	56553	7606	376580
10	710	9095.5	11.324	1.2629	322	4276	2869	19919	48901	59995	8213	362033
10.5	710.5	9099.1			308	4575	2894	20893	48672	58945	8674	379102
11	711	9102.5	11.176	1.2796	322	4191	3135	19222	44902	56440	8263	356679
11.5	711.5	9106.2			275	2835	3436	13203	46072	39031	11174	239992
12	712	9109.6	12.013	1.1752	296	4058	5646	20061	40973	54777	6962	389856
12.5	712.5	9113.2			351	4117	3068	21012	39763	58058	6724	331590
13	713	9117	11.187	1.2128	271	2692	4784	13862	43801	43746	9659	296911
13.5	713.5	9120.5			232	2615	3358	13694	43381	43093	10316	266584
14	714	9124	10.268	1.2588	323	3421	3107	17499	37086	49058	7590	304987
14.5	714.5	9127.6			313	3442	2940	16846	37178	49471	8777	292452
15	715	9131.3	9.9084	1.1842	302	2686	3205	13919	40052	43405	10992	265513
15.5	715.5	9134.8			252	3312	3278	16427	36882	47239	9288	293250
16	716	9138.4	9.1153	1.2068	282	3622	2868	17670	38194	49305	8880	289685
16.5	716.5	9142.1			312	3648	2792	17189	40227	52146	8258	295811
17	717	9145.7	9.2838	1.1553	312	3359	3756	15571	46856	48353	9395	302672
17.5	717.5	9149.3			215	2557	8838	12307	34053	35924	8957	355383
18	718	9153	9.1587	1.2111	301	3777	5798	17454	44404	50760	10727	390443
18.5	718.5	9156.7			296	3612	3543	17350	47166	53067	10316	378860
19	719	9160.3	10.229	1.165	272	3209	2836	15144	45588	47423	10298	349911
19.5	719.5	9164			295	3259	2963	15201	41365	45021	11090	330730
20	720	9167.5	10.471	1.2519	267	3157	3746	15304	50703	45872	7605	311122

Table S2. Raw magnetic susceptibility (MS), density, and X-ray fluorescence (XRF) data. (cont.)

Depth in core (cm)	Composite Depth in Core (cm)	Calibrated Age (cal yr BP)	MS (SI)	Density (g/cm^3)	Al (cps)	Si (cps)	S (cps)	K (cps)	Ca (cps)	Ti (cps)	Mn (cps)	Fe (cps)
20.5	720.5	9171.2			188	1469	2541	7972	54239	30407	11061	163083
21	721	9175	11.572	1.2121	300	3569	2640	15566	50766	47835	9795	268453
21.5	721.5	9178.6			319	3998	2499	17754	49971	53370	8733	282822
22	722	9182.3	11.123	1.2033	239	2127	2315	10340	49511	37939	10842	167892
22.5	722.5	9186.1			222	1699	2891	8822	55442	36181	9934	212140
23	723	9189.7	9.1178	1.2266	211	1667	3442	7771	52855	29737	9890	180135
23.5	723.5	9193.4			286	2508	4236	11996	47658	39802	9835	244134
24	724	9197.1	7.7932	1.1645	289	3794	3098	16970	48489	51484	8250	283262
24.5	724.5	9200.7			353	4785	2654	19794	49299	60256	6791	303704
25	725	9204.5	6.2849	1.2106	404	5028	2386	21091	49870	63422	8227	308671
25.5	725.5	9208			308	4172	3230	17618	45207	53793	6856	289112
26	726	9211.5	5.5704	1.2014	350	4649	2512	20056	48796	58906	6778	317739
26.5	726.5	9215.1			267	3471	2796	15930	45710	52073	8559	275985
27	727	9218.6	5.2643	1.219	356	4331	2092	18285	48561	57576	6879	291694
27.5	727.5	9222.2			321	4256	2117	16898	52743	56524	8671	290289
28	728	9225.9	5.1199	1.2175	325	4749	1890	18891	50181	58401	7151	290903
28.5	728.5	9229.4			459	4800	2299	19943	51797	58942	7129	318406
29	729	9233.1	5.1309	1.2328	312	4082	2602	16543	48652	54967	6815	267746
29.5	729.5	9236.6			401	4714	2690	18808	53705	59478	7550	315439
30	730	9240.2	5.1623	1.2431	377	3596	2593	16243	52218	54642	6643	268454
30.5	730.5	9243.9			252	2262	2846	11333	52220	40503	9772	191445
31	731	9247.6	5.0673	1.2302	234	1572	5589	8314	49396	29452	8699	208398
31.5	731.5	9251.1			185	980	3519	5668	49559	21230	10553	137907
32	732	9254.7	4.8758	1.1845	205	382	3579	1857	44480	7839	12546	79628
32.5	732.5	9258.4			224	990	3207	4327	35774	13900	11989	84316
33	733	9261.9	4.6481	1.1044	244	2427	2860	12827	45342	43221	7276	225009
33.5	733.5	9265.6			278	1561	3426	9018	46113	35671	10910	212828
34	734	9269.1	4.1486	1.0827	320	2650	2510	12540	41314	43109	10774	224011
34.5	734.5	9272.8			299	3562	2464	16700	36708	48484	9289	242882

Table S2. Raw magnetic susceptibility (MS), density, and X-ray fluorescence (XRF) data. (cont.)

Depth in core (cm)	Composite Depth in Core (cm)	Calibrated Age (cal yr BP)	MS (SI)	Density (g/cm^3)	Al (cps)	Si (cps)	S (cps)	K (cps)	Ca (cps)	Ti (cps)	Mn (cps)	Fe (cps)
35	735	9276.4	3.7286	1.1555	256	1838	3134	9706	43532	29755	9562	169377
35.5	735.5	9280.1			198	1332	3689	6060	46757	15594	12473	131755
36	736	9283.7	3.5101	1.2014	202	582	5259	2985	42164	8008	11519	139577
36.5	736.5	9287.4			251	1306	4556	7558	46416	23539	11093	183917
37	737	9291.1	3.7405	1.1274	302	2204	2960	12422	41657	37442	9301	203196
37.5	737.5	9294.7			229	1896	2115	11045	39143	33235	9932	168320
38	738	9298.3	3.7689	1.0945	307	2179	2065	10762	39478	32239	11511	136167
38.5	738.5	9302			309	3945	2722	19297	36877	52269	8914	246438
39	739	9305.6	3.9097	1.1255	335	3832	3478	20777	38350	56347	7014	291423
39.5	739.5	9309.3			350	3846	3321	19965	38558	59103	8095	275789
40	740	9312.8	4.4254	1.16	332	4577	2670	23536	34472	62448	8450	300295
40.5	740.5	9318.1			346	4442	5390	23140	42852	66123	6931	373049
41	741	9323.1	5.1623	1.2075	444	6461	2084	30099	49952	78044	6440	377020
41.5	741.5	9328.2			421	6033	2852	27692	54321	74424	6559	397318
42	742	9333.2	5.9838	1.2409	312	5404	9591	25172	49533	68260	5953	486372
42.5	742.5	9338.3			411	6069	8503	26649	53192	69232	6259	455306
43	743	9343.3	6.4832	1.3433	430	6087	2281	26204	60718	71172	7374	394988
43.5	743.5	9348.3			360	5674	4212	24436	57350	69408	6421	388949
44	744	9353.3	7.2222	1.3455	389	5557	3139	26798	50874	69598	6695	358152
44.5	744.5	9358.3			401	5821	1956	28544	50364	73553	8176	355548
45	745	9363.3	7.6819	1.3604	352	5400	5900	26544	49748	66845	6865	440032
45.5	745.5	9368.5			351	5403	5726	25871	52545	69267	6202	411145
46	746	9373.5	8.0412	1.3452	420	5349	4024	28953	49713	75658	7353	381218
46.5	746.5	9378.5			424	4957	5195	26754	50505	69610	7176	404615
47	747	9383.7	8.423	1.306	334	4910	6186	26119	47769	68719	7474	405977
47.5	747.5	9388.8			380	5638	4023	26546	51795	70418	7591	431595
48	748	9394	8.5461	1.3087	361	5344	2271	22716	60603	67169	9349	420806
48.5	748.5	9399			307	4566	2326	19132	57570	59145	9211	371240
49	749	9404.1	9.0377	1.2983	334	4669	2995	21681	55941	61549	9399	390591

Table S2. Raw magnetic susceptibility (MS), density, and X-ray fluorescence (XRF) data. (cont.)

Depth in core (cm)	Composite Depth in Core (cm)	Calibrated Age (cal yr BP)	MS (SI)	Density (g/cm^3)	Al (cps)	Si (cps)	S (cps)	K (cps)	Ca (cps)	Ti (cps)	Mn (cps)	Fe (cps)
49.5	749.5	9409.1			357	4962	2659	23891	53503	65209	8028	403536
50	750	9414.4	9.4816	1.3149	319	4238	3178	21698	56545	63076	8015	376047
50.5	750.5	9419.4			358	5305	1978	26252	56833	70138	8425	420768
51	751	9424.5	10.078	1.2825	454	5087	1654	25836	52891	72079	6811	390942
51.5	751.5	9429.5			408	4931	1983	27824	41744	74251	6847	364329
52	752	9434.5	10.08	1.2914	300	3060	2472	16510	48051	53452	9469	299560
52.5	752.5	9439.3			329	3773	2338	21039	41418	57021	8365	330619
53	753	9444.4	9.5247	1.2897	294	3337	2555	18321	46334	49694	9950	346611
53.5	753.5	9449.4			207	757	1682	5264	46577	19501	12743	107544
54	754	9454.4	8.7237	1.219	259	2045	2723	11796	41408	36783	10232	233213
54.5	754.5	9459.3			314	2766	4153	15458	32876	41438	8509	309540
55	755	9464.2	7.1662	1.1769	284	1949	2913	12237	39205	38659	9319	227098
55.5	755.5	9469.4			277	2239	3205	13206	32569	40077	8887	261361
56	756	9474.4	5.9347	1.1276	335	3442	2808	19201	29676	49968	8503	304216
56.5	756.5	9479.5			354	3818	2809	20036	27726	50036	8081	321697
57	757	9484.7	5.0436	1.1269	207	1579	1869	9240	32179	28250	9523	162085
57.5	757.5	9489.9			193	513	2376	2936	31850	11245	14358	56627
58	758	9494.9	4.5462	1.1494	304	3095	3150	16551	32460	46427	8061	267481
58.5	758.5	9500.1			407	4721	2291	25251	26393	64060	5937	361986
59	759	9505.1	4.8963	1.0672	326	3313	2235	19187	23807	53663	6923	290591
59.5	759.5	9510.4			355	3528	2606	19504	24451	53975	6257	310080
60	760	9515.6	4.6048	1.1945	369	3534	2943	19038	25637	52148	6761	299746
60.5	760.5				305	3651	2686	20598	25775	56052	6304	318424
61	761		4.5679	1.2443	355	4822	3321	23913	30767	63619	6967	355024

REFERENCES

Asmerom, Y., Baldini, J. U. L., Prufer, K. M., Polyak, V. J., Ridley, H. E., Aquino, V. V., Baldini, L. M., Breitenbach, S. F. M., Macpherson, C. G., and Kennett, D. J., 2020, Intertropical convergence zone variability in the Neotropics during the Common Era: Science Advances, v. 6, no. 7, p. 1 - 7. https://doi.org/10.1126/sciadv.aax3644

Balascio, N. L., Zhang, Z., Bradley, R. S., Perren, B., Dahl, S. O., and Bakke, J., 2011, A multi-proxy approach to assessing isolation basin stratigraphy from the Lofoten Islands, Norway: Quaternary Research, v. 75, no. 1, p. 288-300. https://doi.org/10.1016/j.yqres.2010.08.012

Bhattacharya, T., Chiang, J. C. H., and Cheng, W., 2017, Ocean-atmosphere dynamics linked to 800–1050 CE drying in mesoamerica: Quaternary Science Reviews, v. 169, p. 263-277. https://doi.org/10.1016/j.quascirev.2017.06.005

Blaauw, M., and Christen, J. A., 2011, Flexible paleoclimate age-depth models using an autoregressive gamma process: Bayesian Analysis, v. 6, no. 3, p. 457-474. doi:10.1214/11-BA618. https://projecteuclid.org/euclid.ba/1339616472

Brinson, M. M., and Nordlie, F. G., 1975, II. Lakes. 8. Central and South America: Lake Izabal, Guatemala: SIL Proceedings, 1922-2010 Internationale Vereinigung für Theoretische und Angewandte Limnologie: Verhandlungen, v. 19, no. 2, p. 1468-1479. https://doi.org/10.1080/03680770.1974.11896206

Chadee, X. T., and Clarke, R. M., 2014, Large-scale wind energy potential of the Caribbean region using near-surface reanalysis data: Renewable and Sustainable Energy Reviews, v. 30, p. 45-58. https://doi.org/10.1016/j.rser.2013.09.018

Correa-Metrio, A., Bush, M. B., Cabrera, K. R., Sully, S., Brenner, M., Hodell, D. A., Escobar, J., and Guilderson, T., 2012, Rapid climate change and no-analog vegetation in lowland Central America during the last 86,000 years: Quaternary Science Reviews, v. 38, p. 63-75. https://doi.org/10.1016/j.quascirev.2012.01.025

Curtis, J. H., Hodell, D. A., and Brenner, M., 1996, Climate variability on the Yucatan Peninsula (Mexico) during the past 3500 years, and implications for Maya cultural evolution: Quaternary Research, v. 46, no. 1, p. 37-47. https://doi.org/10.1006/qres.1996.0042

Deevey, E. S., 1965, Sampling lake sediments by use of the Livingstone sampler, in Kummel, B., and Raup, D., eds., Handbook of Paleontological Techniques Freeman, p. 521-529. https://doi.org/10.1002/gj.3350050122

Fensterer, C., Scholz, D., Hoffmann, D. L., Spötl, C., Schröder-Ritzrau, A., Horn, C., Pajón, J. M., and Mangini, A., 2013, Millennial-scale climate variability during the last 12.5ka recorded in a Caribbean speleothem: Earth and Planetary Science Letters, v. 361, p. 143-151. https://doi.org/10.1016/j.epsl.2012.11.019

Fick, S. E., and Hijmans, R. J., 2017, WorldClim 2: new 1-km spatial resolution climate surfaces for global land areas: International journal of climatology, v. 37, no. 12, p. 4302-4315. https://doi.org/10.1002/joc.5086

Fisher, M. M., Brenner, M., and Reddy, K. R., 1992, A simple, inexpensive piston corer for collecting undisturbed sediment/water interface profiles: Journal of Paleolimnology, v. 7, no. 2, p. 157-161. https://doi.org/10.1007/BF00196870

Good, P., Chadwick, R., Holloway, C. E., Kennedy, J., Lowe, J. A., Roehrig, R., and Rushley, S. S., 2021, High sensitivity of tropical precipitation to local sea surface temperature: Nature, v. 589, no. 7842, p. 408-414. https://doi.org/10.1038/s41586-020-2887-3

Gregory, B. R. B., Peros, M., Reinhardt, E. G., and Donnelly, J. P., 2015, Middle–late Holocene Caribbean aridity inferred from foraminifera and elemental data in sediment cores from two Cuban lagoons: Palaeogeography, Palaeoclimatology, Palaeoecology, v. 426, p. 229-241. https://doi.org/10.1016/j.palaeo.2015.02.029

Harris, I., Jones, P. D., Osborn, T. J., and Lister, D. H., 2014, Updated high-resolution grids of monthly climatic observations–the CRU TS3. 10 Dataset: International journal of climatology, v. 34, no. 3, p. 623-642. https://doi.org/10.1002/joc.3711

Haug, G. H., Hughen, K. A., Sigman, D. M., Peterson, L. C., and Röhl, U., 2001, Southward migration of the Intertropical Convergence Zone through the Holocene: Science, v. 293, no. 5533, p. 1304-1308. https://doi.org/10.1126/science.1059725

Hillesheim, M. B., Hodell, D. A., Leyden, B. W., Brenner, M., Curtis, J. H., Anselmetti, F. S., Ariztegui, D., Buck, D. G., Guilderson, T. P., and Rosenmeier, M. F., 2005, Climate change in lowland Central America during the late deglacial and early Holocene: Journal of Quaternary Science, v. 20, no. 4, p. 363-376. https://doi.org/10.1002/jqs.924

Hirahara, S., Ishii, M., and Fukuda, Y., 2014, Centennial-scale sea surface temperature analysis and its uncertainty: Journal of Climate, v. 27, no. 1, p. 57-75. https://doi.org/10.1175/JCLI-D-12-00837.1

Hodell, D. A., Brenner, M., Curtis, J. H., and Guilderson, T., 2001, Solar forcing of drought frequency in the Maya lowlands: Science, v. 292, no. 5520, p. 1367-1370. https://doi.org/10.1126/science.1057759

Hodell, D. A., Curtis, J. H., and Brenner, M., 1995, Possible role of climate in the collapse of Classic Maya civilization: Nature, v. 375, no. 6530, p. 391. https://doi.org/10.1038/375391a0

Hodell, D. A., Curtis, J. H., Jones, G. A., Higuera-Gundy, A., Brenner, M., Binford, M. W., and Dorsey, K. T., 1991, Reconstruction of Caribbean climate change over the past 10,500 years: Nature, v. 352, no. 6338, p. 790. https://doi.org/10.1038/352790a0

Horn, C., 2011, Spatial variations of the phase shift between ocean surface warming, evaporation and changes of continental ice volume at Termination I. [Ph.D. thesis]. University of Kiel, 172 p.

INSIVUMEH, 2020, National Institute of Seismology, Vulcanology, and Meteorology of Guatemala. http://historico.insivumeh.gob.gt/hidrologia-2/ (accessed 23 May 2020).

Jolliffe, I., 1986, Principal Component Analysis. 2nd Edition. Springer-Verlag, New York, p. 487. https://doi.org/10.1007/b98835

Kennett, D. J., Breitenbach, S. F., Aquino, V. V., Asmerom, Y., Awe, J., Baldini, J. U., Bartlein, P., Culleton, B. J., Ebert, C., and Jazwa, C., 2012, Development and disintegration of Maya political systems in response to climate change: Science, v. 338, no. 6108, p. 788-791. https://doi.org/10.1126/science.1226299

Koutavas, A., deMenocal, P. B., Olive, G. C., and Lynch-Stieglitz, J., 2006, Mid-Holocene El Niño–Southern Oscillation (ENSO) attenuation revealed by individual foraminifera in eastern tropical Pacific sediments: Geology, v. 34, no. 12, p. 993-996. https://doi.org/10.1130/G22810A.1

Kylander, M. E., Ampel, L., Wohlfarth, B., and Veres, D., 2011, High-resolution X-Ray fluorescence core scanning analysis of Les Echets (France) sedimentary sequence: New insights from chemical proxies: Journal of Quaternary Science, v. 26, no. 1, p. 109-117. https://doi.org/10.1002/jqs.1438

Laskar, J., Robutel, P., Joutel, F., Gastineau, M., Correia, A. C. M., and Levrard, B., 2004, A long-term numerical solution for the insolation quantities of the Earth: A&A, v. 428, no. 1, p. 261-285. https://doi.org/10.1051/0004-6361:20041335

Leyden, B. W., 2002, Pollen evidence for climatic variability and cultural disturbance in the Maya lowlands: Ancient Mesoamerica, v. 13, no. 1, p. 85-101. https://doi.org/10.1017/S0956536102131099

Martinez, C., Goddard, L., Kushnir, Y., and Ting, M., 2019, Seasonal climatology and dynamical mechanisms of rainfall in the Caribbean: Climate Dynamics, v. 53, no. 1, p. 825-846. https://doi.org/10.1007/s00382-019-04616-4

Mueller, A. D., Islebe, G. A., Hillesheim, M. B., Grzesik, D. A., Anselmetti, F. S., Ariztegui, D., Brenner, M., Curtis, J. H., Hodell, D. A., and Venz, K. A., 2009, Climate drying and associated forest decline in the lowlands of northern Guatemala during the late Holocene: Quaternary Research, v. 71, no. 2, p. 133-141. https://doi.org/10.1016/j.yqres.2008.10.002

Muñoz, E., Busalacchi, A. J., Nigam, S., and Ruiz-Barradas, A., 2008, Winter and Summer Structure of the Caribbean Low-Level Jet: Journal of Climate, v. 21, no. 6, p. 1260-1276. https://doi.org/10.1175/2007JCLI1855.1

Nowaczyk, N. R., Melles, M., and Minyuk, P., 2007, A revised age model for core PG1351 from Lake El'gygytgyn, Chukotka, based on magnetic susceptibility variations tuned to northern hemisphere insolation variations: Journal of Paleolimnology, v. 37, no. 1, p. 65-76. https://doi.org/10.1007/s10933-006-9023-8

Obrist-Farner, J., Brenner, M., Curtis, J. H., Kenney, W., and Salvinelli, C., 2019, Recent onset of eutrophication in Lake Izabal, the largest water body in Guatemala: Journal of Paleolimnology, v. 62, p. 359-372. https://doi.org/10.1007/s10933-019-00091-3

Obrist-Farner, J., Eckert, A., Locmelis, M., Crowley, J. L., Mota-Vidaure, B., Lodolo, E., Rosenfeld, J., and Duarte, E., 2020, The role of the Polochic Fault as part of the North American and Caribbean Plate boundary: Insights from the infill of the Lake Izabal Basin: Basin Research, v. 32, no. 6, p. 1347-1364. https://doi.org/10.1111/bre.12431

Oksanen, J., Blanchet, F., Friendly, M., Kindt, R., Legendre, P., McGlinn, D., Minchin, P., O'Hara, R., Simpson, G., and Solymos, P., 2019, vegan: Community Ecology Package. R package version 2.5. 4. 2019. https://github.com/vegandevs/vegan

Ortiz, J., and Jaramillo, C., 2018, SDAR: A Toolkit for Stratigraphic Data Analysis in R, Smithsonian Research Online. https://doi.org/10.25570/stri/10088/35917

Reimer, P. J., Austin, W. E. N., Bard, E., Bayliss, A., Blackwell, P. G., Bronk Ramsey, C., Butzin, M., Cheng, H., Edwards, R. L., Friedrich, M., Grootes, P. M., Guilderson, T. P., Hajdas, I., Heaton, T. J., Hogg, A. G., Hughen, K. A., Kromer, B., Manning, S. W., Muscheler, R., Palmer, J. G., Pearson, C., van der Plicht, J., Reimer, R. W., Richards, D. A., Scott, E. M., Southon, J. R., Turney, C. S. M., Wacker, L., Adolphi, F., Büntgen, U., Capano, M., Fahrni, S. M., Fogtmann-Schulz, A., Friedrich, R., Köhler, P., Kudsk, S., Miyake, F., Olsen, J., 2020, The IntCal20 Northern Hemisphere Radiocarbon Age Calibration Curve (0–55 cal kBP): Radiocarbon, v. 62, no. 4, p. 725-757. https://doi.org/10.1017/RDC.2020.41

Rühlemann, C., Mulitza, S., Müller, P. J., Wefer, G., and Zahn, R., 1999, Warming of the tropical Atlantic Ocean and slowdown of thermohaline circulation during the last deglaciation: Nature, v. 402, no. 6761, p. 511-514. https://doi.org/10.1038/990069

Schmidt, M. W., Spero, H. J., and Lea, D. W., 2004, Links between salinity variation in the Caribbean and North Atlantic thermohaline circulation: Nature, v. 428, no. 6979, p. 160-163. https://doi.org/10.1038/nature02346

Schneider, U., Becker, A., Finger, P., Meyer-Christoffer, A., Rudolf, B., and Ziese, M., 2011, GPCC Full Data Reanalysis Version 6.0 at 0.5°: Monthly Land-Surface Precipitation from Rain-Gauges built on GTS-based and Historic Data: GPCC Data Rep., v. 10. https://doi.org/10.5676/dwd_gpcc/fd_m_v6_050

Stansell, N. D., Steinman, B. A., Lachniet, M. S., Feller, J., Harvey, W., Fernandez, A., Shea, C. J., Price, B., Coenen, J., Boes, M., and Perdziola, S., 2020, A lake sediment stable isotope record of late-middle to late Holocene hydroclimate variability in the western Guatemala highlands: Earth and Planetary Science Letters, v. 542, p. 116327. https://doi.org/10.1016/j.epsl.2020.116327

Tite, M. S., and Mullins, C., 1971, Enhancement of the Magnetic Susceptibility of Soils on Archaeological Sites: Archaeometry, v. 13, no. 2, p. 209-219. https://doi.org/10.1111/j.1475-4754.1971.tb00043.x

Tjallingii, R., Röhl, U., Kölling, M., and Bickert, T., 2007, Influence of the water content on X-ray fluorescence core-scanning measurements in soft marine sediments: Geochemistry, Geophysics, Geosystems, v. 8, no. 2, p. 1-12. https://doi.org/10.1029/2006GC001393

Voorhies, B., 1971, Settlement patterns in two regions of the southern Maya lowlands: American Antiquity, v. 37, no. 1, p. 115-126. https://doi.org/10.2307/278893

Wahl, D., Byrne, R., and Anderson, L., 2014, An 8700 year paleoclimate reconstruction from the southern Maya lowlands: Quaternary Science Reviews, v. 103, p. 19-25.

Wahl, D., Byrne, R., Schreiner, T., and Hansen, R., 2006, Holocene vegetation change in the northern Peten and its implications for Maya prehistory: Quaternary Research, v. 65, no. 3, p. 380-389. https://doi.org/10.1016/j.yqres.2005.10.004

Wang, C., 2007, Variability of the Caribbean Low-Level Jet and its relations to climate: Climate Dynamics, v. 29, no. 4, p. 411-422. https://doi.org/10.1007/s00382-007-0243-z

Willmott, C. J., and Matsuura, K., 2001, Terrestrial air temperature and precipitation: Monthly and annual time series (1950–1999) Version 5.0.1: Center for Climatic Research, University of Delaware, Newark. http://climate.geog.udel.edu/~climate/html_pages/README.ghcn_ts2.html.

Winter, A., Zanchettin, D., Lachniet, M., Vieten, R., Pausata, F. S., Ljungqvist, F. C., Cheng, H., Edwards, R. L., Miller, T., and Rubinetti, S., 2020, Initiation of a stable convective hydroclimatic regime in Central America circa 9000 years BP: Nature Communications, v. 11, no. 1, p. 1-8. https://doi.org/10.1038/s41467-020-14490-y

II. SEDIMENTOLOGICAL AND GEOCHEMICAL CHARACTERIZATION OF A VARVED SEDIMENT RECORD FROM THE NORTHERN NEOTROPICS

Edward Duarte[1], Jonathan Obrist-Farner[1], Susan R. H. Zimmerman [2], Erik T. Brown[3], Robert Brown[3]

[1]Geosciences and Geological and Petroleum Engineering Department, Missouri University of Science and Technology, Rolla, MO 65409, USA

[2]Center for Accelerator Mass Spectrometry, Lawrence Livermore National Laboratory, Livermore, CA 94550, USA

[3]Large Lakes Observatory and Department of Earth and Environmental Sciences, University of Minnesota Duluth, Duluth, MN 55812, USA

ABSTRACT

Highly resolved sedimentological records (e.g., varves) are well-known paleoclimate archives that can be used to calibrate key climatic and tectonic events. Most published varved records, however, are from high latitudes, resulting in a spatial bias with few annually resolved records in tropical regions (e.g., Central America). Here we report on the sedimentology of two sediment cores obtained from Lake Izabal, eastern Guatemala, that contain a well-preserved thinly laminated section spanning ca. 2,200 years. We integrate radiocarbon age-depth modeling, sedimentological observations, laminae counting, μX-ray fluorescence scanning, and multivariate statistical analyses to constrain the nature and chronology of the laminations. Our sedimentological and geochemical results suggest that this mid-Holocene sequence of alternating clastic (dark) and biogenic (light) laminae couplets, were deposited annually. Dark laminae are characterized by an abundance of detrital grains, organic detritus, total organic carbon,

and terrigenic elements and formed during times of increased discharge from rivers during the rainy season. In contrast, light laminae are characterized by a decrease in detrital grains and total organic carbon, and an increase in biogenic silica constituents and a higher abundance of silica and formed during times of increased lake productivity during the dry season. The annual character of the laminations is supported by the consistency among the number of laminae couplets and the radiocarbon age-depth models. The laminated Lake Izabal record provides one of the first annually resolved sedimentological records from Central America and it can help constrain mid-Holocene hydroclimate variability and regional tectonic processes at this understudied region.

1. INTRODUCTION

Paleolimnological investigations in Central America have highlighted the sensitivity of lake systems to past environmental and climatic changes (e.g., Leyden et al., 1994; Hodell et al., 1995; Curtis et al., 1996; Curtis et al., 1998; Hodell et al., 2001; Hillesheim et al., 2005; Mueller et al., 2009; Wahl et al., 2014; Stansell et al., 2020). For example, several hydroclimate records indicate that Central America experienced relatively wet conditions during the early and mid-Holocene, followed by gradual drying during the late Holocene (Leyden et al., 1994; Hodell et al., 1995; Mueller et al., 2009; Wahl et al., 2014). This pattern of hydroclimate variability was generally interpreted as a result of a gradual shift in the mean position of the Intertropical Convergence Zone (ITCZ; Hodell et al., 1991; Haug et al., 2001). Recent studies from the Guatemalan highlands, however, suggest that oceanic and atmospheric processes acting on much

shorter time scales significantly influenced Holocene hydroclimate in the region (Stansell et al., 2020; Winter et al., 2020). Additional highly resolved proxy records could provide key information to constrain sub-decadal and multidecadal oceanic and atmospheric processes influencing precipitation in the region, such as El Niño-Southern Oscillation (ENSO).

Highly resolved sedimentological records from lakes are common in lacustrine systems with a strong signal of seasonally alternating fluxes, in the absence of post-depositional erosion, resuspension, and re-deposition (Zolitschka et al., 2015). These conditions are commonly founded in lakes that are deep relative to their surface area (Larsen et al., 1998; Ojala et al., 2000; Tylmann et al., 2013). Central American lakes, however, are rarely deep enough to contain annually resolved laminated records (i.e., varves; cf. Brocard et al., 2014) that could offer the potential for high-resolution quantitative paleoclimatic reconstructions. Lake Izabal, located in the eastern lowlands of Guatemala, is a shallow (z = 15 m) lake with a large surface area (Fig. 1). Modern limnological observations indicate that the lake is highly sensitive to precipitation seasonality (Brinson, 1973; Brinson and Nordlie, 1975). For example, during the wet season (May to October), lake level increases a monthly average of ~45cm, and increased runoff delivers abundant terrigenous sediment and allochthonous organic detritus to the lake (Brinson, 1973). In contrast, during the dry season (November to April), decreased river input results in lower lake levels (Brinson, 1973; Brinson and Nordlie, 1975; Medina et al., 2009) and lower terrigenous sediment input, and in phytoplankton blooms (Brinson, 1973; Brinson and Nordlie, 1975). Paleolimnological studies have also illustrated that this system responds to long-term changes in nutrient input, erosion,

precipitation, and sea-level changes (Obrist-Farner et al., 2019; Duarte et al., 2021; Obrist-Farner et al., 2022).

Although Lake Izabal is currently shallow and well-mixed, a marine transgression during the early Holocene established a chemocline in the lake that most likely turned Lake Izabal into a meromictic lake, with persistent bottom-water anoxia that lasted approximately 3,200 years between 8,370 and 4,800 cal yr BP (Obrist-Farner et al., 2022). Anoxia decreased bioturbation in the deeper parts of the basin, facilitating preservation of a sequence of thinly laminated sediments (Duarte et al., 2021). Preliminary research results suggested that the laminated sediment record from Lake Izabal could be annually laminated (Buckley and Obrist-Farner, 2019). However, limited chronological constraints and difficulties in establishing correlations between overlapping cores did not allow robust evaluation of the laminations and the processes that led to their formation.

This study integrates radiocarbon age-depth modeling, smear-slide analysis, laminae counting, μX-ray fluorescence (μXRF) scanning and other geochemical analysis, and multivariate statistical analysis for two sediment cores retrieved from the deepest part of Lake Izabal (Figure 1). We analyzed a 400-cm-thick thinly laminated silty clay section that contains 2,186 dark/light laminae couplets. The dark and light laminae are sedimentological and geochemical distinct, with differences in color, thickness, grain size, composition, and biogenic and organic matter content. Our analyses suggest that the couplets are annual deposits and that their physical and compositional differences are mainly driven by precipitation seasonality, preserved during an unusual period of anoxia. The laminated sediment section retrieved from Lake Izabal provides one of the first

annually resolved sedimentological records from Central America and can help to understand regional climatic processes and tectonic events during the mid-Holocene.

2. REGIONAL SETTING

Lake Izabal is a polymictic and hydrologically open lake with a surface area of 672 km^2 and a maximum water depth of 15 m (Figure 1). The lake is located between the central highlands and eastern lowlands of Guatemala. It occupies the eastern side of the Lake Izabal Basin, a pull-apart basin that developed ~12 My ago along the North American-Caribbean plate boundary (Bartole et al., 2019; Obrist-Farner et al., 2020). The lake is bounded by the Santa Cruz Mountain Range in the north, the Minas Mountain Range in the south, and the Mico Mountains in the east (Figure 1).

Lake Izabal has a hydrological catchment area of 8,740 km^2, and the main tributary is the Polochic River, contributing ~70% of the water input to the lake (Brinson & Nordlie, 1975; Obrist-Farner et al., 2019). The water residence time in the lake is ~6 months, and the lake drains into the Caribbean Sea via the Dulce River (Brinson & Nordlie, 1975; Figure 1). Monthly precipitation in Lake Izabal is seasonal, with an annual mean of approximately 3,300 $mmyr^{-1}$ (Duarte et al., 2021). Modern observations indicate that the seasonality of precipitation has significant effects on lake level variations, lake productivity, and sediment and organic matter input into the lake (Brinson, 1973; Brinson and Nordlie, 1975; Medina et al., 2009).

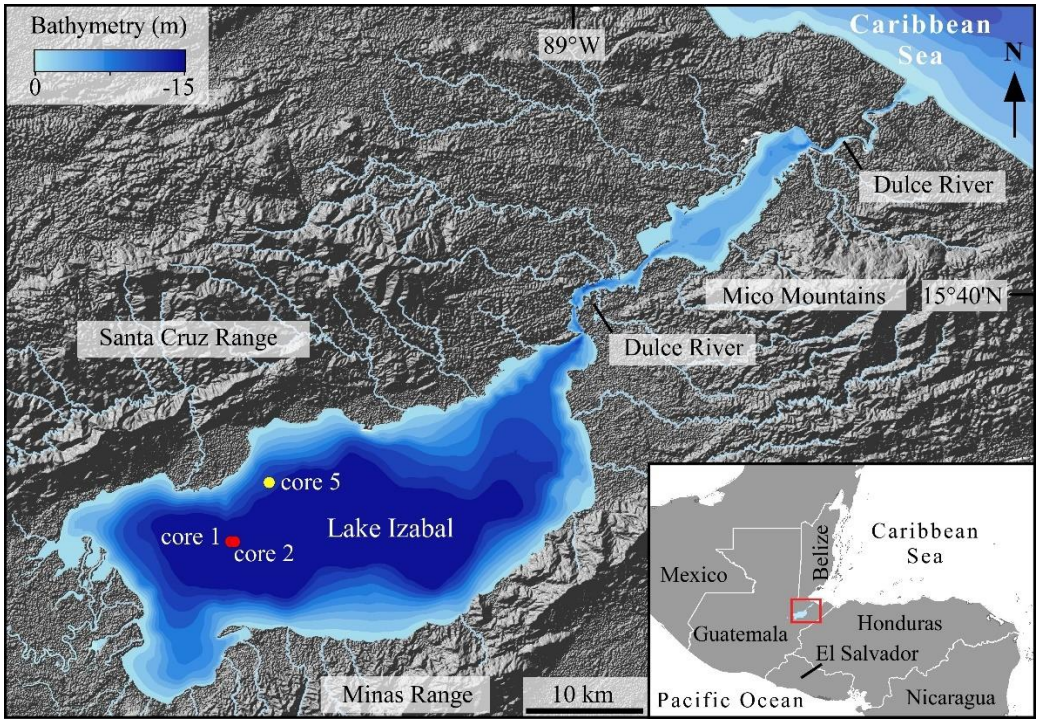

Figure 1. Location of Lake Izabal showing the bathymetry of the lake and the main topographic features. Red dots show the locations of the two sediment cores (cores 1 and 2) used in this study. Yellow dot shows the location of sediment core 5. Inset map shows the location of the study area (red square) in the eastern lowlands of Guatemala.

3. MATERIALS AND METHODS

Two parallel and overlapping sediment cores (cores 1 and 2), ~6 m apart, were retrieved in 2018 from the deepest area of Lake Izabal using a modified piston corer (Deevey, 1965). Consolidated sediment sections (individual drives of 1 m depth) were collected at 185 cm below the lake sediment surface for core 1 (15°28'47.95"N, 89°15'34.26"W) and 225 cm below the lake sediment surface for core 2 (15°28'48.08"N, 89°15'34.1"W). The sediment cores (555 cm for core 1 and 470 cm for core 2) were kept in their polycarbonate core tubes, sealed, and shipped to the University of Florida.

Magnetic susceptibility (MS) was measured at 0.5 cm resolution using a loop sensor in an automated core logger (Geotek MSCL-S). Then, sediment cores were cut lengthwise, and cleaned core surfaces were scanned at 20 pixels mm^{-1} to acquire line scan images using a Geoteck Geoscan-III at the University of Florida. The working halves of the split cores were shipped to Missouri S&T for initial core description, while the other split halves were stored at the Land Use and Environmental Change Institute (LUECI) at the University of Florida. The initial core description was carried out by visual inspection of the cleaned core surfaces and the digital core scan images following the protocol outlined by Schnurrenberger et al. (2003). We constructed a composite sediment profile via cross-correlation of the high-resolution line-scan images using Schlumberger's Techlog® 2017.2 software, using the overlapping sections to eliminate sediment intervals at the top of the core sections with evidence of disturbance caused while coring.

To characterize laminae composition and structure, we analyzed thin sections, grain size, smear slides, and carbon content from core 1. Sediment slabs from core 1 were prepared at the Continental Scientific Drilling Facility (CSDF) at the University of Minnesota Twin Cities using the freeze-drying technique. First, sediment slabs were submerged in liquid nitrogen dioxide (NO_2) and subsequently freeze-dried for four days. Slabs were then impregnated with Spurr resin. Impregnated slabs were divided, and thin sections were prepared following standard techniques. Smear slides were prepared from untreated sediment and mounted into glass slides with Norland Optical Cement 61. Percent carbon (wt% C) was measured for 20 samples using a Carlo-Erba elemental analyzer at LUECI. Samples of dried bulk sediment (3 mg per sample) were analyzed from 623.8 to 625.7 cm in the laminated interval of core 1. Grain size distribution was

measured by a laser Microtrac S3500 diffraction particle analyzer at Missouri S&T on a selection of 10 samples (n=10) of core 1. The results are reported as mean grain size (Mz) with one standard deviation (Folk and Ward, 1957).

Micro X-ray fluorescence (µXRF) core scanning was conducted on both cores at 500 µm steps. Because the laminations in the Izabal cores are, in some intervals, thinner than 500 µm, we scanned one impregnated thin section chip (from 520 to 517 cm) at 40 µm steps. The µXRF measurements were performed with an ITRAXTM core scanner at the Large Lakes Observatory at the University of Minnesota-Duluth, using a Cr X-ray source, operated at 30 kV and 55 mA and with a 15-sec dwell time. The width of the x-ray beam on the ITRAX^{TM} core scanner is 200 µm; therefore, the 40 µm resolution scan is oversampling the section chip, only exposing 40 µm of new material each step. Measured elemental abundances are reported in total counts (tc), and elemental ratios are reported on a log scale to avoid ratio asymmetry. Principal component analysis (PCA) was performed to summarize the relationship between elemental variables, where vector length indicates the amount of variance of each element and angles among vectors indicating their association (Jolliffe, 1986). Elemental counts were standardized (as z-scores) before PCA analysis to avoid confounding effects of dimensional heterogeneity.

Chronological control for both cores was established using accelerator mass spectrometry (AMS) radiocarbon (^{14}C) ages of five terrestrial plant fragments. Samples were pretreated with standard acid-base-acid chemistry at the Center for Accelerator Mass Spectrometry (CAMS), Lawrence Livermore National Laboratory and at Beta Analytic. Radiocarbon ages were combined into a composite core chronology through the established stratigraphic correlation between the cores. Radiocarbon dates were calibrated

using the IntCal20 calibration curve (Reimer et al., 2020). Since the radiocarbon ages are not in stratigraphic order, we constructed three possible radiocarbon age-depth models using the Bacon package in R (Blaauw & Christen, 2011). Radiocarbon dates are in calibrated years before present (cal yr BP) and are reported with the modeled 95% confidence range. In addition to the radiocarbon ages, the modeled age of 4,800 cal yr BP (95% range is 4,520 – 5,105) was added at 312 cm depth in core 1. This date is derived from the age-depth model of Duarte et al. (2021) for core 5 (6 km away from core 1; Figure 1) and marks the transition from brackish to freshwater conditions in Lake Izabal (Duarte et al., 2021; Obrist-Farner et al., 2022).

Laminae counting and thickness measurements were performed for the composite core profile using two independent counting processes, one based on manual counting and the other based on a semi-automated process. Manual laminae counting was performed by inspection of the high-resolution line-scan images, and the measurements were made using the Techlog® 2017.2 software. For the semi-automated process, laminae counting was carried out using the countMYvarves software, which uses sliding-window autocorrelation to count the number of repeated patterns in core scans (Van Wyk de Vries et al., 2021). CountMYvarves uses as input parameters the resolution (20 mm pixel^{-1}) of the digital image and the estimated sedimentation rate for the core. Manual laminae counts, assuming that a dark and light couplet represents 1 year, were compared to the radiocarbon age-depth models and to the semi-automated counting method.

4. RESULTS

4.1. CORE SEDIMENTOLOGY AND GEOCHEMISTRY

Based on the sedimentological descriptions of cores 1 and 2, the two cores can be subdivided into three zones: 1) homogeneous and bedded mud; 2) thinly bedded mud; and 3) thinly laminated mud. We focus here on the thinly laminated mud zone, which is 399 cm thick in core 1 and 325 cm thick in core 2 (Figure 2).

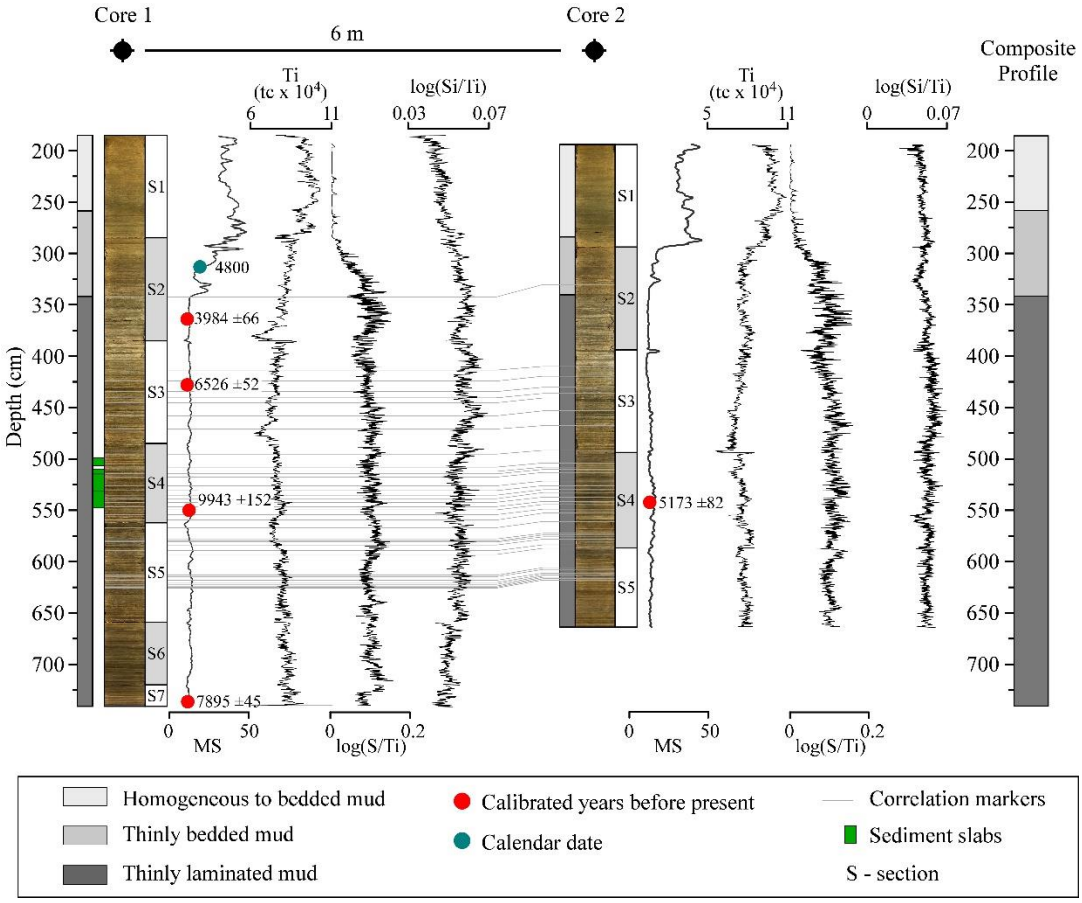

Figure 2. Simplified lithological description, magnetic susceptibility (MS), titanium (Ti), and the log(S/Ti) and log(Si/Ti) ratios of the two sediment cores retrieved from Lake Izabal. Sediment cores were correlated using 38 laminae markers (gray lines). MS is expressed in international standard units (SI) and Ti is expressed in total counts (tc). Radiocarbon dates for cores 1 and 2 are in calibrated years before present (cal yr BP).

The most conspicuous feature of the thinly laminated mud zone is the consistent presence of dark and light laminae that are very similar in thickness but differ in their color. For example, dark laminae are composed of dark grayish brown silty clay (10YR 4/2), while light laminae are composed of light brownish gray silty clay (10YR 6/2).

Dark laminae have a mean thickness of 0.67 mm and a thickness range of 0.39 to 0.79 mm (Figure 3), while light laminae have a mean thickness of 0.62 mm and a thickness range from 0.39 to 0.77 mm. Light and dark laminae couplets have a mean thickness of 1.28 and a thickness range of 0.85 to1.55 mm (Figure 3). There are no changes in thickness through time between dark and light laminae, although variations in couplet thickness are observable through time (Figure 3).

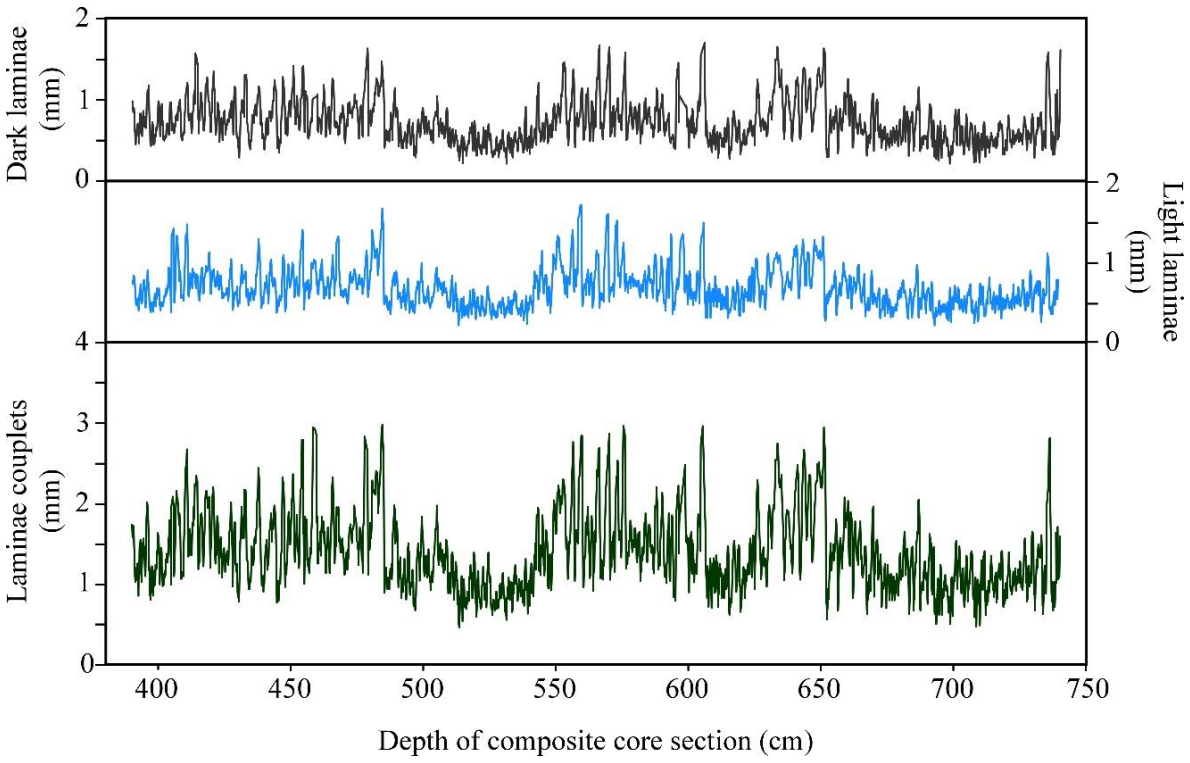

Figure 3. Measured thickness for dark and light laminae and laminae couplets for the thinly laminated mud zone.

Observations of the high-resolution line-scan images, microscopic analysis of smear slides, and grain size indicate that the dark and light laminae are sedimentologically different. Dark laminae contain a larger proportion of detrital minerals (i.e., quartz, plagioclase) and terrestrial organic matter constituents, such as plant cuticle fragments and amorphous organic matter (Figure 4). Dark laminae also contain low abundances of lacustrine biogenic constituents, such as diatom fragments and sponge spicules, and contain a relatively high total carbon content (1.90 to 2.25 wt% C; Table S1 in Supplementary Information) and a high abundance of microscopic pyrite grains (Figure 4). Dark laminae have a mean grain size of medium silt (M_z = 26.43μm ± 7.78; n=5) and are composed of 6.98% ± 3.70 clay, 78.41% ± 5.92 silt, and 15.21% ± 7.72 sand. In contrast, light laminae are characterized by a lower abundance of detrital minerals and organic matter constituents, are enriched in biogenic constituents, and contain a relatively low total carbon content (1.31 to 1.77 wt% C; Table S1) and a high abundance of microscopic pyrite grains (Figure 4). Light laminae have a mean grain size of fine silt (M_z = 10.32μm ± 2 .01; n=5) and are composed of 16.22% ± 4.75 clay, 76.38% ± 3.88 silt, and 7.4% ± 8.51 sand.

Another conspicuous feature of the thinly laminated mud zone is the constant low magnetic susceptibility (MS) values when compared to the zones above, with an average MS value of 5 SI (Figure 2). This zone is also characterized by variations in elemental abundances (Figure S1 in Supplementary Information). For example, the laminated zone is characterized by low and relatively constant Ti abundances, followed by an upward increasing trend in the zones above (Figure 2). Sulfur abundances show the opposite pattern, with high values throughout the thinly laminated mud zone, followed by an upward decreasing trend above. Silica and Fe abundances have similar patterns, with highly

variable abundances in the thinly laminated mud zone, followed by an upward increasing trend (Figure S1). This variability is also observed in elemental ratios. For example, the log(S/Ti) ratio is characterized by high values in the thinly laminated mud zone, followed by a decreasing trend at the top of the core (Figure 2). In comparison, the log(Si/Ti) ratio is characterized by a slightly upward increasing trend in the laminated interval and decreases in the upper part of the cores (Figure 2).

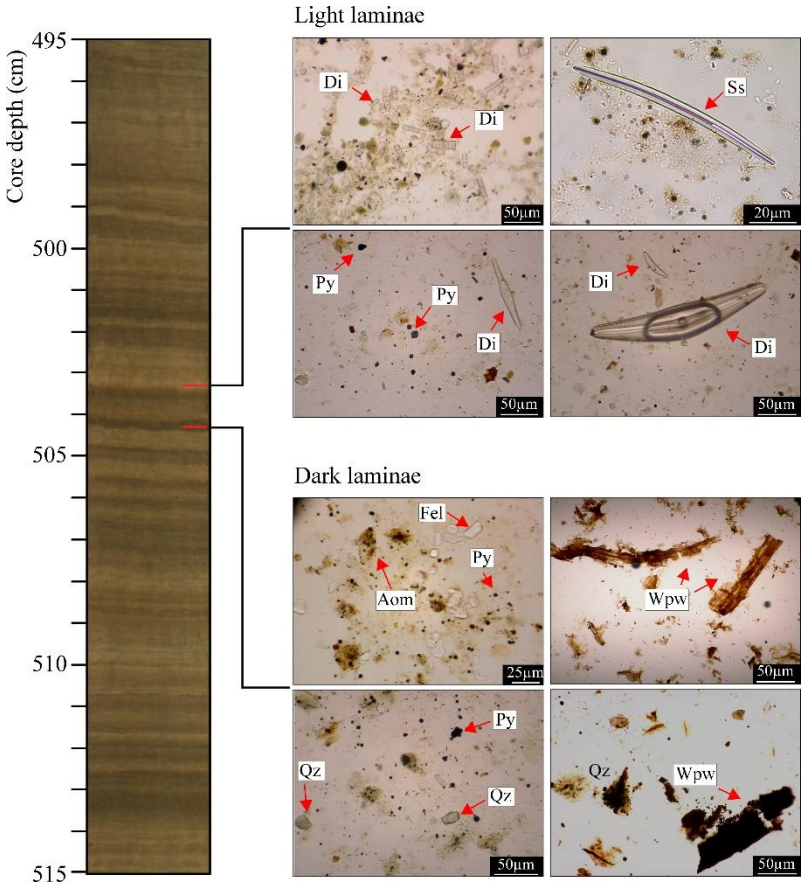

Figure 4. High-resolution digital core scan image showing a section of the thinly laminated mud zone in core 1. Photomicrographs showing an example of light and dark laminae highlighting the main components of the laminae. All images were taken under plane-polarized light. Qz - Quartz; Fel – Feldspar; Py - Pyrite; Ss - Sponge spicule; Di - Diatom; Aom - Amorphous organic matter; Wpw – Well-preserved wood fragments.

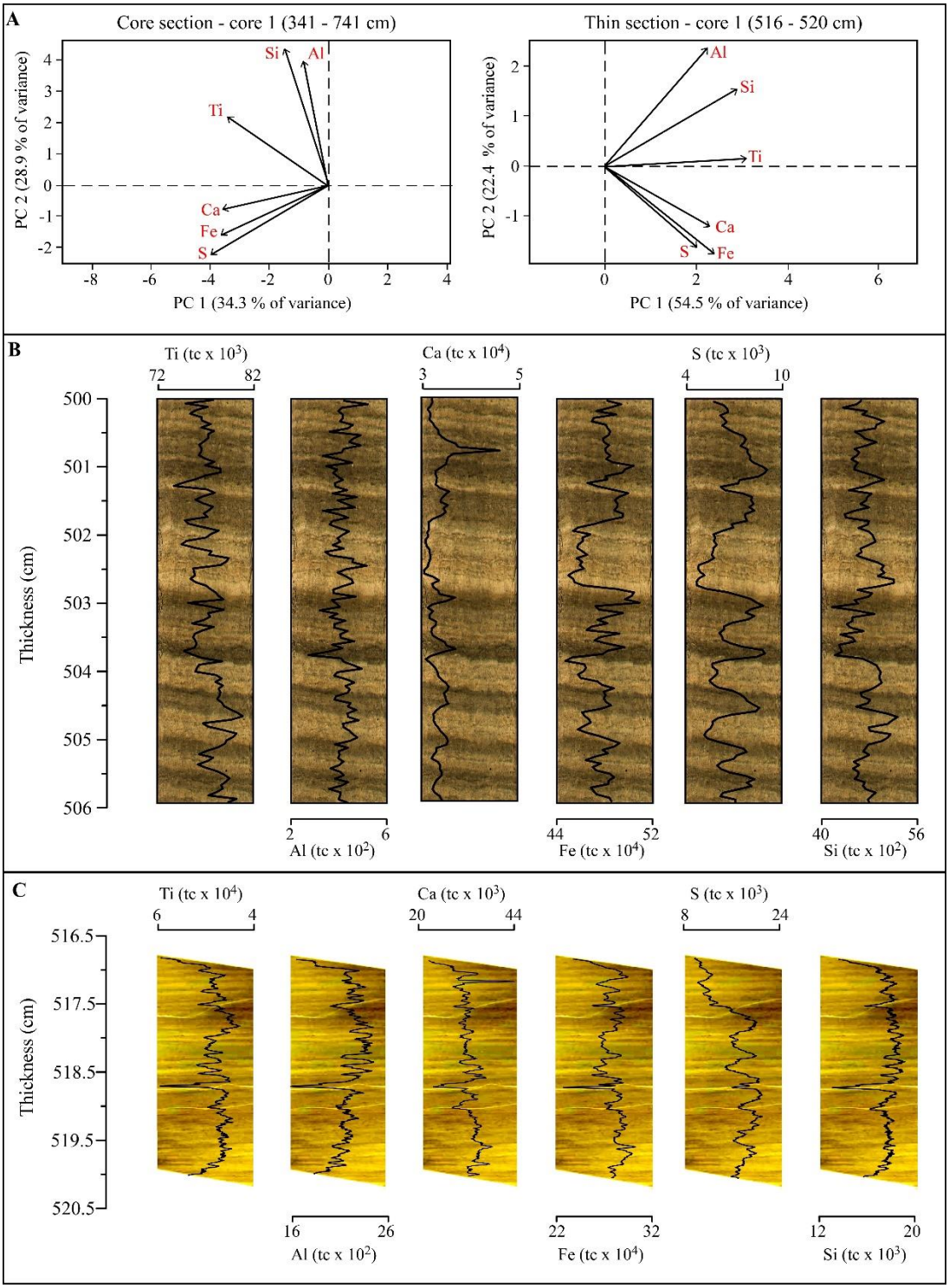

Figure 5. A) Principal component analyses (PCA) for element abundances in the thinly laminated mud zone for core 1 (left) and thin section chip (right). B) Digital core scan image with elemental abundances in total counts (tc) for a section of the thinly laminated mud zone in core 1. C) Thin section image showing elemental abundances in tc for the thin section chip from core 1.

Comparison of the high-resolution µXRF profiles with core photos and with the thin section photo indicates that the dark laminae are characterized by a high abundance of Ti, Fe, S, and Ca. In contrast, light laminae contain higher abundances of Si and Al (Figure 5). Principal component analysis of the µXRF data from the cores and thin section shows two main modes of variability. The first mode of variability is a relationship between S, Fe, and Ca, which are associated along the negative side of the principal component 1 (PC1) in core 1 (34.3% of variance), along the positive side of PC2 in core 2 (29.7% of variance; Figure S2 in Supplementary Information), and along the positive side of PC 1 in the thin section (54.4% of variance; Figure 5). The second mode of variability is the relationship between Si and Al, which are associated along the positive side of PC2 in core 1 (28.9% of variance) and the thin section (22.4% of variance; Figure 5). In core 2, Si and Al are associated along the positive side of PC1 (37.7% of variance; Figure S2). Ti is not associated with the two groups in both cores and thin section (Figure 5; Figure S2 in Supplementary Information).

Elemental ratios also show that the laminae are distinctly different. For example, dark laminae in the cores and thin section chip are characterized by high log(Fe/Ti), log(Mn/Ti), and log(S/Ti) ratios (Figure 6). Light laminae, on the other hand, are characterized by a high log(Si/Ti) ratio (Figure 6). The PCA results on the ratios indicate a relationship between log(Fe/Ti), log(Mn/Ti), and log(S/Ti), which are associated along the positive axis of PC1, which explains 43.8% of the variance (Figure 6). In contrast, the log(Si/Ti) ratio is statistically different and is aligned with the positive axis of PC2, which explains 26.3% of the variance. Similarly, XRF ratios on the thin section chip are characterized by a relationship between log(Mn/Ti) and log(S/Ti) ratios, which are

associated to the negative axis of PC1 (44.9% of variance). In contrast, the log(Si/Ti) ratio is associated to the negative axis of PC2 (28.1% of variance). The log(Fe/Ti) ratio is not associated to the log(Mn/Ti) and log(S/Ti) ratios as seen in the sediment core data (Figure 6).

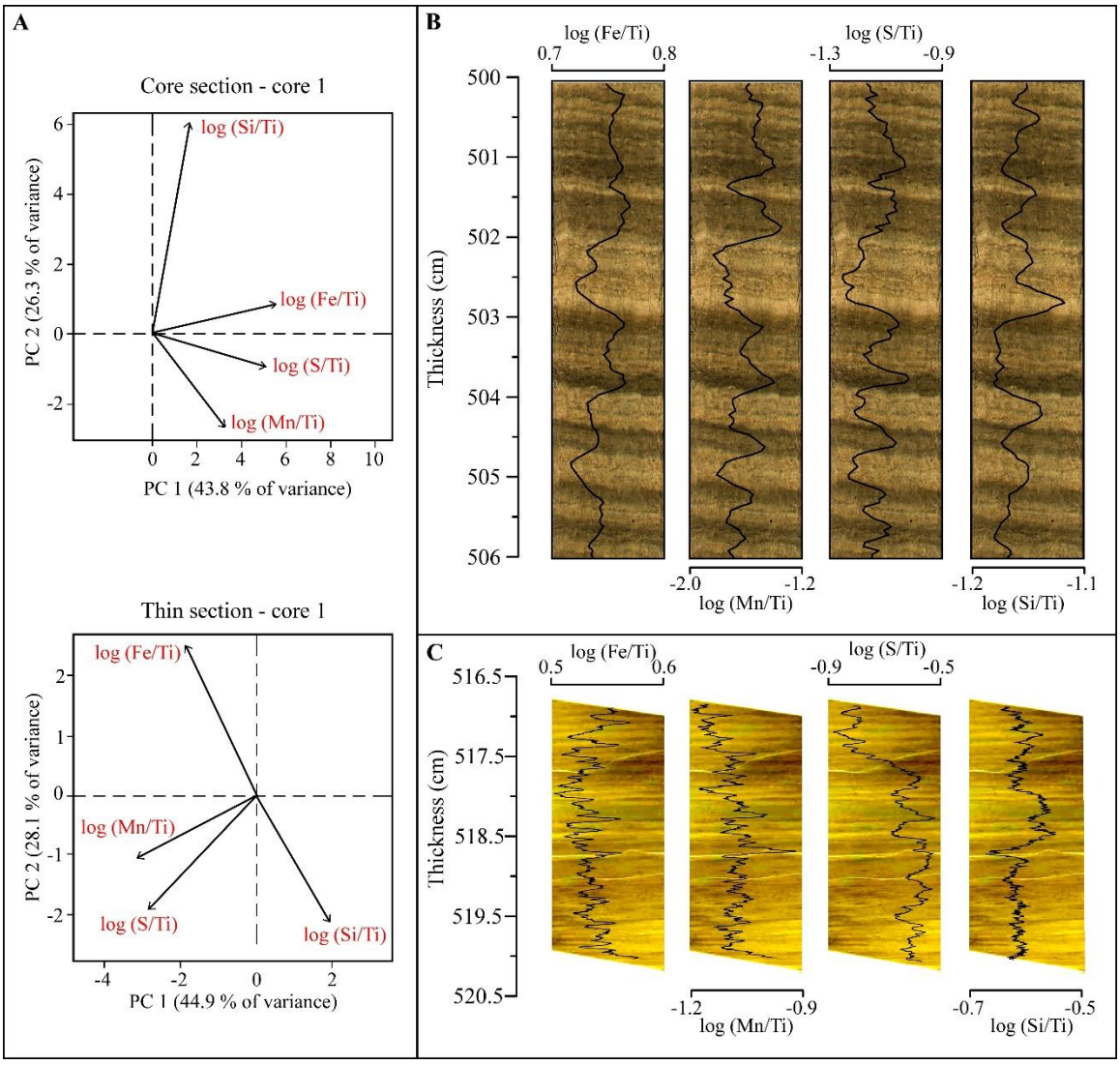

Figure 6. (A) Principal component analyses for XRF ratios from the thinly laminated mud zone for core 1 (top) and thin section chip (bottom). B) Digital core scan image showing elemental ratios for a section of the thinly laminated mud zone in core 1. C) Thin section image showing elemental ratios for the thin section chip from core 1.

4.2. RADIOCARBON BASED CRONOLOGY

The radiocarbon ages are not in stratigraphic order, so their interpretation is not straightforward. To examine the possible range of ages we generated three radiocarbon-based age-depth models with differing assumptions (Figure 7).

Model 1 utilizes three radiocarbon dates and suggests that the laminated segment of the composite profile could span ~3,732 years, from 4,151 (95% range = 3,953 – 4,345) to 7,883 (95% range = 7,722 – 8,007) cal yr BP (Figure 7). Median sedimentation rates range from 0.13 to 0.17 $cmyr^{-1}$ between 389 to 547 cm and then decrease to 0.09-0.12 cmyr-1 from 547 to 740 cm (Figure 8).

Model 2 is based on two radiocarbon dates and the date of 4,800 cal yr BP (95% range is 4,520–5,105) that marks the transition from brackish to freshwater conditions in nearby core 5 (Duarte et al., 2021). Results indicate that the laminated segment of the composite profile could span ~2,500 years, from 5,822 (95% range = 5,494 – 6,129) to 8,322 (95% range = 7,897 – 9,206) cal yr BP (Figure 7). Median sedimentation rates range from 0.06 to 0.07 $cmyr^{-1}$ between 389 to 435 cm, followed by a sharp increase, with the sedimentation rate changing to 0.15 to 0.22 $cmyr^{-1}$ until the bottom of the profile (Figure 8).

Finally, model 3 is based on two calibrated radiocarbon dates. Results indicate that the laminated segment of the composite profile could span ~2,830 years, from 3,687 (3,433 – 3,892) to 6,517 (6,127 – 6,950) cal yr BP (Figure 7). Median sedimentation rates remain constant throughout the laminated interval, ranging from 0.16 to 0.21 $cmyr^{-1}$ (Figure 8).

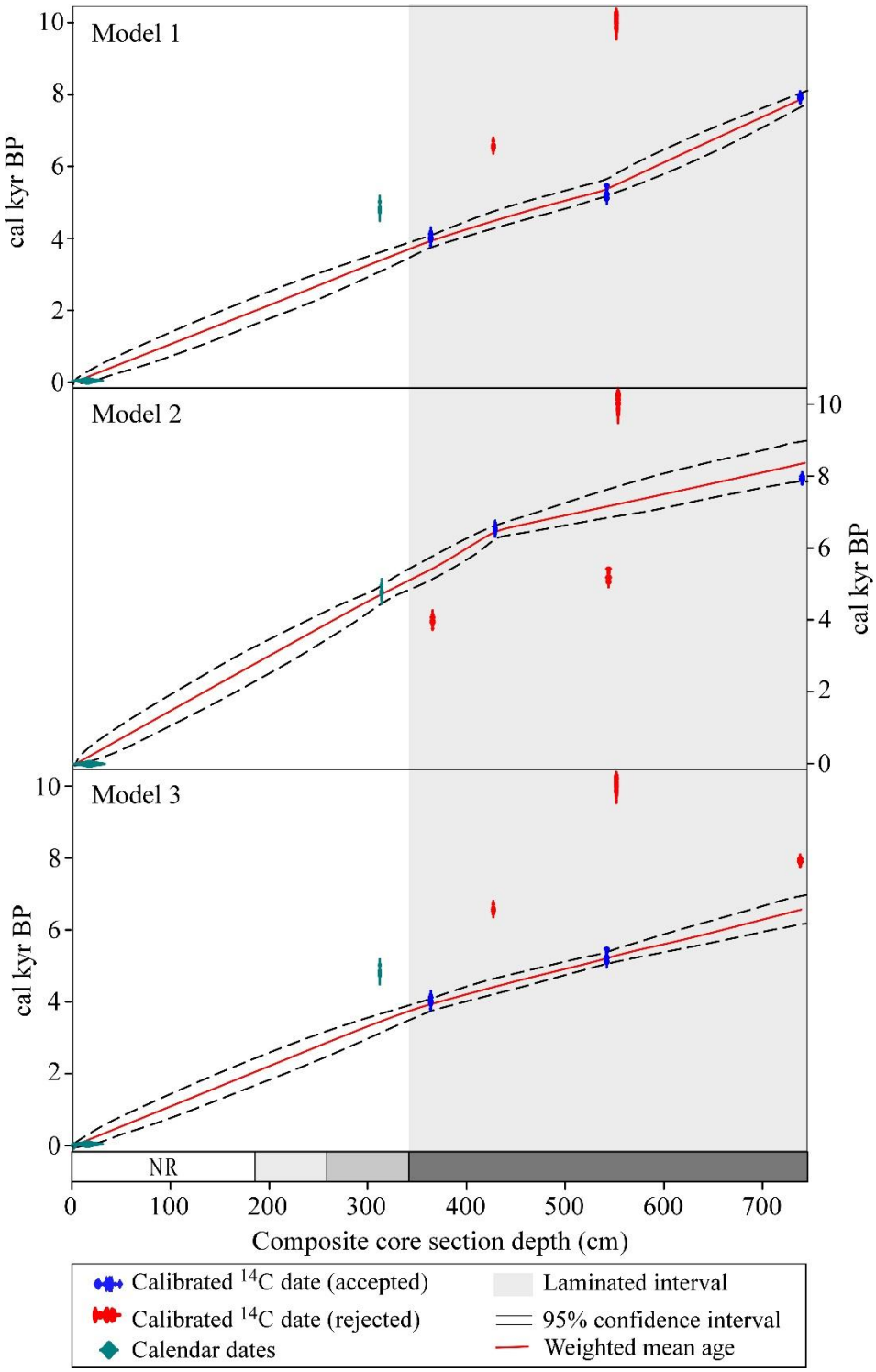

Figure 7. Proposed age-depth models for the composite core profile. Envelopes between black dashed lines show 95% confidence intervals. Red curves show the single best model based on the mean age for each depth. See Figure 2 for the simplified lithological legend. NR = core segment not recovered.

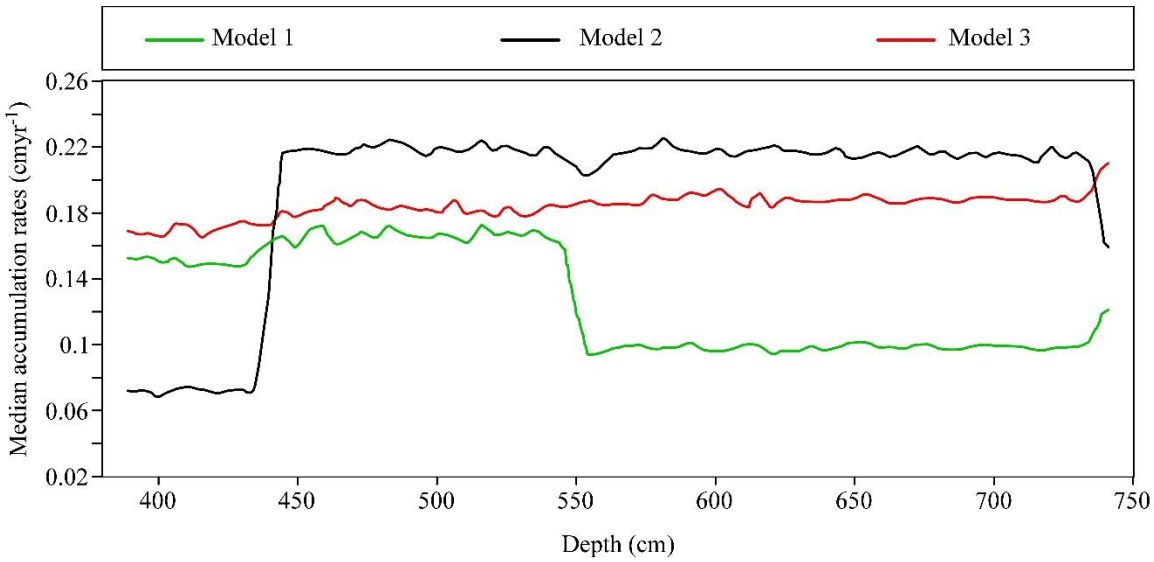

Figure 8. Estimated median accumulation rates ($cmyr^{-1}$) for the three proposed age-depth models. Accumulation rates were computed for the thinly laminated mud zone using the Bacon package in R (Blaauw and Christen, 2011).

4.3. LAMINAE COUNTING AND VARVED AGE-DEPTH MODELS

Results from the manual counts suggest that the entire laminated composite core sequence is composed of 2,186 ± 45.1 laminae couplets. We compared laminae count results with laminae counts generated automatically by the countMYvarves software. The semi-automated countMYvarves model counted 2,102 laminae couplets with a range between 2,193 and 2,000 (Figure 9). Comparison of the two indicates that the manual counts broadly correlate with the countMYvarves model (Figure 9).

We also compared the manual and semi-automated laminae count models with 1,000 Markov Chain Monte Carlo (MCMC) age-depth iterations obtained from the three radiocarbon-based age-depth models (Figure 10).

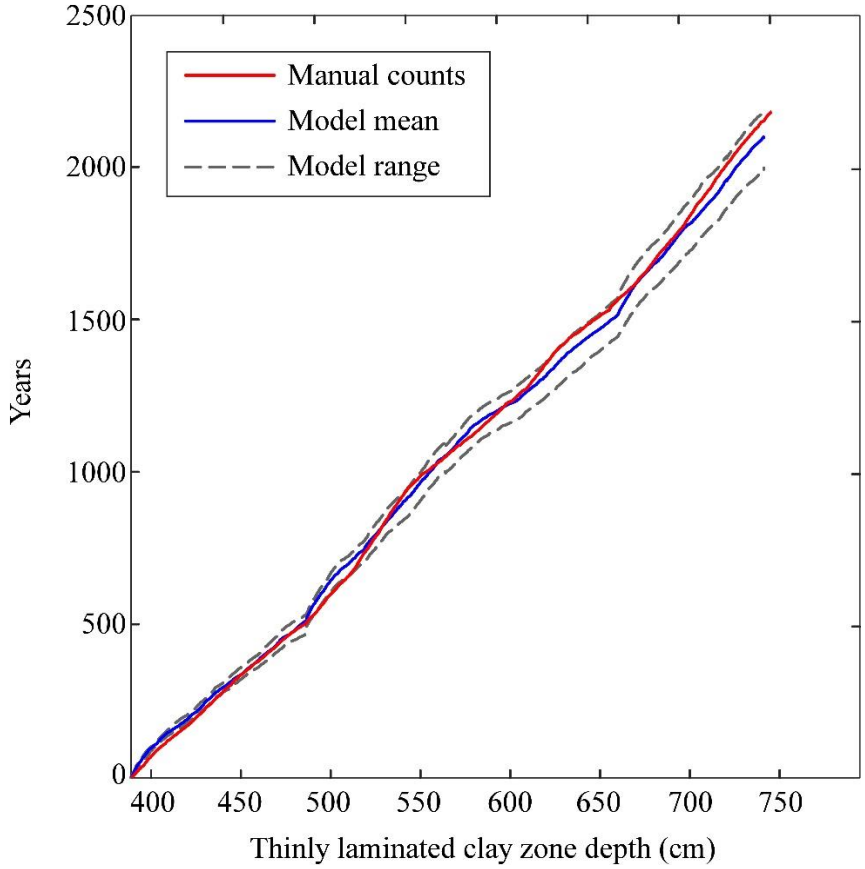

Figure 9. Results of the manual laminae counts and the semi-automated models for the entire thinly laminated mud zone (lowermost 356 cm of the composite profile). The semi-automated models were generated using countMYvarves (Van Wyk de Vries et al., 2021).

The results for model 1 indicate that the sedimentation rate derived from the varve model is similar to the radiocarbon-based age-depth models until ~590 cm. The lower 156 cm are not correlated, with the varve model predicting a higher sedimentation rate (0.17 $cmyr^{-1}$) than the radiocarbon-based age depth model (0.09 $cmyr^{-1}$). Models 2 and 3 have a sedimentation rates (0.19 and 0.18 $cmyr^{-1}$, respectively) comparable to that of the varve model (0.18 $cmyr^{-1}$), with the varve model ages coinciding with the lower ranges of the MCMC results (Figure 10).

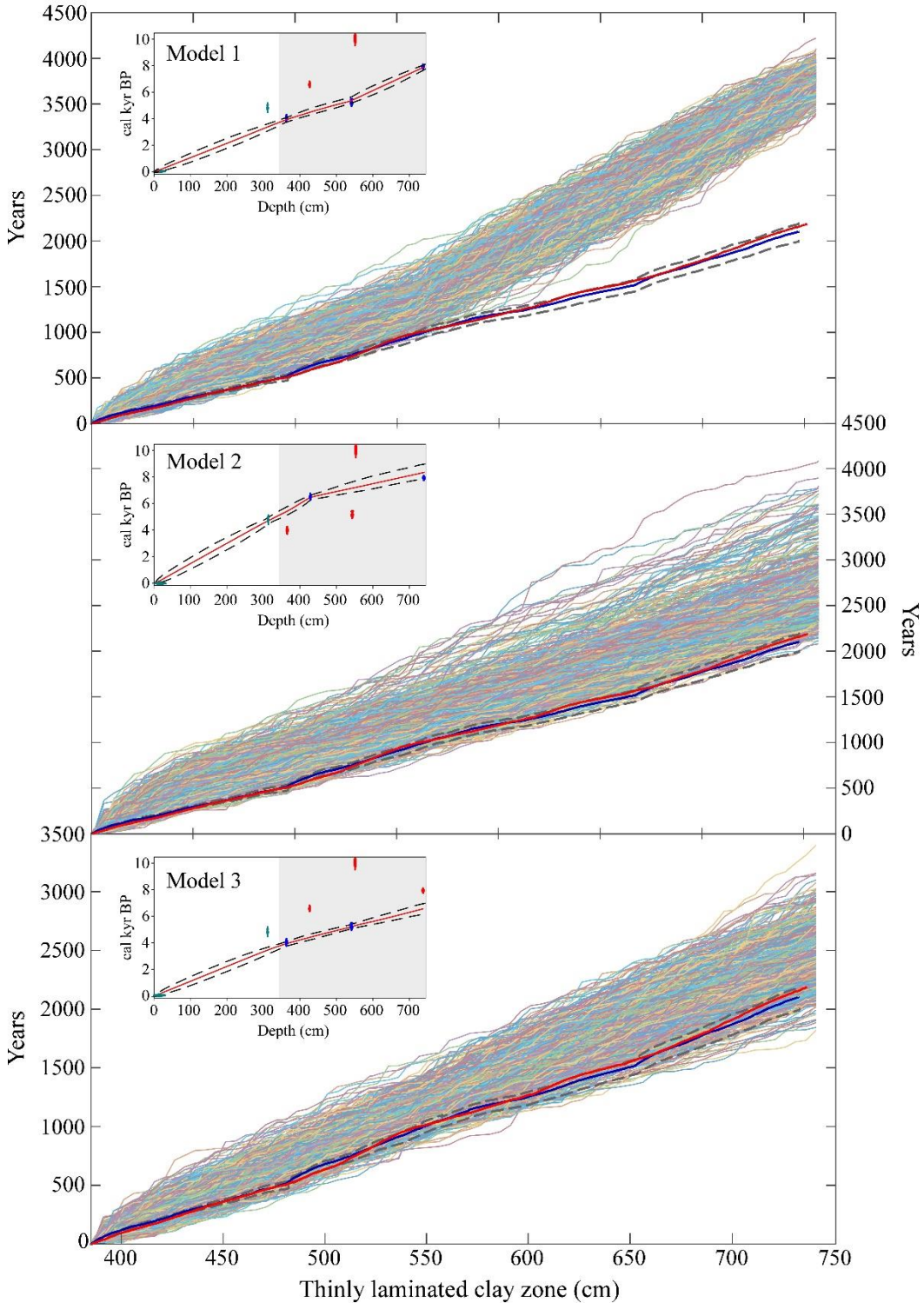

Figure 10. Resulting 1,000 Markov Chain Monte Carlo (MCMC) age-depth iterations for the laminated section of the composite profile plotted with the varve chronology. The Monte Carlo iterations were extracted from the radiocarbon-based age-depth models calculated using the Bacon package in R (Blaauw and Christen, 2011).

5. DISCUSSION

Our sedimentological observations reveal a detailed and well-preserved laminated sedimentary section in Lake Izabal that spans close to 2,200 years (Figure 7), covering a large part of the mid-Holocene. Our analyses indicate that the dark and light laminae are distinctive, with differences in color, composition, texture, and organic constituents. The larger grain size and abundance of detrital grains and allochthonous woody organic fragments suggest that dark laminae formed during times of greater terrestrial sediment input into Lake Izabal. This inference is supported by a greater abundance of elements associated with increased runoff, such as Ti and Fe (e.g., Kylander et al., 2011; Figure 5), as well as by a higher concentration of total organic carbon (ST 1) and higher log(S/Ti) ratio values, a proxy for increased organic matter (Moreno et al., 2007). We suggest that the dark laminae were deposited during times of increased river runoff, most likely during the rainy season in Izabal. Modern observations from Brinson (1973) suggest that the hydrological regime exerts a significant control on organic matter and sediment flow into Lake Izabal, recognizing that turbidity in the water increases during the wet season as a result of greater input of detritus-laden waters into the lake.

Light laminae, by contrast, have decreased grain size, detrital grains and organic content (ST 1) accompanied increases in diatoms and sponge spicules (Figure 4), consistent with a reduction in detrital input to the lake and an increase in biogenic constituents. This is supported by an overall increase in Si and the log(Si/Ti) ratio in light laminae (Figure 6), indicating more production and deposition of lacustrine biogenic silica (Brown et al., 2007; Brown, 2011; Brown, 2015). Limnological observations in Lake Izabal (e.g.,

Brinson and Nordlie, 1975) show increased primary productivity during the dry season, most likely as a result of greater light penetration into the water column. Our sedimentological observations support the view that the dark and light laminae formed in response to seasonality in precipitation and were preserved during the mid-Holocene period of anoxia (Figure 11).

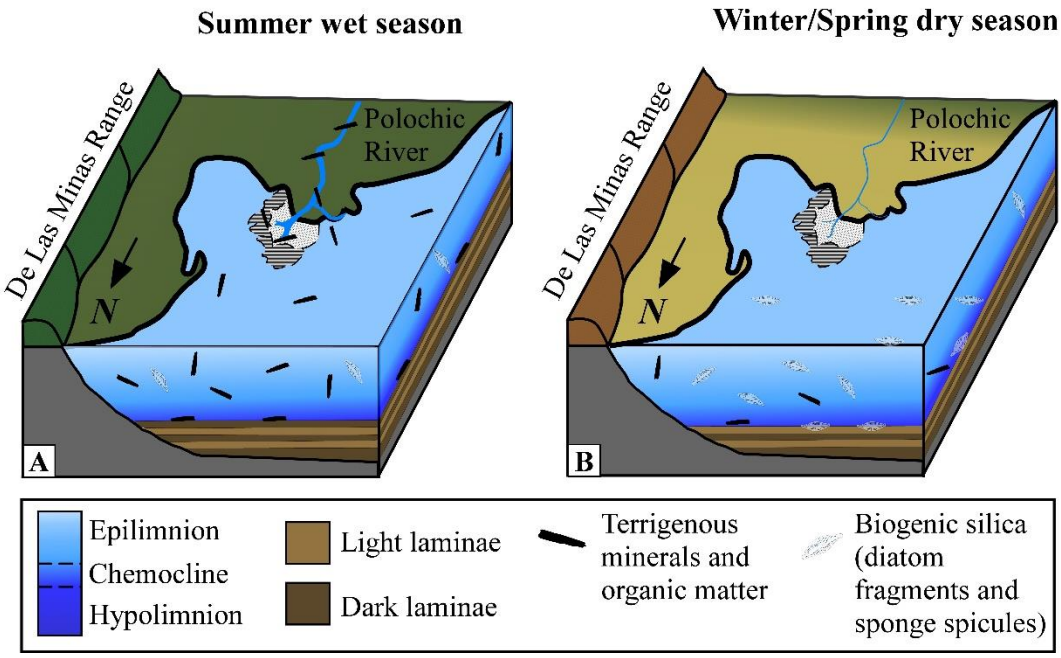

Figure 11. Depositional model of the thinly laminated mud zone in Lake Izabal. (A) Deposition of dark laminae during the summer wet season, characterized by a high abundance of organic matter and detritus. (B) Deposition of light laminae during the winter and spring dry season, characterized by a high abundance of opaline silica.

PCA results based on µXRF scans of the core and a thin section demonstrate differences in the elemental composition of the dark and light laminae and reveal several interesting processes happening in Lake Izabal during the mid-Holocene. First, and as noted above, the similarities between detrital elements (e.g., Ti, Fe, Al) and their relative

increase in dark laminae support our interpretation that darker laminae formed during increased detrital influx into the lake. The abundance of Si, however, is not always related to detrital sediment flux; the log(Si/Ti) ratio and in the PCA results indicating that some of the observed variability in Si abundance is mostly related to changes in lake productivity. Second, there is a similarity between the abundance in S and Fe, especially in the dark laminae, which is also evident by their association in the PCA results (Figure 5). This relationship was documented by Duarte et al. (2021), who suggested that the presence of brackish and anoxic bottom-waters controlled redox processes in the lake. In anoxic marine sediments, pyrite (FeS) formation is aided by the presence of sulfate-reducing bacteria and organic matter, which is necessary for sulfate reduction (Raiswell and Berner, 1985). The higher concentration of organic carbon and higher abundance of S, Fe, and woody debris suggests an increase in pyrite formation during deposition of the dark laminae.

Throughout the core, the observed changes in XRF elemental abundances do not systematically correlate with the observed changes in the core photographs. There are two potential reasons for this discrepancy. First, the μXRF core scans were carried out at 0.5 mm steps, while laminations in Lake Izabal are, on average, 0.64 mm thick but range between 0.39 to 0.78 mm. The variability in thickness and constant 0.5 mm steps by the core scanner would have resulted in variable levels of aliasing during the analyses. Second, the laminations in Lake Izabal are not always parallel to each other and are not always perpendicular to the core tube. The ITRAX has an analytical footprint that is 8 mm wide, indicating that some measurements could be combining results from two or several laminae. The thin section chip scan, however, was carried out at a much finer resolution (0.04 mm) to evaluate these issues. Similarities between the XRF observations in the core

and thin section chip, combined with similar PCA results, support our inference of distinct compositional changes in the laminations.

Obtaining radiocarbon dates and a robust radiocarbon age-depth model is challenging in this system due to the scarcity of macroscopic terrestrial material and to the stratigraphic reversals in our radiocarbon results. This means that a wide range of possible ages for the laminated segment of the sediment cores are consistent with our data. However, additional supporting information has helped us constrain the chronology of the laminated sediment section. 1) The consistent presence of laminae in both cores and their thickness trends does not support the abrupt changes in sedimentation rates observed in both radiocarbon-based models 1 and 2. Deposition of laminae with similar thickness indicates that sedimentation rate was most likely constant during the mid-Holocene. This is supported by previous paleolimnological studies in Lake Izabal that have shown that sedimentation was constant during the mid-Holocene in the deeper parts of the basin (Duarte et al., 2021). 2) Duarte et al. (2021) reported a linear sedimentation rate of ~0.08 cm yr-1 for the laminated segment of core 5 based on 11 radiocarbon ages. This sedimentation rate is half of the one reconstructed for cores 1 and 2 based on radiocarbon-age depth models 2 and 3 and based on the varve age-depth model. However, the laminated segment of cores 1 (399 cm) and 2 (325 cm) differ significantly in thickness from the laminated segment of core 5 (210 cm), suggesting that the sediment rate in the deeper, more central part of Lake Izabal was at least twice as fast as in core 5 but without abrupt changes. This additional information, combined with the similarities between models 2 and 3 and our varve age-depth model (Figure 10), supports our interpretation of the laminae couplets as varves. Finally, exclusion of the 4,800 cal yr BP

date increases the similarity between model 3 and the varve age-depth model (Figure 10). This implies that the change from brackish to freshwater observed in core 5 (z = 12 m) at 4,800 cal yr BP was not a temporally coherent basinwide change. Instead, it suggests that the change may have been gradual, with the brackish to freshwater transition occurring somewhat later in the deepest parts of Lake Izabal.

6. CONCLUSIONS

Sedimentological and geochemical analyses of the thinly laminated sediment cores from Lake Izabal provide new insights into the nature and chronology of the laminations and the processes that led to their formation. Our results indicate that the laminated section consists of alternating clastic (dark) and biogenic (light) laminae couplets that are distinctly different in their color, texture and composition. These laminae couplets most likely formed because of the characteristic seasonality in precipitation observed in western Central America. Consistency between radiocarbon age-depth models and the laminae chronology support our interpretation of the laminae couplets as varves. However, additional cores and radiocarbon dates are needed to further refine and constrain the chronology of the laminae. For now, this work provides a detailed view of the processes allowing for varve development, documenting one of the first annually resolved sedimentological records from the region, which will allow to investigate mid-Holocene climatic and tectonic events in Central America at an unprecedented resolution.

ACKNOWLEDGMENTS

This study was partially supported by the Geological Society of America (GSA) Graduate Student Research Grant, funded by the National Science Foundation (NSF) Award no. 1712071. This research was also partially supported by the Visiting Graduate Student Program from the Continental Scientific Drilling (CSD) Facility (Minnesota). Brooke Birkett is acknowledged with gratitude for her insightful comments on the manuscript. We thank Defensores de la Naturaleza Foundation (Guatemala) for managing fieldwork logistics. This is contribution # 15 of the Missouri S&T MCTF research group, and LLNL-JRNL-805149.

APPENDIX A.

SUPPLEMENTARY FIGURES

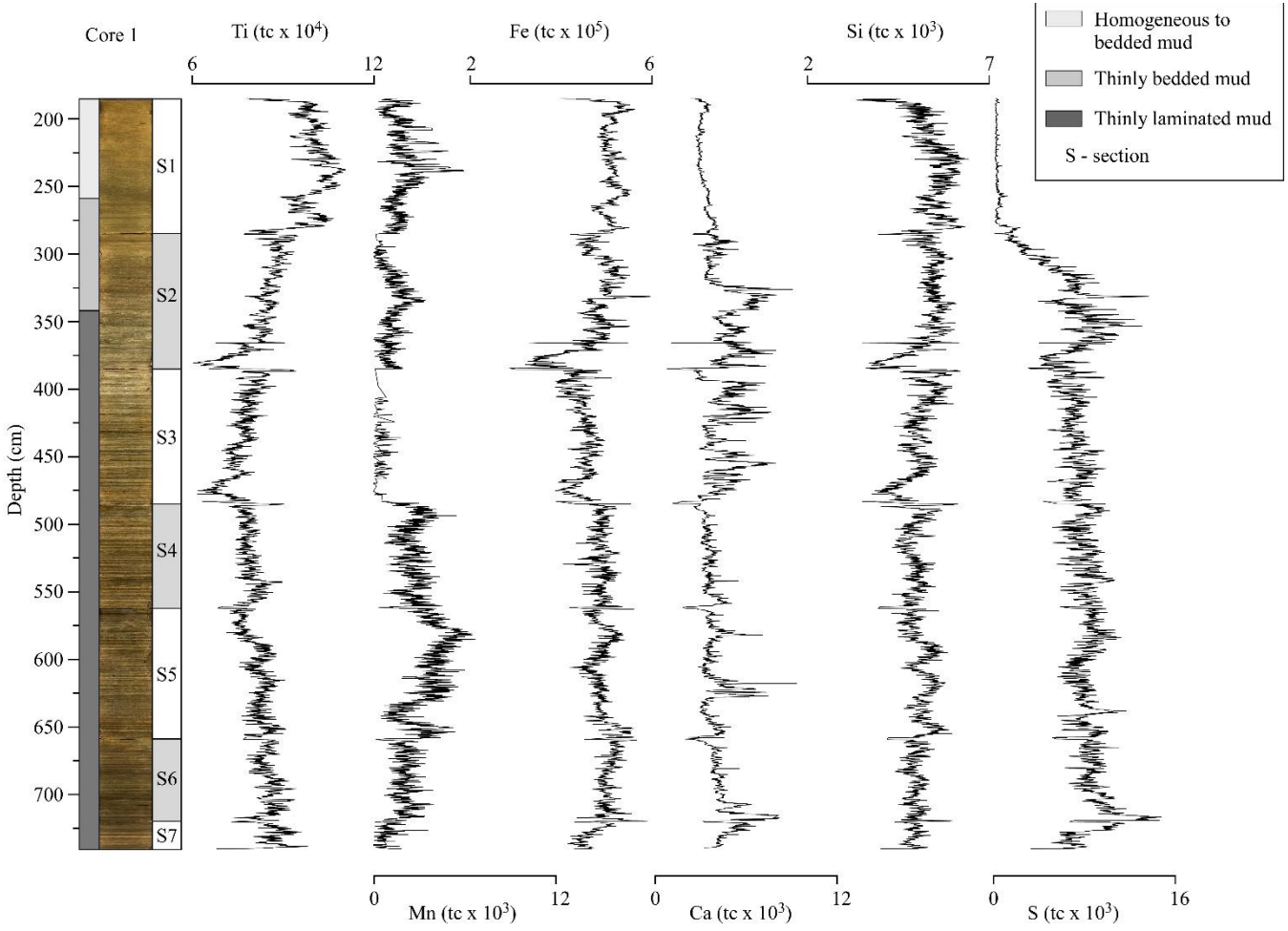

Figure S1. Proxy data and simplified lithology versus depth for core 1. Elemental abundances in total counts (tc).

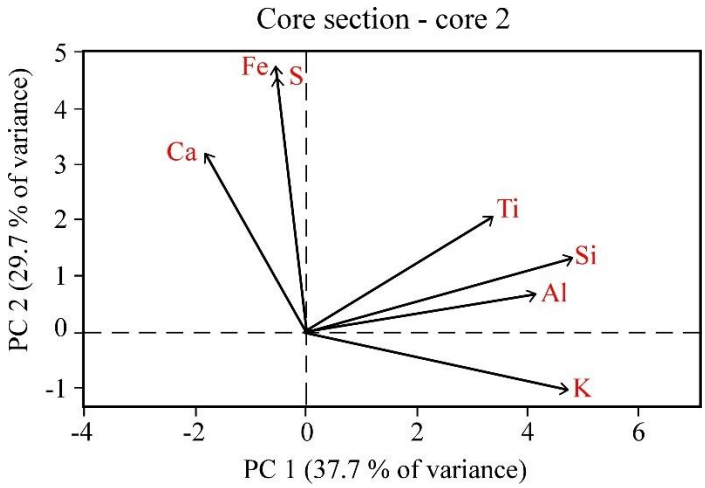

Figure S2. Principal component analyses (PCA) using the µXRF data from the thinly laminated clay zone in core 2.

APPENDIX B.

SUPPLEMENTARY TABLES

Table S1. Percent Carbon (wt %C) on samples from cores 1 in Lake Izabal.

Core	Depth	Laminae	Sample Weight [mg]	Reten. Time [min]	Response	Weight [mg]	Weight [%]
				Carbon	Carbon	Carbon	Carbon
1	623.889	Dark	2.771	5.167	764.591	0.062	2.25
1	623.953	Light	2.882	5.175	628.014	0.051	1.77
1	624.024	Dark	3.565	5.179	949.431	0.078	2.17
1	624.103	Light	1.954	5.176	350.817	0.028	1.45
1	624.182	Dark	2.212	5.18	367.851	0.03	1.34
1	624.356	Light	2.77	5.179	446.891	0.036	1.31
1	624.467	Dark	2.367	5.177	639.649	0.052	2.2
1	624.641	Light	3.761	5.175	738.906	0.06	1.6
1	624.705	Dark	2.496	5.183	676.854	0.055	2.2
1	624.792	Light	3.172	5.187	593.74	0.048	1.52
1	624.839	Dark	3.177	5.197	849.117	0.069	2.18
1	624.879	Light	3.411	5.18	588.117	0.048	1.4
1	624.95	Dark	3.244	5.196	857.005	0.07	2.15
1	625.053	Light	1.985	5.192	402.381	0.033	1.64
1	625.116	Dark	3.104	5.183	759.596	0.062	1.99
1	625.164	Light	3.453	5.176	650.246	0.053	1.53
1	625.259	Dark	1.859	5.188	454.564	0.037	1.98
1	625.362	Light	3.272	5.197	678.331	0.055	1.69
1	625.488	Dark	2.376	5.18	557.787	0.045	1.9
1	625.781	Light	3.183	5.184	637.201	0.052	1.63

Table S2. Radiocarbon dates on samples from cores 1 and 2 in Lake Izabal, Guatemala.

Sample type	Accession number	Core name	Corrected depth (cm)	^{14}C age	± 1σ	Mean age (cal yr BP)[a]	Error (1σ)	Status	Modeled age (cal yr BP)	95% range (cal yr BP)[a]
Wood fragment	CAMS-185397	1	364	3645	40	3984	66	Rejected	5402	5104 - 5724
Wood fragment	Beta-504957	1	428	5730	30	6526	52	Accepted	6464	6294 - 6616
Wood fragment	Beta-516048	2	542	4530	30	5173	82	Rejected	7137	6822 - 7594
Wood fragment	CAMS-185398	1	552	8860	80	9943	152	Rejected	7197	6870 - 7684
Wood fragment	Beta-503614	1	739	7070	40	7895	45	Accepted	8302	7884 - 9174

[a] Radiocarbon ages at depth in the core (m below lake floor) were converted into calendar ages (cal yr BP) using Oxcal 4.4 (Bronk Ramsey, 2009) with the calibration curve IntCal20 (Reimer et al., 2020) and an age-depth model with a 95% confidence range was constructed using the Bayesian software Bacon (Blaau and Christen, 2011).

REFERENCES

Bartole, R., Lodolo, E., Obrist-Farner, J., and Morelli, D., 2019, Sedimentary architecture, structural setting, and Late Cenozoic depocentre migration of an asymmetric transtensional basin: Lake Izabal, eastern Guatemala: Tectonophysics, v. 750, p. 419-433. https://doi.org/10.1016/j.tecto.2018.12.004

Blaauw, M., and Christen, J. A., 2011, Flexible paleoclimate age-depth models using an autoregressive gamma process: Bayesian Analysis, v. 6, no. 3, p. 457-474. https://doi.org/10.1214/11-BA618

Brinson, M. M., 1973, The Organic Matter Budget and Energy Flow of a Tropical Lowland Aquatic Ecosystem: University of Florida, 273 p.

Brinson, M. M., and Nordlie, F. G., 1975, II. Lakes. 8. Central and South America: Lake Izabal, Guatemala: SIL Proceedings, 1922-2010 Internationale Vereinigung für Theoretische und Angewandte Limnologie: Verhandlungen, v. 19, no. 2, p. 1468-1479. https://doi.org/10.1080/03680770.1974.11896206

Brocard, G., Adatte, T., Magand, O., Pfeifer, H.-R., Bettini, A., Arnaud, F., Anselmetti, F. S., and Moran-Ical, S., 2014, The recording of floods and earthquakes in Lake Chichój, Guatemala during the twentieth century: Journal of Paleolimnology, v. 52, no. 3, p. 155-169. https://doi.org/10.1007/s10933-014-9784-4

Brown, E., 2011, Lake Malawi's response to “megadrought” terminations: Sedimentary records of flooding, weathering and erosion: Palaeogeography Palaeoclimatology Palaeoecology - PALAEOGEOGR PALAEOCLIMATOL, v. 303, p. 120-125. https://doi.org/10.1016/j.palaeo.2010.01.038

-, 2015, Estimation of Biogenic Silica Concentrations Using Scanning XRF: Insights from Studies of Lake Malawi Sediments, in Smol, J. P., ed., Micro-XRF Studies of Sediment Cores Applications of a non-destructive tool for the environmental sciences, Volume 17: Kingston, ontario, Canada, Springer, p. 267-277. https://doi.org/10.1007/978-94-017-9849-5_9

Brown, E., Johnson, T. C., Scholz, C., Cohen, A., and King, J., 2007, Abrupt change in tropical African climate linked to the bipolar seesaw over the past 55,000 years: Geophysical Research Letters, v. 34, p. 20702. https://doi.org/10.1029/2007GL031240

Buckley, K. L., and Obrist-Farner, J., 2019, Sedimentological characteristics of a laminated core from Lake Izabal, eastern Guatemala, Geological Society of America Annual Meeting, Volume 51: Phoenix, Arizona, USA, GSA, p. 193-110.

Curtis, J. H., Brenner, M., Hodell, D. A., Balser, R. A., Islebe, G. A., and Hooghiemstra, H., 1998, A multi-proxy study of Holocene environmental change in the Maya Lowlands of Peten, Guatemala: Journal of Paleolimnology, v. 19, no. 2, p. 139-159. https://doi.org/10.1023/A:1007968508262

Curtis, J. H., Hodell, D. A., and Brenner, M., 1996, Climate variability on the Yucatan Peninsula (Mexico) during the past 3500 years, and implications for Maya cultural evolution: Quaternary Research, v. 46, no. 1, p. 37-47.

Deevey, E. S., 1965, Sampling lake sediments by use of the Livingstone sampler, in Kummel, B., and Raup, D., eds., Handbook of Paleontological Techniques Freeman, p. 521-529. https://doi.org/10.1002/gj.3350050122

Duarte, E., Obrist-Farner, J., Correa-Metrio, A., and Steinman, B. A., 2021, A progressively wetter early through middle Holocene climate in the eastern lowlands of Guatemala: Earth and Planetary Science Letters, v. 561, p. 116807. https://doi.org/10.1016/j.epsl.2021.116807

Folk, R. L., and Ward, W. C., 1957, Brazos River bar [Texas]; a study in the significance of grain size parameters: Journal of Sedimentary Research, v. 27, no. 1, p. 3-26. https://doi.org/10.1306/74D70646-2B21-11D7-8648000102C1865D

Haug, G. H., Hughen, K. A., Sigman, D. M., Peterson, L. C., and Röhl, U., 2001, Southward Migration of the Intertropical Convergence Zone Through the Holocene: Science, v. 293, no. 5533, p. 1304. https://doi.org/10.1126/science.1059725

Hillesheim, M. B., Hodell, D. A., Leyden, B. W., Brenner, M., Curtis, J. H., Anselmetti, F. S., Ariztegui, D., Buck, D. G., Guilderson, T. P., and Rosenmeier, M. F., 2005, Climate change in lowland Central America during the late deglacial and early Holocene: Journal of Quaternary Science, v. 20, no. 4, p. 363-376. https://doi.org/10.1002/jqs.924

Hodell, D. A., Brenner, M., Curtis, J. H., and Guilderson, T., 2001, Solar forcing of drought frequency in the Maya lowlands: Science, v. 292, no. 5520, p. 1367-1370. https://doi.org/10.1126/science.1057759

Hodell, D. A., Curtis, J. H., and Brenner, M., 1995, Possible role of climate in the collapse of Classic Maya civilization: Nature, v. 375, no. 6530, p. 391. https://doi.org/10.1038/375391a0

Hodell, D. A., Curtis, J. H., Jones, G. A., Higuera-Gundy, A., Brenner, M., Binford, M. W., and Dorsey, K. T., 1991, Reconstruction of Caribbean climate change over the past 10,500 years: Nature, v. 352, no. 6338, p. 790-793. https://doi.org/10.1038/352790a0

Hughen, K. A., Overpeck, J. T., Peterson, L. C., and Anderson, R. F., 1996, The nature of varved sedimentation in the Cariaco Basin, Venezuela, and its palaeoclimatic significance, in Kemp, A. E. S., ed., Palaeoclimatology and Palaeoceanography from Laminated Sediments, Volume 116: London, Geological Society, London, Special Publications, p. 171-183. https://doi.org/10.1144/GSL.SP.1996.116.01.15

Jolliffe, I., 1986, Principal Component Analysis. Berlin, Springer-Verlag. https://doi.org/10.1007/b98835

Kylander, M. E., Ampel, L., Wohlfarth, B., and Veres, D., 2011, High-resolution X-Ray fluorescence core scanning analysis of Les Echets (France) sedimentary sequence: New insights from chemical proxies: Journal of Quaternary Science, v. 26, no. 1, p. 109-117. https://doi.org/10.1002/jqs.1438

Larsen, C. P. S., Pienitz, R., Smol, J. P., Moser, K. A., Cumming, B. F., Blais, J. M., Macdonald, G. M., and Hall, R. I., 1998, Relations between lake morphometry and the presence of laminated lake sediments: a re-examination of Larsen and Macdonald (1993): Quaternary Science Reviews, v. 17, no. 8, p. 711-717. https://doi.org/10.1016/S0277-3791(97)00043-7

Leyden, B. W., Brenner, M., Hodell, D. A., and Curtis, J. H., 1994, Orbital and internal forcing of climate on the Yucatan Peninsula for the past ca. 36 ka: Palaeogeography, Palaeoclimatology, Palaeoecology, v. 109, no. 2, p. 193-210. https://doi.org/10.1016/0031-0182(94)90176-7

Medina, C., Gomez-Enri, J., Villares, P., and Alonso, J., An Integrated Methodology for the Environmental Assessment and Management of Lake Izabal (Guatemala), in Proceedings Proceedings Proceedings of the 3rd WSEAS Int. Conf. on Energy Planning, Energy Saving, Environmental Education2009, p. 150-157.

Moreno, A., Giralt, S., Valero-Garcés, B., Sáez, A., Bao, R., Prego, R., Pueyo, J. J., González-Sampériz, P., and Taberner, C., 2007, A 14kyr record of the tropical Andes: The Lago Chungará sequence (18°S, northern Chilean Altiplano): Quaternary International, v. 161, no. 1, p. 4-21. https://doi.org/10.1016/j.quaint.2006.10.020

Mueller, A. D., Islebe, G. A., Hillesheim, M. B., Grzesik, D. A., Anselmetti, F. S., Ariztegui, D., Brenner, M., Curtis, J. H., Hodell, D. A., and Venz, K. A., 2009, Climate drying and associated forest decline in the lowlands of northern Guatemala during the late Holocene: Quaternary Research, v. 71, no. 2, p. 133-141. https://doi.org/10.1016/j.yqres.2008.10.002

Obrist-Farner, J., Brenner, M., Curtis, J. H., Kenney, W., and Salvinelli, C., 2019, Recent onset of eutrophication in Lake Izabal, the largest water body in Guatemala: Journal of Paleolimnology, v. 62, p. 359-372. https://doi.org/10.1007/s10933-019-00091-3

Obrist-Farner, J., Brenner, M., Stone, J. R., Wojewódka-Przybył, M., Bauersachs, T., Eckert, A., Locmelis, M., Curtis, J. H., Zimmerman, S. R. H., Correa-Metrio, A., Schwark, L., Duarte, E., Schwalb, A., Niewerth, E., Echeverría-Galindo, P. G., and Pérez, L., 2022, New estimates of the magnitude of the sea-level jump during the 8.2 ka event: Geology, v. 50, no. 1, p. 86-90. https://doi.org/10.1130/G49296.1

Obrist-Farner, J., Eckert, A., Locmelis, M., Crowley, J. L., Mota-Vidaure, B., Lodolo, E., Rosenfeld, J., and Duarte, E., 2020, The role of the Polochic Fault as part of the North American and Caribbean Plate boundary: Insights from the infill of the Lake Izabal Basin: Basin Research, v. 32, no. 6, p. 1347-1364. https://doi.org/10.1111/bre.12431

Ojala, A., Saarinen, T., and Salonen, V.-P., 2000, Preconditions for the formation of annually laminated lake sediments in Southern and central Finland: Boreal Environment Research, v. 5, p. 243-255.

Raiswell, R., and Berner, R. A., 1985, Pyrite formation in euxinic and semi-euxinic sediments: American Journal of Science, v. 285, p. 710-724. https://doi.org/10.2475/ajs.285.8.710

Reimer, P. J., Austin, W. E. N., Bard, E., Bayliss, A., Blackwell, P. G., Bronk Ramsey, C., Butzin, M., Cheng, H., Edwards, R. L., Friedrich, M., Grootes, P. M., Guilderson, T. P., Hajdas, I., Heaton, T. J., Hogg, A. G., Hughen, K. A., Kromer, B., Manning, S. W., Muscheler, R., Palmer, J. G., Pearson, C., van der Plicht, J., Reimer, R. W., Richards, D. A., Scott, E. M., Southon, J. R., Turney, C. S. M., Wacker, L., Adolphi, F., Büntgen, U., Capano, M., Fahrni, S. M., Fogtmann-Schulz, A., Friedrich, R., Köhler, P., Kudsk, S., Miyake, F., Olsen, J., Reinig, F., Sakamoto, M., Sookdeo, A., and Talamo, S., 2020, The IntCal20 Northern Hemisphere Radiocarbon Age Calibration Curve (0–55 cal kBP): Radiocarbon, v. 62, no. 4, p. 725-757. https://doi.org/10.1017/RDC.2020.41

Schnurrenberger, D., Russell, J., and Kelts, K., 2003, Classification of lacustrine sediments based on sedimentary components: Journal of Paleolimnology, v. 29, no. 2, p. 141-154. https://doi.org/10.1023/A:1023270324800

Stansell, N. D., Steinman, B. A., Lachniet, M. S., Feller, J., Harvey, W., Fernandez, A., Shea, C. J., Price, B., Coenen, J., Boes, M., and Perdziola, S., 2020, A lake sediment stable isotope record of late-middle to late Holocene hydroclimate variability in the western Guatemala highlands: Earth and Planetary Science Letters, v. 542, p. 116327. https://doi.org/10.1016/j.epsl.2020.116327

Tylmann, W., Zolitschka, B., Enters, D., and Ohlendorf, C., 2013, Laminated lake sediments in northeast Poland: distribution, preconditions for formation and potential for paleoenvironmental investigation: Journal of Paleolimnology, v. 50, no. 4, p. 487-503. https://doi.org/10.1007/s10933-013-9741-7

Van Wyk de Vries, M., Ito, E., Shapley, M., and Brignone, G., 2021, Semi-automated counting of complex varves through image autocorrelation: Quaternary Research, p. 1-12. https://doi.org/10.5281/zenodo.4031811.

Wahl, D., Byrne, R., and Anderson, L., 2014, An 8700 year paleoclimate reconstruction from the southern Maya lowlands: Quaternary Science Reviews, v. 103, p. 19-25. http://dx.doi.org/10.1016/j.quascirev.2014.08.004

Winter, A., Zanchettin, D., Lachniet, M., Vieten, R., Pausata, F. S. R., Ljungqvist, F. C., Cheng, H., Edwards, R. L., Miller, T., Rubinetti, S., Rubino, A., and Taricco, C., 2020, Initiation of a stable convective hydroclimatic regime in Central America circa 9000 years BP: Nature Communications, v. 11, no. 1, p. 716. https://doi.org/10.1038/s41467-020-14490-y

Zolitschka, B., Francus, P., Ojala, A. E. K., and Schimmelmann, A., 2015, Varves in lake sediments – a review: Quaternary Science Reviews, v. 117, p. 1-41. https://doi.org/10.1016/j.quascirev.2015.03.019

SECTION

2. CONCLUSIONS

Analysis of the sediment cores retrieved from Lake Izabal provides new insights into Holocene hydroclimatic changes in the eastern lowlands of Guatemala. The Abundance of elements commonly associated with terrigenous sources increased from the early to the latest mid-Holocene, from ca. 9,500 to ca. 4,800 cal yr BP, suggesting a progressive increase in erosion/precipitation. From 8,370 to 4,800 cal yr BP, marine waters entered the lake, establishing a chemocline that most likely turned Lake Izabal into a meromictic lake, with persistent bottom-water anoxia. Anoxia decreased bioturbation in the deeper parts of the basin, facilitating the preservation of a thinly laminated section that consists of alternating clastic and biogenic laminae couplets that are distinctly different in their color, texture, and composition. Our analyses suggest that the laminae couplets are annual deposits, and that their physical and compositional differences are mainly driven by precipitation seasonality, preserved during the unusual period of anoxia. At ~4,800 cal yr BP, Lake Izabal became a polymictic lake, characterized by the disappearance of laminations and relatively stable and high erosion/precipitation conditions until ca. 1,200 cal yr BP. It is followed by an abrupt decrease in erosion/precipitation starting at 1,200 years ago.

The inferred patterns of hydroclimate change from the Lake Izabal cores support new evidence that Central American precipitation variability throughout the Holocene was highly heterogeneous. Our observations are potentially explainable by a gradual

increase in Caribbean SSTs throughout the Holocene. Warmer SST would have increased moisture availability through enhanced evaporation, amplifying precipitation in the eastern lowlands of Guatemala. Our results also provide insights into the nature and chronology of the laminations and the processes that led to their formation, documenting one of the first annually resolved mid-Holocene sedimentological records from the region. This record will allow us to investigate climatic and tectonic events in Central America at an unprecedented resolution. Additional paleoclimate records from the Central American region are needed to improve our understanding of regional climatic changes and reconcile differences between the Izabal record and other regional paleoclimate datasets.

BIBLIOGRAPHY

Anderson, T. G., Anchukaitis, K. J., Pons, D., and Taylor, M., 2019, Multiscale trends and precipitation extremes in the Central American Midsummer Drought: Environmental Research Letters, v. 14, no. 12, p. 124016. https://doi.org/10.1088/1748-9326/ab5023

Bhattacharya, T., and Coats, S., 2020, Atlantic-Pacific Gradients Drive Last Millennium Hydroclimate Variability in Mesoamerica: Geophysical Research Letters, v. 47. https://doi.org/10.1029/2020GL088061

Brinson, M. M., 1973, The Organic Matter Budget and Energy Flow of a Tropical Lowland Aquatic Ecosystem: University of Florida, 273 p.

Brinson, M. M., and Nordlie, F. G., 1975, II. Lakes. 8. Central and South America: Lake Izabal, Guatemala: SIL Proceedings, 1922-2010 Internationale Vereinigung für Theoretische und Angewandte Limnologie: Verhandlungen, v. 19, no. 2, p. 1468-1479. https://doi.org/10.1080/03680770.1974.11896206

Christensen, J. H., Hewitson, B., Busuioc, A., Chen, A., Gao, X., Held, I., Jones, R., Kolli, R. K., Kwon, W.-T., Laprise, R., Magaña Rueda, V., Mearns, L., Menéndez, C. G., Räisänen, J., Rinke, A., Sarr, A., and Whetton, P., 2007, Regional Climate Projections, in Solomon, S., Qin, D., Manning, M., Chen, Z., Marquis, M., Averyt, K. B., Tignor, M., and Miller, H. L., eds., Climate Change 2007: The Physical Science Basis. Contribution of Working Group I to the Fourth Assessment Report of the Intergovernmental Panel on Climate Change: Cambridge, United Kingdom and New York, NY, USA., Cambridge University Press, p. 94.

Fensterer, C., Scholz, D., Hoffmann, D. L., Spötl, C., Schröder-Ritzrau, A., Horn, C., Pajón, J. M., and Mangini, A., 2013, Millennial-scale climate variability during the last 12.5ka recorded in a Caribbean speleothem: Earth and Planetary Science Letters, v. 361, p. 143-151. https://doi.org/10.1016/j.epsl.2012.11.019

Gutiérrez, J. M., Jones, R. G., Narisma, G. T., Alves, L. M., Amjad, M., Gorodetskaya, I. V., Grose, M., Klutse, N. A. B., Krakovska, S., Li, J. M.-C., D. , Mearns, L. O., Mernild, S. H., Ngo-Duc, T., van den Hurk, B., and Yoon, J. H., 2021, Atlas, in Masson-Delmotte, V., Zhai, P., Pirani, A., Connors, S. L., Péan, C., Berger, S., Caud, N., Chen, Y., Goldfarb, L., Gomis, M. I., Huang, M., Leitzell, K., Lonnoy, E., Matthews, J. B. R., Maycock, T. K., Waterfield, T., Yelekçi, O., Yu, R., and Zhou, B., eds., In Climate Change 2021: The Physical Science Basis. Contribution of Working Group I to the Sixth Assessment Report of the Intergovernmental Panel on Climate Change, Cambridge University Presss. In Press., p. 1-196.

Haug, G. H., Hughen, K. A., Sigman, D. M., Peterson, L. C., and Röhl, U., 2001, Southward Migration of the Intertropical Convergence Zone Through the Holocene: Science, v. 293, no. 5533, p. 1304. https://doi.org/10.1126/science.1059725

Hillesheim, M. B., Hodell, D. A., Leyden, B. W., Brenner, M., Curtis, J. H., Anselmetti, F. S., Ariztegui, D., Buck, D. G., Guilderson, T. P., and Rosenmeier, M. F., 2005, Climate change in lowland Central America during the late deglacial and early Holocene: Journal of Quaternary Science, v. 20, no. 4, p. 363-376. https://doi.org/10.1002/jqs.924

Hodell, D. A., Curtis, J. H., Jones, G. A., Higuera-Gundy, A., Brenner, M., Binford, M. W., and Dorsey, K. T., 1991, Reconstruction of Caribbean climate change over the past 10,500 years: Nature, v. 352, no. 6338, p. 790-793. https://doi.org/10.1038/352790a0

Martinez, C., Goddard, L., Kushnir, Y., and Ting, M., 2019, Seasonal climatology and dynamical mechanisms of rainfall in the Caribbean: Climate Dynamics, v. 53, no. 1, p. 825-846. https://doi.org/10.1007/s00382-019-04616-4

Mueller, A. D., Islebe, G. A., Hillesheim, M. B., Grzesik, D. A., Anselmetti, F. S., Ariztegui, D., Brenner, M., Curtis, J. H., Hodell, D. A., and Venz, K. A., 2009, Climate drying and associated forest decline in the lowlands of northern Guatemala during the late Holocene: Quaternary Research, v. 71, no. 2, p. 133-141. https://doi.org/10.1016/j.yqres.2008.10.002

Stansell, N. D., Steinman, B. A., Lachniet, M. S., Feller, J., Harvey, W., Fernandez, A., Shea, C. J., Price, B., Coenen, J., Boes, M., and Perdziola, S., 2020, A lake sediment stable isotope record of late-middle to late Holocene hydroclimate variability in the western Guatemala highlands: Earth and Planetary Science Letters, v. 542, p. 116327. https://doi.org/10.1016/j.epsl.2020.116327

Wang, C., 2007, Variability of the Caribbean Low-Level Jet and its relations to climate: Climate Dynamics, v. 29, no. 4, p. 411-422. https://doi.org/10.1007/s00382-007-0243-z

Winter, A., Zanchettin, D., Lachniet, M., Vieten, R., Pausata, F. S. R., Ljungqvist, F. C., Cheng, H., Edwards, R. L., Miller, T., Rubinetti, S., Rubino, A., and Taricco, C., 2020, Initiation of a stable convective hydroclimatic regime in Central America circa 9000 years BP: Nature Communications, v. 11, no. 1, p. 716. https://doi.org/10.1038/s41467-020-14490-y

VITA

Edward Fernando Duarte Martinez was born in Bucaramaga, Colombia. In May 2013, he graduated with a Bachelor of Science in Geology from Univeridad Industrial de Santander (UIS), Colombia. Edward has participated in research projects in Colombia, Brazil, and Guatemala, mainly in paleoenvironmental reconstructions from tropical and subtropical basins. As a doctoral student at Missouri University of Science and Technology, Edward worked as a graduate teaching and research assistant from 2018 to 2022 in the Geosciences and Geological and Petroleum Engineering Department. During this time, he has been involved in a multidisciplinary research project that aims to afford insight into regional hydroclimate and paleoenvironmental changes in the eastern lowlands of Guatemala over the last ~10,000 years. He has also been involved in various side projects in Guatemala and Colombia, mainly in basin analysis. Edward received his PhD degree in geology and geophysics from Missouri University of Science and Technology, Rolla, Missouri, USA in July 2022. In July 2022, Edward began a postdoctoral position in the Dynamic Environment and Mountain Territories Laboratory (EDYTEM) at the University of Savoie Mont Blanc, France.